DESIGN OF A DOPPLER-AIDED GPS NAVIGATION SYSTEM FOR WEAK SIGNALS CAUSED BY STRONG IONOSPHERIC SCINTILLATION

A DISSERTATION
SUBMITTED TO THE DEPARTMENT OF AERONAUTICS AND ASTRONAUTICS
AND THE COMMITTEE ON GRADUATE STUDIES
OF STANFORD UNIVERSITY
IN PARTIAL FULFILLMENT OF THE REQUIREMENTS
FOR THE DEGREE OF
DOCTOR OF PHILOSOPHY

Tsung-Yu Chiou
May 2010

Abstract

The fundamental tasks of a Global Positioning System (GPS) receiver are signal tracking and noise rejection. The essence of this dissertation is investigating the balance between the aforementioned objectives; taking advantage of the noise immunity property of external sensors, and designing novel integrated tracking architectures to advance the performance of a GPS receiver under strong interference conditions. Specifically, the problem of interest is resolving the interference due to ionospheric scintillation on the GPS receiver used in aviation navigation.

Using GPS for landing aircraft in equatorial regions is more difficult than in other regions because ionospheric scintillation is prevalent. Ionospheric scintillation causes amplitude fades of 20 dB or more, and an increase in the phase jitter.

This research evaluates techniques to enhance a GPS receiver's ability to overcome ionospheric scintillation. To validate the designed GPS receiver, a GPS channel model for aircraft landing in equatorial regions is built based on the use of a high fidelity GPS constellation simulator, a clock emulator, and real GPS data from the equator that contains an abundance of ionospheric scintillation.

The results of this research demonstrate that the integration of a GPS receiver with a low-cost inertial navigation system provides the capability to operate continuously during periods of strong scintillation. In addition, so-called vector processing also shows promise for a less severe scintillation environment. Various combinations of receiver tracking architectures and aiding methods have been analyzed to quantify the sensitivity improvement of an “aided” GPS receiver.

Acknowledgements

I would like to thank the following people for their technical advice, funding support, and assistance during my Ph.D. candidacy.

I would like to say thank you to my advisor, Prof. Per Enge. Special appreciation is given to him for his proficient technical guidance, continuous encouragement, and funding support throughout my graduate studies. His door is always open to students. Over the years, whenever I encountered difficulties in research, he was always enthusiastic about my questions and gave me sharp insights into the problems. I will never forget the enjoyable time spent doing research with him. These unforgettable days will influence the rest of my life.

I would like to express thanks to my reading committee, Prof. David Powell and Dr. Todd Walter. Thank you for reading my dissertation, giving me your keen comments, and guiding me through the process of completing my dissertation. Special thanks to Dr. Todd Walter for his continued support during my doctoral studies.

Many thanks to my oral committee, Prof. Brian Cantwell and Prof. Mark Kasevich. Thank you for your time for my defense presentation. I appreciate your comments on my defense. I also want to thank you for being so supportive when I asked you to be on my oral committee.

I would like to sincerely thank my sponsor, the Federal Aviation Administration (FAA), for financially supporting me throughout my graduate studies. Without your funding support, my dissertation would never exist.

Special thanks to Dan Babitch at SiRF Inc., Dr. Ted Beach at AFRL, and Paul Crampton at Spirent Inc. for providing and helping me with the clock signal emulating, the scintillated GPS data, and the use of the Spirent simulator. Without your help, I would not have been able to complete my dissertation.

I wish to thank Dr. Demoz Gebre-Egziabher, Dr. Dennis Akos and Dr. David De Lorenzo for your guidance on the GPS baseband analysis and the implementation on the software receiver. I would like to thank Professor Kai Borre at Aalborg University in Denmark for his experienced comments on designing a GPS software receiver. Parts (the navigation engine) of the software receiver developed for this dissertation were based on Professor Borre's and his colleagues' software receiver. Thank you very much for giving me your outstanding advice.

Life with colleagues in the GPS lab, friends at Stanford, and help from the staff of the lab and the department are unforgettable. Thank you all for cheering me up from time to time.

Love from my parents and brothers is invaluable. Thank you for always being so encouraging over the years. Although I saw you face to face only several times in the past 7 years, smiles from each of you are kept in my mind. I look forward to being with you more often after my graduation.

Finally, I sincerely thank my wife, Chia-Yu Kao, and my daughters Sandra Chiou, and Sophia Chiou. Thank you very much for being with me everyday and for bringing me so much happiness. We have gone through one of the best parts of our life together.

Contents

List of Tables

List of Figures

Chapter 1

Introduction

1.1 Background

The Global Positioning System (GPS) is a radio navigation system; therefore a GPS receiver is subject to radio frequency interference. Among the natural interferences to a GPS receiver, ionospheric scintillation is one of the strongest. Typically, severe ionospheric scintillation occurs more frequently in equatorial regions. The impacts of ionospheric scintillation on a GPS receiver include power fading and rapid carrier phase variation.

The signals received by a GPS receiver in an airplane have traveled through the atmosphere from the satellites in orbit. As a result, the transmitted signals have been degraded by several uncertainties. One of the largest channel errors is due to the perturbations in the ionosphere layer. This channel degradation caused by the ionosphere can be divided into two categories. The first ionosphere error is the nominal ionosphere delay, which can be predicted by the Klobuchar model or removed using a dual frequency technique. The second ionospheric effect of interest is scintillation. Ionospheric scintillation is caused by the results of local ionosphere plasma anomalies. Deep signal power fading and rapid phase variations are the typical characteristics of ionospheric scintillation. Power fading and phase variations may lead to the loss of signal lock or an increases in measurement errors. As a result, ionospheric scintillation is a threat to the continuity of GPS. Figure 1.1 on page 3 shows the deep power fading phenomenon due to ionospheric scintillation. The scintillated signals are real GPS data collected in the equatorial region in 2001, which represents the last solar maximum. Ionospheric scintillation occurs frequently every day during solar max years. As can be seen in the figure, signal power fades by more than 20 dB in a period of tens seconds. A traditional GPS receiver satisfying the requirements of aviation navigation usually has the sensitivity of 27 to 30 dB-Hz. As can be seen in Figure 1.1, a traditional GPS receiver would have difficulties continuously providing reliable position fixes. The receiver may not be able to maintain phase or frequency lock during the periods of deep fading. Consequently, the receiver cannot offer accurate measurements for computing accurate position solutions.

One could reduce the bandwidth of the tracking loops during the periods of deep power fading. By reducing the bandwidth, the tracking loop would reject much noise and would, hopefully, be able to keep phase or frequency locks. However, the problem is not that straightforward. The loop bandwidth cannot be reduced too much. There are dynamic stresses for the receiver to track. Therefore, this problem leads us to investigate the methods for optimizing the loop bandwidth. The process of determining the optimal bandwidth needs the understanding of all possible error sources going into the carrier tracking loops. Accordingly, the approach of this work is:

1. To examine the characteristics of the ionospheric scintillation;
2. To analyze the impact of ionospheric scintillation on a GPS receiver;
3. To investigate possible methods for resolving the issues caused by ionospheric scintillation;
4. To design and implement a GPS software receiver which executes the possible methods;
5. To enable a hardware simulation for validating the proposed methods and the designed GPS software receiver; and,
6. To step back, to look into the fundamentals of a GPS receiver, to view the receiver as a system, and to design the system considering all of the challenges that the system has to face.

This research designs a Doppler-aided GPS navigation system for processing weak signals caused by ionospheric scintillation. The relative motion between the satellite and the receiver causes a Doppler shift in the GPS signals. Doppler-aiding means that the Doppler estimate is provided to the GPS receiver by another source. In doing this, we reduce the burden of the GPS receiver such that it has more capability for tracking weak signals.

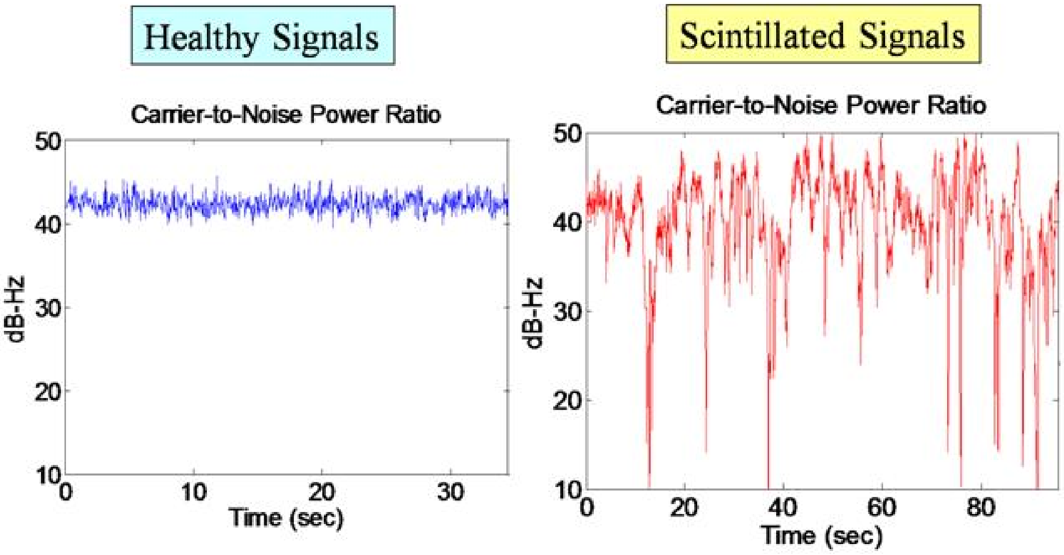

Figure 1.1: GPS Signal-to-Noise Power Ratio for Healthy and Scintillated Signals

The motivation for this dissertation is to investigate the difficulties of aircraft landing using GPS in equatorial regions and to research enhanced GPS navigation for mitigating these difficulties. As will be discussed, there are in fact three intertwined challenges for GPS receivers operating in aircraft near the equator. The first challenge of the GPS receiver is the weak signals due to scintillation. The second challenge is clock vibration due to the airframe vibration. The GPS receiver clock, a crystal oscillator, is sensitive to the aircraft vibration. Because of the impact of this vibration on the GPS receiver clock, the phase noise in the GPS carrier tracking loop increases. The third challenge is the platform dynamic stress. Disturbances such as wind gusts and a pilot's maneuvers create dynamic stress in the GPS receiver. As a result, the GPS receiver for aircraft landing in equatorial regions must overcome the aforementioned three challenges.

The main idea to resolve the scintillation problem is to find an aiding source, which allows us to reduce the receiver bandwidth. In this work, we consider two Doppler-aiding sources: vector processing and an inertial system. Vector processing calculates the Doppler estimate of the weak channels using the strong channels. This aiding method [2] is effective when there are at least four or more strong channels. However, if there are fewer than four healthy channels, the Doppler estimate must rely on an external measurement, i.e., an inertial system. The Doppler-aiding using an inertial system is achieved by tightly coupling the GPS receiver with the inertial measurement unit (IMU). In addition to the two Doppler aiding sources, we also evaluate the performance of applying Doppler aiding to both coherent and non-coherent carrier tracking loops.

Coherent tracking means that the receiver utilizes a phase-locked loop (PLL) to track the phase of the received GPS signal. In contrast, non-coherent tracking refers to the utilization of a frequency-locked loop (FLL) to track the frequency of the received GPS signal. In this dissertation, the two labels of "PLL/FLL" and "coherent/non-coherent" will be used interchangeably.

Figure 1.2 on the next page demonstrates the architecture of the Doppler-aided GPS receiver that we develop in this work. The receiver runs coherent and non-coherent carrier tracking in parallel. Depending on the availability of pseudorange measurements, the navigation function switches between the two tracking modes to calculate position, velocity, and time (PVT). The bit and frame synchronization of the non-coherent tracking is provided by the coherent tracking channels. The Doppler aiding can be applied to both of the carrier tracking loops of the software receiver. This receiver has various degrees of freedom. We can implement different architectures of code and carrier tracking loops. Furthermore, the update rate of the tracking loops, the update rate of the PVT solutions, and the rate of Doppler aiding are all flexible. The design parameters are determined according to the model analysis of the problem of interest to this dissertation.

In this work, we conducted a hardware simulation to validate the designed GPS receiver. Figure 1.3 on page 6 depicts the steps of constructing the hardware simulation. The setup includes the following components.

1. A Spirent GPS simulator. This simulator is used to create the user motions, the healthy GPS signals, and the scintillated GPS signals. The profile of the scintillation is extracted from the real scintillated GPS data collected on Ascension Island in 2001. The scintillation profile is then loaded into the Spirent simulator by using the scintillation commands. As a result, the RF GPS signals from the Spirent will have the same scintillation profile as illustrated in Figure 1.1 on the previous page.

2. A high quality clock emulator. This an oven controlled crystal oscillator (OCXO) driven clock emulator which can emulate the clock signals that have phase noise above the intrinsic phase noise of the embedded OCXO. This emulator is used to emulate the aircraft vibration effects on the temperature compensated crystal oscillator (TCXO).

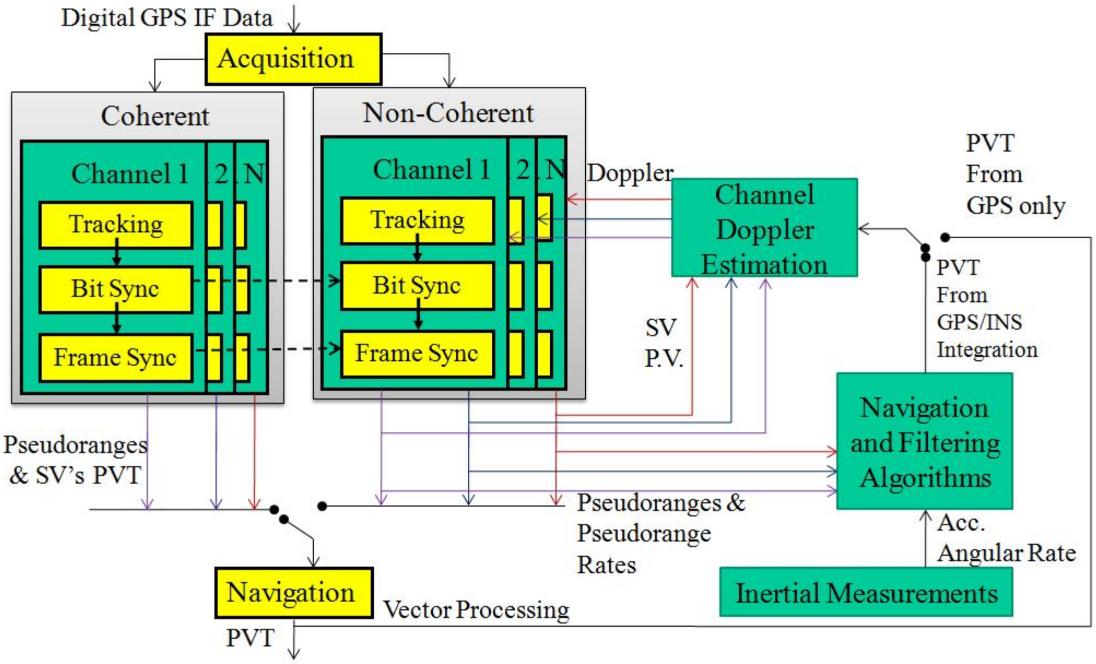

Figure 1.2: Doppler-Aided GPS Receiver, where SV is satellite vehicle; PVT is position, velocity, and time; SV P.V. means satellite vehicle's position and velocity; INS stands for inertial navigation system. Doppler aiding can also be used on the coherent channels.

A GPS receiver usually uses a TCXO for its reference frequency. A TCXO is sensitive to vibrations. The phase noise of a vibrated TCXO is higher than that of a static TCXO. To evaluate the performance of a GPS receiver used on an aircraft, one must consider the effects of the vibrations on the TCXO inside the GPS receiver. Therefore, we use this clock emulator to generate the desired clock signals. It is important to note that this clock emulator was made available to use by SiRF, Inc.

3. A NordNav front-end and ADC. This front-end is used to receive the RF GPS signals generated by the Spirent simulator. The output of the front-end is the digitized GPS signal at an intermediate frequency (IF). Importantly, this front-end can take an external clock signal as its reference frequency. Therefore, we connect this front-end to the clock emulator. By doing so, the vibration-affected clock signals are used as the reference frequency to down-convert and to sample the RF GPS signals from the Spirent simulator.

Having the above three key components, we can conduct a high fidelity hardware simulation of a GPS receiver used on an aircraft in the presence of ionospheric scintillation.

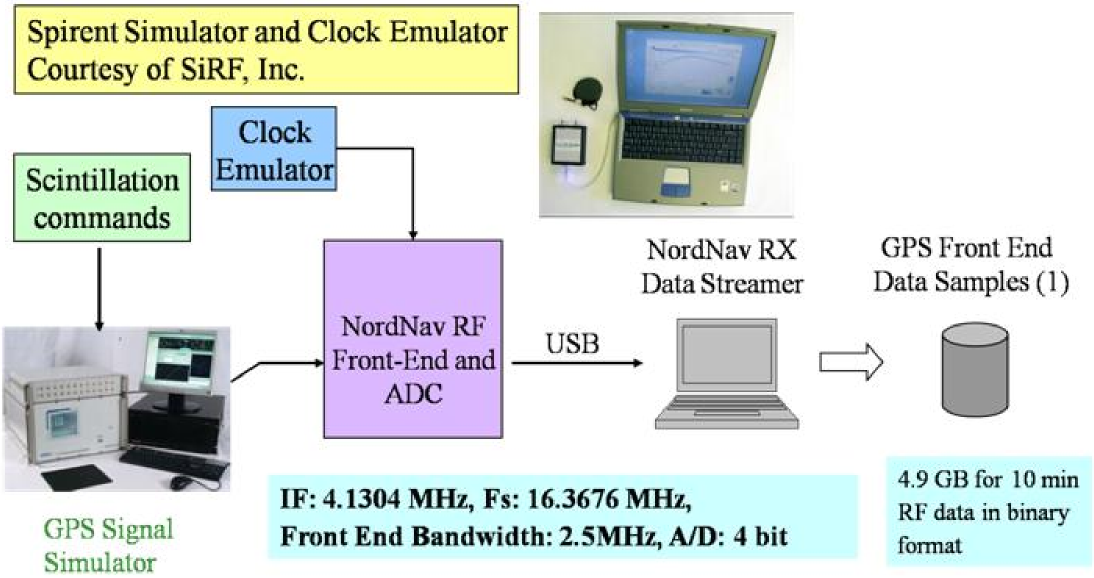

Figure 1.3: Enabling a hardware simulation

1.2 Prior Research

To evaluate the robustness of the tracking loops during ionospheric scintillation, both the errors due to scintillation and the generic tracking loop errors must be considered. Previous work in this area, in general, can be divided into two groups.

In the first group, a number of researchers have studied the effects of ionospheric scintillation on tracking loop performance [1, 3, 4, 5, 6, 7]. An excellent research effort was made by Knight [1] to evaluate the ionospheric scintillation effects on GPS receivers. The major contribution of Knight's research is to use a widely accepted stochastic model of scintillation activity to investigate the effects of scintillations on GPS receivers. The model is closely linked to the Wide Band Scintillation Model (WBMOD) [68]. The WBMOD can predict various statistical scintillation parameters based on empirically derived models of the global distribution and behavior of ionospheric scintillation. Knight also derived the expressions of carrier and code tracking errors as a function of scintillation parameters. Intensive model studies by Knight have provided the fundamentals for researchers who wish to further investigate overall receiver performance in the presence of scintillation. In addition, he determined the optimal parameters of the tracking loops as a function of scintillation strength. It is important to point out that a constant C/N_0, mostly 41.5 dB-Hz, is assumed for his studies. In his work, he evaluated the impact of various severities of scintillation on

GPS receiver given that C/N_0 is guaranteed mostly at 41.5 dB-Hz. However, the focus of this dissertation, which is different from Knight's approach, is to investigate the minimum allowable C/N_0 given specific conditions of the ionospheric scintillation. Assuming a condition of strong GPS signal strength (41.5 dB-Hz), Knight then concluded that the carrier tracking loops of full code correlation GPS receivers are quite robust to scintillations, even when the levels of scintillation activity are quite high [1]. However, the GPS signal strength is not always strong. We then are interested in determining the minimum allowable C/N_0 in the presence of scintillation. Furthermore, not all of the error sources are considered in his research. For example, the vibration effects of the receiver clock are not included in his analysis.

In addition to the linear model approach, extensive hardware testing has been conducted by Morrissey et al. [8], and [9]. Although tests were done on a static receiver, the results of these hardware tests demonstrated that a traditional GPS receiver is not robust to ionospheric scintillation. When a GPS receiver is subject to an accelerating and vibrating motion, the receiver will encounter more challenges in the presence of ionospheric scintillation than a static receiver.

The second group of researchers contributed to determining the tracking loop performance without considering ionospheric scintillation [12, 13, 14, 15, 16, 17, 18]. In particular, most attention in the previous work was focused on a phase-locked loop (PLL), i.e., a coherent tracking loop. Relatively few studies have been done on a frequency-locked loop (FLL), i.e., a non-coherent tracking loop. Under a condition of weak signals, it is difficult for a PLL to maintain phase locked. However, it is relatively easier for a FLL to maintain frequency locked given the same level of signal strength or even weaker signals. Therefore, this is an engineering trade off where a relatively lenient accuracy requirement provides more availability of a system. The attention is then moved to investigating if the use of an FLL can fulfill the accuracy requirement and to insure that the gain of increasing the availability is worth a loss in high accuracy, which a PLL provides. However, it should be noted that a PLL usually can not work well under a very weak signal condition we are dealing with in this research. Thus, an FLL becomes a potential candidate to sustain the function of a GPS receiver in severe scintillation environments.

The use of an FLL to strengthen a PLL was studied in [19] and [22]. A comprehensive FLL linear model study on the noise performance with different frequency discriminators was conducted in [19, 21]. More recently, in [23, 24] , the FLL linear model including various error sources was considered. The use of an FLL to cope with ionospheric scintillation was implemented to process simulated scintillation data in [11] . It was demonstrated in [11] that an FLL is effective for the cycle slip detection in scintillation environments. The key contributions from researchers of this group are constructing the linear models of the error sources, except for the ionospheric scintillation, for the GPS carrier tracking loop, especially for the PLL. Important findings from this group are the specific impacts of each error source on the carrier tracking loop. Given the conditions of signal strength, the platform dynamics, and the quality of the receiver clock, the optimal bandwidth of the carrier tracking loop can be determined. The technique of Doppler aiding to a PLL has also been studied by the researchers of this group. It was shown that the improvement of tracking sensitivity by applying Doppler aiding to a PLL is around 3 dB [13]. However, the impacts of ionospheric scintillation had not yet been studied when the work of evaluating the performance of a carrier tracking loop was done by the researchers of this group.

Thus far, we found that the performance of a GPS receiver in the presence of ionospheric scintillation has not yet been extensively studied. Researchers from the first group did not consider error sources that the researchers of the second group investigated. On the other hand, the impacts of scintillations were not covered in the studies from the second group. Therefore, my dissertation would like to do a comprehensive study on this problem; to investigate a new way of resolving the difficulties caused by scintillations on a GPS receiver; to develop a software receiver for implementing the proposed algorithms; and, to validate the effectiveness of the algorithms through the hardware simulations.

The previous literature has investigated the impact of scintillation on a PLL, but little attention has been paid to using an FLL to resolve scintillation problems. My dissertation will explore the advantage of using an FLL as well as an aided FLL to improve the robustness to scintillation. As will be seen in this work, an FLL is more robust to noise and dynamics than a PLL. However, an FLL provides more noisy measurements than a PLL does. An effective aiding scheme is considered to take advantage of an FLL without suffering from the noisy measurements provided by the FLL. The benefits of using an inertial-aided as well as vector processing carrier tracking loop in dealing with ionospheric scintillation have not been investigated either.

In this research, we attempt to provide an inclusive linear model analysis of both the

PLL and FLL by considering all of the generic tracking error sources as well as the errors due to ionospheric scintillation. The purpose is to determine whether the use of an FLL as a backup tracking loop could effectively overcome ionospheric scintillation.

1.3 Dissertation Objectives and Contributions

The bandwidth of the carrier tracking loop inside the GPS receiver is the main parameter, and we strive to reduce and optimize this parameter to surmount the aforementioned three challenges. In principle, lower bandwidth reduces the noise impact, but higher bandwidth is needed to track the clock and platform dynamics. Hence, this is a trade-off study focused on the bandwidth of the GPS receiver. To evaluate the performance of the designed GPS receiver for the concerned application under strong scintillation conditions, we have conducted the following analyses and implementations to assess the performance of the designed receiver.

1. To have high-fidelity GPS radio frequency (RF) data, we have built a realistic hardware simulation for emulating the aircraft landing using a GPS in a strong scintillation environment. The scintillation data were provided by the Air Force Research Lab (AFRL). AFRL collected scintillated GPS data on Ascension Island in 2001.

2. We have designed a GPS receiver which runs coherent and non-coherent tracking in parallel and have evaluated the performance of both tracking architectures.

3. The technique of Doppler-aiding is applied to both coherent and non-coherent tracking architectures.

4. Two Doppler-aiding sources are considered. The first technique is vector processing [2], and the second technique is tightly-coupled GPS/INS integration.

There are three main contributions made by this dissertation.

1. Developed and implemented a GPS hardware simulation for operation in environments which include aircraft dynamic, aircraft vibration-affected receiver clock, and strong ionospheric scintillation.

2. Validated tracking architectures in strong ionospheric scintillation environment.

3. Developed a nonlinear model for the non-coherent tracking loop and derived the probability density function (PDF) of frequency error. Having the PDF is the key to evaluate the bit error rate (BER), word error rate (WER), and the probability of failure of the navigation system. Solving for the PDF serves as the basis for future work on ascertaining the system performance in terms of availability, continuity, and integrity.

1.4 Dissertation Organization

The three main contributions of this dissertation are organized in four chapters as follows.

Chapter 2 analyzes the performance of a Doppler-aided GPS receiver using linear models. This is the analytical part of evaluating the impact of error sources of GPS carrier tracking loops. Through this process of linear model analysis, one can determine the optimal noise bandwidth of the carrier tracking loop. This chapter aims for comprehensive model study and derivations. The theoretical basis of this dissertation is provided in this chapter.

Chapter 3 describes how the high fidelity GPS hardware simulations are realized utilizing both real data and GPS simulator. This process serves as the GPS RF database generator. With the hardware simulation built, the designed GPS navigation system is then evaluated using the database.

Thus far, Chapter 2 presents the fundamental analysis of a Doppler-aided GPS receiver and Chapter 3 supplies the database for the validation of the analysis in Chapter 2. Chapter 4 develops specific ideas for providing the Doppler aiding. Chapter 4 implements a software GPS receiver including the two techniques of Doppler aiding, tightly-coupled inertial aiding and vector processing. This chapter presents and discusses the architecture of the designed receiver. The experimental results are also provided in this chapter to validate the aiding techniques based on GPS RF data from the hardware simulations.

Chapter 5 provides the second round of analytical research for this dissertation. In this chapter, a nonlinear model for the non-coherent loop is developed. The probability density function of frequency error is also solved using a numerical method.

Finally, Chapter 6 summarizes and concludes this research. Appendix A provides preliminary discussions of the word error rate calculations for a WAAS receiver under scintillation conditions. However, the investigations of the impacts of scintillation on WAAS is beyond the scope of this dissertation. The appendix prepares the starting point for the research in this topic.

Chapter 2

Performance of a Doppler-Aided GPS Receiver for Aviation in the Presence of Ionospheric Scintillation

2.1 Chapter Overview

In this chapter, the theoretical analysis of a Doppler-aided GPS receiver is covered. We assume that Doppler aiding is available, and Chapter 4 will develop specific sources for this aiding.

Ionospheric scintillation has a significant impact on the availability of the Global Positioning System (GPS), especially when the GPS receiver is dynamically stressed. This chapter investigates the tolerable thermal noise level, given various conditions of ionospheric scintillation and dynamic stress. Two important criteria are used to determine the tolerable wideband interference level: the tracking threshold and the word error rate (WER) of the navigation data demodulation. This chapter presents the quantitative improvement using the Doppler-aided FLL and compares it to the generic PLL as well as Doppler-aided PLL carrier-tracking loops. A theoretical model analysis was performed for the above various tracking-loop configurations, considering all of the possible error sources that could potentially degrade carrier-tracking loop performance. These errors include satellite/receiver clock dynamics, platform dynamics, platform vibrations, the sensitivity of the receiver clock to acceleration, wideband interference, and ionospheric scintillation. The results showed that by using a Doppler-aided FLL tracking loop, there is a 7 dB improvement in the minimum C/N_0 compared to a receiver using only a PLL as a primary tracking loop. However, satisfying the requirements of the WER limits the performance of this technique. For example, to have WER $< 10^{-4}$ for a PLL driven GPS receiver, the C/N_0 should be at least 28 dB-Hz [12, 61]. The same WER requirement for an FLL driven GPS receiver would need the C/N_0 to be at least 31 dB-Hz [61]. In the condition of strong scintillation, the C/N_0 is easily degraded to be lower than 28 dB-Hz. The details of the WER analysis will be provided in Section 2.6 on page 42.

2.2 An overview of a GPS receiver

This section provides a brief overview of a GPS receiver. Figure 2.1 illustrates a GPS receiver block diagram [26, p.432]. The transmitted L-band GPS signals are captured by the antenna. A signal-conditioning process is conducted by the front-end to down-convert the signals from radio frequency (RF) to an appropriate intermediate frequency (IF), such that the acquisition and tracking can be realized in the next step. After the tracking process, the code and carrier of the received GPS signal have been removed through steps of multiplying the replica code and carrier with the incoming signal, and accumulating the multiplication outputs.

The signal left at this step represents a stream of binary bits which originally modulated the GPS carrier signal at a rate of 50 bits per second. The process of determining the sign of the data bits is called data demodulation. How to read the sign of the data bits depends on the method of carrier tracking loop. At the data demodulation step, a binary phase shift keying (BPSK) demodulation is used if the carrier tracking loop is a PLL. In contrast, if an FLL is used for the carrier tracking loop, a differential phase shift keying (DPSK) demodulation is needed [21] and [27, p.381] . The current focus of Sections 2.4 and 2.5 is to discuss the carrier tracking loop. The carrier tracking loop can be a stand alone PLL, a Doppler-aided PLL, a stand alone FLL, or a Doppler-aided FLL. Note that a phase-locked loop (PLL), also called a coherent tracking loop, tracks the phase of the received GPS signal. In contrast, a frequency-locked loop (FLL), also called a non-coherent tracking loop, tracks the frequency of the received GPS signal.

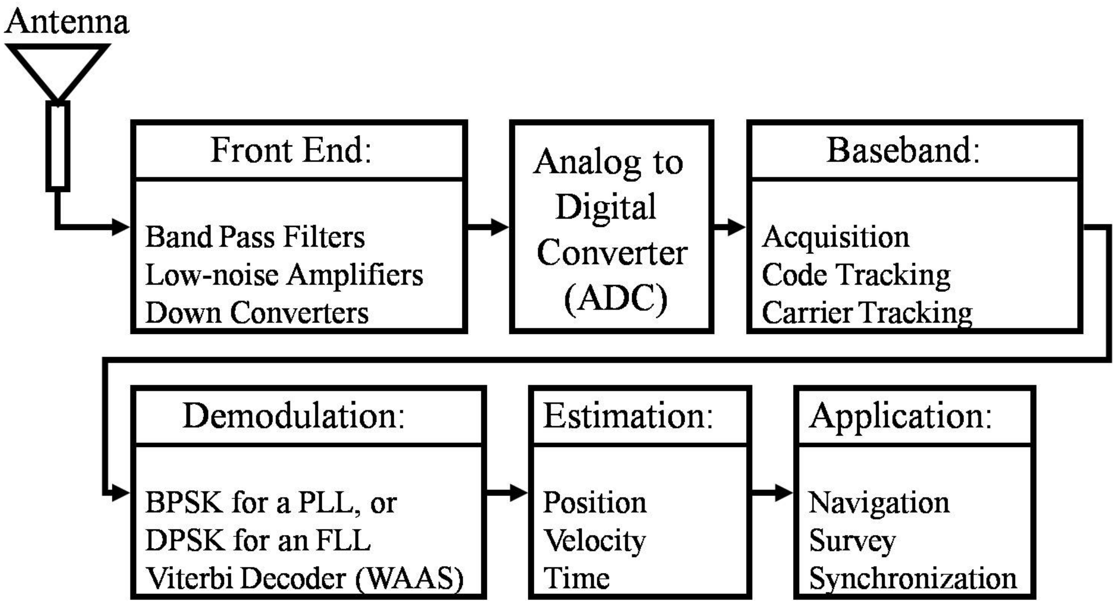

Figure 2.1: Block Diagram of GPS Receiver

2.3 Models of Scintillation

As mentioned in Section 1.1 on page 1, ionospheric scintillation can be decomposed into two components: phase scintillation and amplitude scintillation, which are defined by their power spectral densities (PSD) and probability density functions (PDF). In this section, we review the mathematical models of the aforementioned PSDs and PDFs. Characterizing the model of the ionospheric scintillation is not the purpose of this work. The focus of this chapter is to evaluate the improvements using an inertial-aided PLL or FLL, given the PSDs and PDFs of scintillation.

The PSD of phase scintillation follows an inverse power law, which is given in the following form [29] :

$$S_{\delta\phi_p}(f) = \frac{T_{sct}}{(f_0^2 + f^2)^{p/2}} \quad radians^2/Hz \tag{2.1}$$

where T_{sct} is the magnitude of the PSD at the frequency of 1 Hz; f is the frequency of phase fluctuations; f_0 is the frequency corresponding to the maximum irregularity size in the ionosphere; and, p is the slope of the PSD (usually in the range of 1 to 4 and typically 2.5). In this dissertation, we select the typical values for the constants in Eq.(2.1). $T_{sct} = -20\ dB - radians^2$, $f_0 = 10^{-1}\ Hz$, and $p = 2.5$ [1]. These typical values are given by

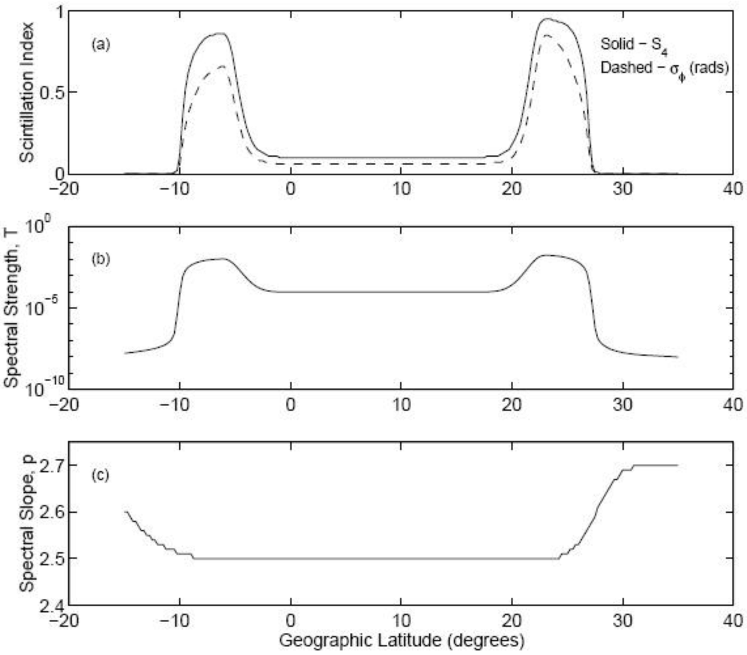

Figure 2.2: An example of the scintillation indices produced by WBMOD for a period of high solar activity, given by [1]

the results of the Wide Band ionospheric scintillation MODel (WBMOD, [68]). Knight [1] provided an example of the scintillation indices using WBMOD for a period of high solar activity, shown in Figure 2.2. Note that all plots are a function latitude at a longitude of $120^o\ E$ and are at the 70th percentile [1]. From Figure 2.2, we observe a strong correlation between the strength of amplitude scintillation, S_4 (definition of S_4 is provided in the next paragraph) and the strength of phase scintillation, T_{sct} (denoted as T in the plot). The maximum of T_{sct} is $-20\ dB - radians^2$ while S_4 is close to 0.9 . We also find that p stays at 2.5 till the strength of the scintillation reaches the two humps at $25^o\ N$ and $5^o\ S$. The parameter, f_0, is the frequency where phase scintillation is of no significance to a receiver. The dynamics below f_0 are within the capabilities of carrier tracking loops [6, 72, 73]. As a result, the spectral density begins at this cutoff frequency. Figure 2.3 illustrates the power spectral density described in Eq.(2.1) based on the aforementioned values for T_{sct}, f_0, and p. As will be seen in Chapter 3 on page 52, we included this simulated phase scintillation as part of the hardware simulation.

Before defining the PDF of the amplitude scintillation, an important parameter, S_4, describing the strength of the amplitude scintillation must be defined. S_4, the intensity scintillation index, is the normalized root mean square (RMS) intensity and is given by [1,

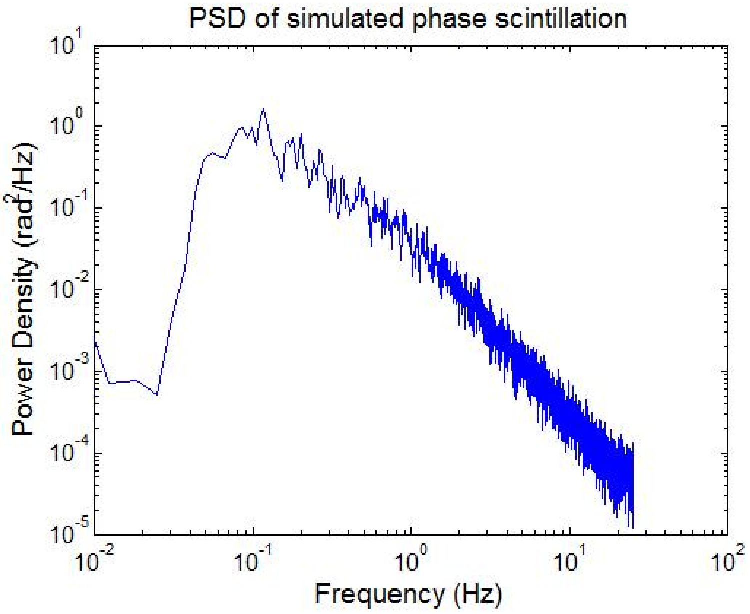

Figure 2.3: Power spectral density of simulated phase scintillation

p.45] and [10]

$$S_4 = \sqrt{\frac{\langle I^2 \rangle - \langle I \rangle^2}{\langle I \rangle^2}} \tag{2.2}$$

where I is the signal intensity, and $\langle \bullet \rangle$ is the expectation operator. Figures 2.4 and 2.5 depict the amplitude scintillation with high S_4 and low S_4, respectively. We see that with high S_4, the amount of fading and the rate of deep fadings is much higher than the amplitude scintillation with low S_4.

The PDF of the amplitude scintillation is modeled as a Nakagami-m distribution, which is given by [30]

$$f_A(A) = \frac{2m^m A^{2m-1}}{\Gamma(m) \langle A^2 \rangle^m} e^{-mA^2/\langle A^2 \rangle} \quad A \geq 0 \tag{2.3}$$

where A is the signal amplitude; $\Gamma(\bullet)$ is the Gamma function and m is defined as $m = {}^1\!/_{S_4^2}$. If we substitute $m = {}^1\!/_{S_4^2}$ into Eq.(2.3), we obtain the distribution in terms of S_4, which is shown in Eq.(2.4).

$$f_A(A) = \frac{2\left(\frac{1}{S_4^2}\right)^{\frac{1}{S_4^2}} A^{2\frac{1}{S_4^2}-1}}{\Gamma\left(\frac{1}{S_4^2}\right) \langle A^2 \rangle^{\frac{1}{S_4^2}}} e^{-\frac{1}{S_4^2} A^2/\langle A^2 \rangle} \quad A \geq 0 \tag{2.4}$$

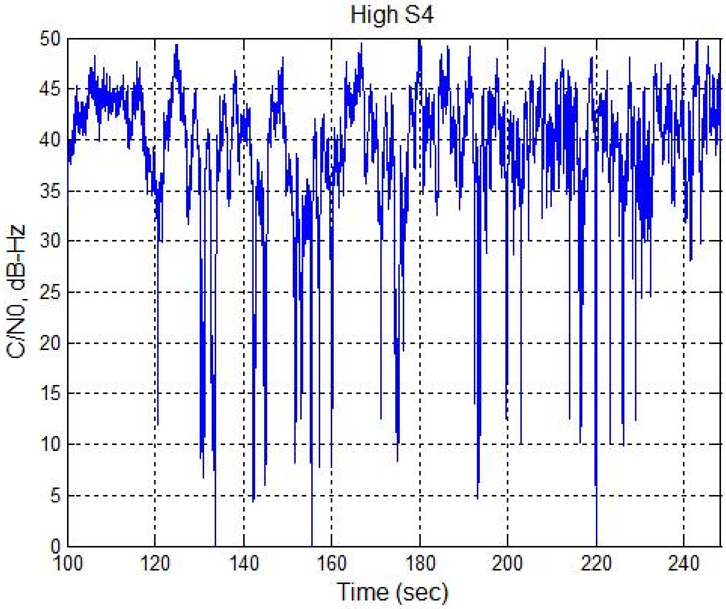

Figure 2.4: Amplitude scintillation with high S_4

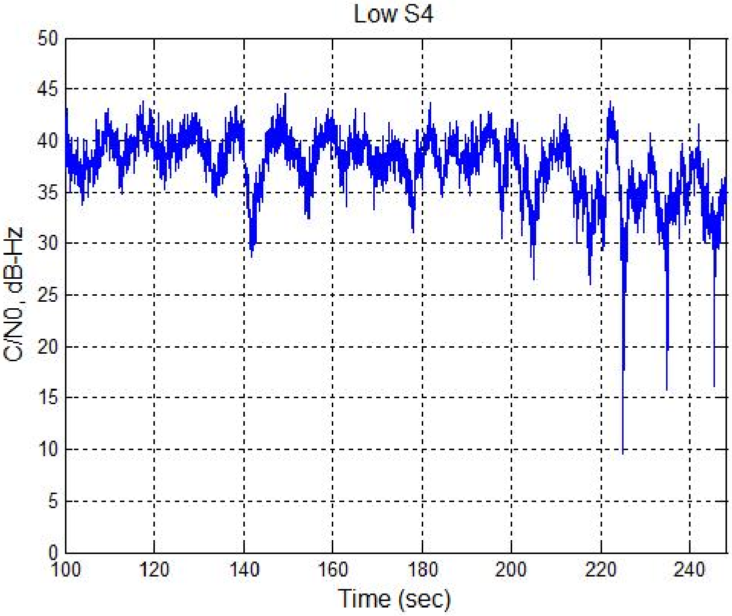

Figure 2.5: Amplitude scintillation with low S_4

Given the mean square amplitude, $\langle A^2 \rangle$, and the m parameter, the Nakagami-m distribution for the amplitude scintillation is well defined. As will be seen in the next section, the largest allowable value of S_4 in the linear model analysis is $\frac{1}{\sqrt{2}}$. It should be noted that for a very strong scintillation condition, S_4 could reach a value larger than 1.0. Different researchers may use different values of S_4 to describe the scintillation conditions. For example, Hegarty [69] characterized a moderate/strong scintillation when $S_4 \geqq 0.7$. Furthermore, Pullen [6] defined moderate scintillation as $S_4 = 0.7$. In addition, Van Dierendonck [10] conducted comprehensive S_4 measurements using SBAS signals in the equatorial region in 2004. The data he collected indicated moderate amplitude scintillation activity and the S_4 values were up to 0.65. Note that 2004 did not represent a period of high Solar Maximum. Figure 2.2 on page 15 also demonstrates a strong scintillation with S_4 from 0.7 to 0.9. Therefore, $S_4 = 0.7$ would be suitable for characterizing a moderate/strong scintillation condition. Although this is not the best value for describing a strong scintillation, $S_4 = \frac{1}{\sqrt{2}}$ represents the most severe scintillation for the linear model analysis in the following section. As will be seen in Subsection 2.4.1 on page 22, the phase error due to amplitude scintillation when $S_4 = \frac{1}{\sqrt{2}}$ is infinity.

In consequence, the estimated phase or frequency variance caused by the amplitude scintillation will be presented in terms of S_4 in Subsection 2.4.1 on page 22. While one is evaluating the bit error rate (BER) in the presence of amplitude scintillation, the PDF, i.e., Eq.(2.3), should be applied (details will be provided in Subsection 2.6.2 on page 46).

As for determining the estimated phase or frequency variance caused by the phase scintillation, one will use the PSD shown in Eq.(2.1). Subsections 2.4.5 and 2.5.4 will demonstrate the details for the errors caused by the phase scintillation.

Thus far, the error sources originating from scintillation have been described. In the following two sections (Sections 2.4 and 2.5), the PLL linear model analysis and FLL linear model analysis will be provided, respectively.

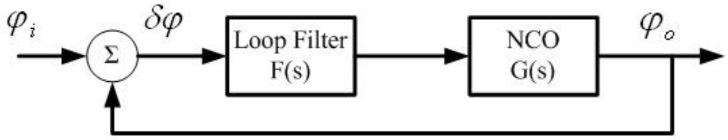

Figure 2.6: PLL Linear Model

2.4 Performance of a GPS Receiver with a Doppler-Aided Phase-Locked Loop

In this section, a PLL (a coherent tracking loop) linear model analysis is discussed. Discussions of the generic linear model analysis can be found in [13]. We would like to address the error sources that were not previously discussed. Likewise, providing the fundamental framework on the PLL linear model analysis would be helpful in the understanding of the FLL (a non-coherent tracking loop) analysis in the subsequent section. A short discussion of the functions of a PLL was given in [17]. To analyze the phase error of a PLL, the linear model illustrated in Figure 2.6 is considered. The input, φ_i, is the phase of the incoming digital IF signal. The output, φ_o, is the phase steered by the PLL to track the input φ_i. The summation symbol in Figure 2.6 represents the phase discriminator. Thus, $\delta\varphi$ is the phase error between φ_i and φ_o. $G(s)$ is the open loop transfer function of the numerically controlled oscillator (NCO). In the language of control, it is the plant or system to be controlled. Therefore, $G(s)$ represents a pure integrator, which can be represented by $1/s$. $F(s)$ is the controller, for which we design the parameters to control the bandwidth of the overall closed-loop. Ideally, $\delta\varphi$ stays exactly at zero once the phase is locked in. However, the incoming phase signal, φ_i, is influenced by thermal noise, the dynamics of the platform, ionospheric scintillation, and even satellite clock dynamics. Furthermore, the replica carrier phase, φ_o, is affected by receiver clock dynamics and the extra phase instability induced by the platform vibration. As a result, the phase error source includes thermal noise, platform dynamics stress error, receiver and satellite clock dynamics, and the oscillator's frequency error induced by platform vibrations.

A higher bandwidth PLL performs better in tracking the dynamics. However, a higher bandwidth PLL suppresses noise ineffectively. Specifically, the standard deviation value (1-sigma) of the steady-state phase error is used as a metric to characterize the performance of the PLL alone or the inertially-aided PLL. The 1-sigma phase error is also called phase jitter [28] , which is represented by

$$\sigma_{\delta\varphi} = \sqrt{\sigma^2_{\delta\varphi\omega} + \sigma^2_{\delta\varphi sv} + \sigma^2_{\delta\varphi rx} + \sigma^2_{\delta\varphi v} + \sigma^2_{\delta\varphi p}} + \frac{\theta_e + \theta_{acc}}{3} \quad radians \tag{2.5}$$

where

$\sigma_{\delta\varphi\omega}$= phase jitter from thermal noise and amplitude scintillation (if applied);

$\sigma_{\delta\varphi sv}$= phase jitter from the instability of the satellite's oscillators;

$\sigma_{\delta\varphi rx}$= phase jitter from the instability of the receiver's oscillators;

$\sigma_{\delta\varphi v}$= the vibration induced phase jitter;

$\sigma_{\delta\varphi p}$= phase jitter caused by phase scintillation;

θ_e= dynamic stress in the PLL tracking loop; and,

θ_{acc}= the excessive bias phase error induced by the acceleration sensitivity of the local oscillator.

The phase jitter in Eq.(2.5) consists of the statistical part (terms inside the square root) and the deterministic part (terms outside the square root). Evaluating the deterministic errors of the phase jitter is done by using the final value theorem, which can be found in fundamental control texts. The details of calculating the deterministic part will be demonstrated in Subsections 2.4.6, 2.4.7, and 2.4.8. On the other hand, evaluating the statistical part of the phase jitter can be done by spectral density analysis through the transfer function in the frequency domain. If we find the transfer function from φ_i to φ_o shown in Figure 2.6, we also find the corresponding closed-loop transfer function, $H(s)$. φ_i is the incoming carrier phase corrupted by the thermal noise or amplitude scintillations. To evaluate the filtered noise in φ_o caused by the thermal noise or amplitude scintillations, we need to calculate the power spectral density of φ_o. Given the power spectral density of the input signal ($S_\omega(f)$), the relation between the input power spectral density, the output power spectral density ($S_{\delta\varphi}(f)$), and the system frequency response ($H(j2\pi f)$) is given as follows.

$$S_{\delta\varphi}(f) = \left| H\left(j2\pi f\right)\right|^2 S_\omega\left(f\right) \tag{2.6}$$

In consequence, the variance of φ_o caused by thermal noise is the total area under $S_{\delta\varphi}(f)$, described in Eq.(2.6). Similarly, given the closed-loop transfer function ($H(s)$), the transfer function from $\delta\varphi$ to φ_o would be $1 - H(s)$. The statistical terms in Eq.(2.5), other than thermal noise and amplitude scintillation, belong to this category. Therefore, the power spectral density at the phase error estimate caused by these error sources is evaluated by $|1 - H(j2\pi f)|^2 S_{\delta\phi}(f)$. As a result, the phase jitter (deterministic terms not included) of the system in Figure 2.6 can be written as the following equation.

$$\sigma_{\delta\varphi}^2 = \int_0^\infty \left(|H(j2\pi f)|^2 S_\omega(f) + |1 - H(j2\pi f)|^2 S_{\delta\phi}(f) \right) df \tag{2.7}$$

where $H(j2\pi f)$ is the closed-loop transfer function of the linear model shown in Figure 2.6; $S_\omega(f)$ is the power spectral density of the phase noise from thermal noise or the amplitude scintillation; and, $S_{\delta\phi}(f)$ is the power spectral density of the additional phase noise from satellite and receiver oscillators or the phase scintillation. Eq.(2.7) is the key equation throughout the whole chapter. All of these statistical errors are evaluated using Eq.(2.7). For the carrier tracking loop, $H(s)$ is a low-pass filter and therefore $1 - H(s)$ is a high-pass filter. Reducing the bandwidth of $H(s)$ actually increases the bandwidth of $1 - H(s)$. Thus, the two parts in Eq.(2.7) have contradictive results when changing the bandwidth of $H(s)$. This reveals the main idea of the tracking loop design, that is, to determine the optimal bandwidth such that $\sigma_{\delta\varphi}^2$ reaches a minimum value. The work of this chapter is to determine the power spectral density of each error source in Eq.(2.5) on the facing page. Next, evaluate the final variance using Eq.(2.7). Finally, we resolve the optimized bandwidth which meets the balance for all of the error sources.

By definition, the closed-loop transfer function is written as

$$H(s) = \frac{\varphi_o}{\varphi i} = \frac{G(s) F(s)}{1 + G(s) F(s)} \tag{2.8}$$

It can be calculated that [17]

$$|1 - H(j2\pi f)|^2 = \frac{f^{2k}}{f_n^{2k} + f^{2k}} \tag{2.9}$$

where k is the order of the closed-loop and f_n is the natural frequency of the closed loop in Hz. Note that Eq.(2.9) represents the common optimized closed-loop transfer function [3, 27]. Eq.(2.9) is true for those transfer functions of $H(s)$ being in the optimized closed-loop and true for k being 1, 2, and 3 [27]. "Optimized closed-loop" means that, for example, the damping ratio of the second order $H(s)$ (i.e., $k = 2$) is $\frac{1}{\sqrt{2}}$.

Since the overall transfer function is a low pass filter, from Eq.(2.7) we can see that reducing the bandwidth of the loop rejects more thermal noise, but unavoidably induces more phase error contributed by the additional phase noise due to the oscillator's dynamics or the phase scintillation. As a result, it is a convex problem. There is a minimum allowable one-sided noise bandwidth, B_n, such that the lowest tolerable C/N_0 is achieved.

In the remainder of this section, the mathematical representation of each error source will be provided. The overall errors will be computed and presented at the end of this section (Subsection 2.4.9) and the determinations of the optimized bandwidth will be discussed in Chapter 4.

2.4.1 Thermal Noise and Amplitude Scintillation ($\sigma_{\delta\varphi\omega}$)

The thermal noise tracking error of a PLL with a dot-product phase discriminator in the presence of amplitude scintillation is derived in [1, p.105] and [31], and is given as

$$\sigma_{\delta\varphi\omega}^2 = \frac{B_n}{\frac{C}{N_0}(1-S_4^2)}\left[1+\frac{1}{2T_{coh}\frac{C}{N_0}(1-2S_4^2)}\right] \quad radians^2 \tag{2.10}$$

where

B_n is the PLL one-sided noise bandwidth in Hz;

$\frac{C}{N_0}$ is the signal-to-noise power density ratio;

T_{coh} is the coherent integration time in seconds, 0.02s for GPS; and,

$S_4 < \frac{1}{\sqrt{2}}$ for the L1 signal.

As shown, S_4 must be less than $\frac{1}{\sqrt{2}}$. This artifact arises because of the assumptions used in developing Eq.(2.10). Eq.(2.10) is derived based on an assumption of using the ideal AGC, which has the AGC gain factor equal to the squared signal amplitude at the end of the coherent integration (i. e., I^2+Q^2) [1]. Other types of AGC were also analyzed by Knight [1] and his results suggested using the model with the ideal AGC. Other model results using the other types of AGC may tolerate higher values of S_4. For example, using a slow AGC would have the phase error variance only affected by amplitude scintillation when S_4 is very close to 1 (details in [1]). However, using the slow AGC would substantially increase the phase error caused by phase scintillations and dynamics. However, Conker [31] also suggested the model using the ideal AGC. Therefore, the limited range of S_4 that could be applied for the model given in Eq.(2.10) is unavoidable.

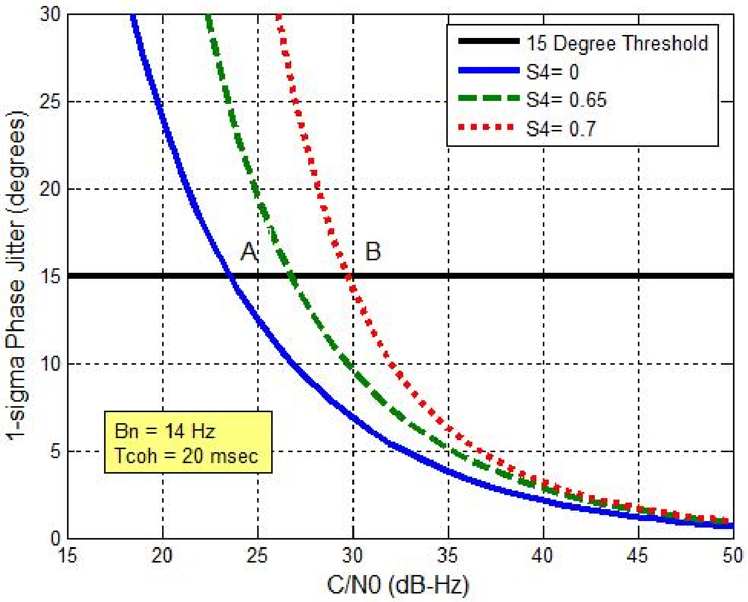

Figure 2.7: Phase jitter caused by thermal noise and amplitude scintillation

If there is no amplitude scintillation, $S_4 = 0$, Eq.(2.10) becomes the standard thermal-noise tracking error for the PLL [27]

$$\sigma^2_{\delta\varphi\omega} = \frac{B_n}{\frac{C}{N_0}}\left[1 + \frac{1}{2T_{coh}\frac{C}{N_0}}\right] \quad radians^2 \tag{2.11}$$

Figure 2.7 demonstrates the results of Eq.(2.10) with $B_n = 15$ Hz and $T_{coh} = 0.02$ sec. From Figure 2.7, we see that if $S_4 = 0.7$ instead of $= 0$, the minimum allowable C/N_0 is degraded by 6 dB (from point A to point B in the figure). It is desired to reduce the loop bandwidth to tolerate the extra jitter caused by amplitude scintillation. However, as will be seen in coming sections, all of the remaining error sources enlarge the phase jitter when the loop bandwidth decreases. A trade-off should be made to find the optimal bandwidth. From Subsection 2.4.2 forward, we will introduce the analysis of the remaining error sources of the phase jitter (shown in Eq.(2.5) on page 20).

2.4.2 Receiver Oscillator Phase Noise ($\sigma_{\delta\varphi rx}$)

The second phase error source is caused by the receiver oscillator phase noise, especially at a low noise bandwidth. One can increase the noise bandwidth such that the PLL can track the clock dynamics. However, a higher noise bandwidth introduces more effects on the phase error caused by the thermal noise. Therefore, to determine an appropriate noise bandwidth, we must ascertain the carrier phase-noise spectrum. The phase-noise power spectral density (PSD) (one-sided) of an oscillator can be written as [32]

$$W_{\delta\phi rx}(f) = \sum_{i=-4}^{0} h_i f^i \quad f_l \leq f \leq f_h \quad radians^2/H^z \tag{2.12}$$

The lower bound of the frequency range, f_l , can be set to be 0 without losing any generality [32] . The upper bound of the frequency range, f_h , can be exceedingly large, but it will be limited by the pre-detection integration (PDI) bandwidth (or coherent integration time) of the receiver. This is because the pre-detection integration is a low-pass filtering process. Any frequency contents beyond the PDI bandwidth would be negligible. Therefore, by definition, $f_h = {}^1\!/_{2T_{coh}}$ in Hz.

$W_{\delta\phi rx}(f)$ is the baseband spectrum of the phase noise, $\phi(t)$ [33] , which is also known as the spectral density of the phase fluctuations [34] . It is important to note that $W_{\delta\phi rx}(f)$ is the PSD defined at the oscillator's center frequency, f_0 . In fact, the actual phase noise PSD experienced by the tracking loop should be the PSD at the received signal frequency, for example, the GPS L1 frequency (f_{L1}). To elaborate, we define a multiplication factor between the received carrier frequency ($f_{carrier}$) and the local oscillator's center frequency (f_0) to be

$$N = \frac{f_{carrier}}{f_0} \tag{2.13}$$

In this work, $f_{carrier} = f_{L1}$. As a result, the phase noise PSD at the input of the carrier tracking loop should be

$$S_{\delta\phi rx}(f) = N^2 W_{\delta\phi rx}(f) \quad radians^2/Hz \tag{2.14}$$

To illustrate this magnification effect on the phase noise, let us assume that the oscillator's center frequency is 10.23 MHz. Therefore, N = 154 for the L1 signal. The final phase noise PSD at f_{L1} is increased by $20log_{10}(N) = 43.75dB$ from the original noise PSD at f_0. One should remember that the phase noise PSD is defined at a specific center frequency.

In order to complete the analysis here, the coefficients h_i in Eq.(2.12) must be found for a given oscillator. However, what is listed in the specification sheet of an oscillator is not the phase noise PSD defined in Eq.(2.12). The specification sheet usually specifies the single-sideband (SSB) phase noise, $L\left(\triangle f\right)$, which is typically expressed in a decibel format as $10\log_{10}\left[L\left(\triangle f\right)\right]$ dBc/Hz [33, 34]. As stated in [33], *"dBc means ,'dB relative to carrier,' where the term carrier actually means total power in the signal; 'per Hz' refers to a bandwidth of 1 Hz."* $L\left(\triangle f\right)$ is the normalized version of the theoretical passband spectrum of the oscillator signal [33]. A more concise definition of $L\left(\triangle f\right)$ given in [33, p.147] is that *"$L\left(\triangle f\right)$ is the noise power, relative to the total power in the signal, in a bandwidth of 1 Hz in a single sideband at a frequency offset of $\triangle f$ from the carrier frequency f_0."* The relationship between $W_{\delta\phi rx}(f)$ and $L\left(\triangle f\right)$ can be defined only if the following statement is true. The phase fluctuations at frequencies greater than the offset frequency are much less than 1 *radians*^{2} [34]. In other words, if the phase-noise amplitude is small enough, the following equation holds [36]

$$L\left(\triangle f\right) \approx \frac{W_{\delta\phi rx}\left(f\right)}{2} \tag{2.15}$$

Through the relation in Eq.(2.15), we can find the coefficients, h_i , in Eq.(2.12) based on the given SSB in the specification sheet of an oscillator. Table 2.1 on the next page shows the SSB phase noise ($L\left(\triangle f\right)$) for several types of oscillators and Table 2.2 on page 27 shows the resolved coefficients, h_i , for $W_{\delta\phi rx}(f)$. Nevertheless, as mentioned in [33, p.150], *"the phase noise amplitude is never small enough at frequencies close in to the carrier frequency, so $W_{\delta\phi rx}(f)$ is never a good representation of the close-in $L\left(\triangle f\right)$, the close-in RF sidebands."* Since the process of the phase noise due to oscillators through the tracking is a high pass filtering process, this discrepancy may not be pronounced. The large discrepancies at low frequency ranges, i.e., close to the carrier frequency, will be filtered out. If the noise bandwidth of the tracking is quite small (much less than 1 Hz), the imperfect phase noise model begins to degrade the results predicted by this analysis. Hence, the tracking error due to oscillator dynamics is an approximate result but it is currently the best solution one can obtain.

Given the PSD in Eq.(2.14), we can find the phase jitter from the oscillator's dynamics by evaluating the second integrand in Eq.(2.7) as follows:

$$\sigma^2_{\delta\varphi rx} = \int\limits_0^\infty \left|1 - H\left(j2\pi f\right)\right|^2 S_{\delta\phi rx}\left(f\right) df \tag{2.16}$$

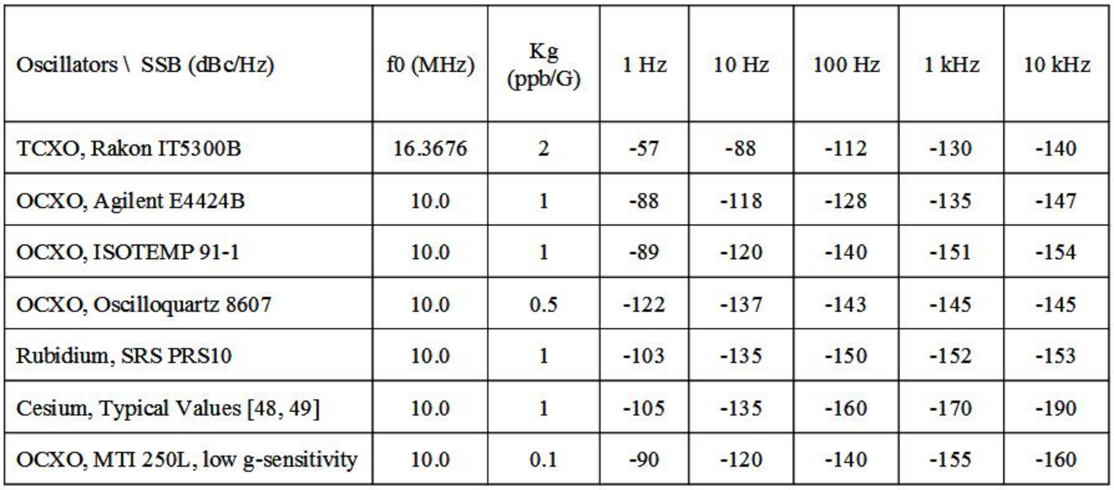

Oscillators \ SSB (dBc/Hz)	f0 (MHz)	Kg (ppb/G)	1 Hz	10 Hz	100 Hz	1 kHz	10 kHz
TCXO, Rakon IT5300B	16.3676	2	-57	-88	-112	-130	-140
OCXO, Agilent E4424B	10.0	1	-88	-118	-128	-135	-147
OCXO, ISOTEMP 91-1	10.0	1	-89	-120	-140	-151	-154
OCXO, Oscilloquartz 8607	10.0	0.5	-122	-137	-143	-145	-145
Rubidium, SRS PRS10	10.0	1	-103	-135	-150	-152	-153
Cesium, Typical Values [48, 49]	10.0	1	-105	-135	-160	-170	-190
OCXO, MTI 250L, low g-sensitivity	10.0	0.1	-90	-120	-140	-155	-160

Table 2.1: Single-Sideband (SSB) Phase Noise Specifications of Oscillators

Substituting Eqs. (2.9) and (2.14) into Eq.(2.16), we obtain the phase jitter from the oscillator's dynamics, only in terms of the PLL noise bandwidth, B_n , as follows [17]:

For a second order PLL ($k = 2$),

$$\sigma^2_{\delta\varphi rx} = N^2[X^3 h_4 \frac{\pi}{2\sqrt{2}} + X^2 h_3 \frac{\pi}{4} + X h_2 \frac{\pi}{2\sqrt{2}}] \quad radians^2 \tag{2.17}$$

where $X = \frac{2\pi}{1.8856 B_n}$, and N was defined in Eq.(2.13);

and for a third order PLL ($k = 3$),

$$\sigma^2_{\delta\varphi rx} = N^2[Y^3 h_4 \frac{\pi}{6} + Y^2 h_3 \frac{\pi}{3\sqrt{3}} + Y h_2 \frac{\pi}{3}] \quad radians^2 \tag{2.18}$$

where $Y = \frac{2\pi}{1.2 B_n}$, and N was defined in Eq.(2.13).

Note that the unit of B_n is Hz.

2.4.3 Satellite Oscillator Phase Noise ($\sigma_{\delta\varphi sv}$)

In addition to the receiver oscillator on earth that produces phase noise, the clock onboard the satellite in orbit could also generate phase noise in the signals. The nominal satellite oscillator PSD was not available. However, it was promised by the ICD of GPS that the phase jitter from satellite oscillator's dynamics would be less than 0.1 radians when B_n is 10 Hz [35]. As shown in [13], this specification is somewhat conservative. We use a typical specification of a Cesium clock as listed in Table 2.1 to model the satellite oscillator's

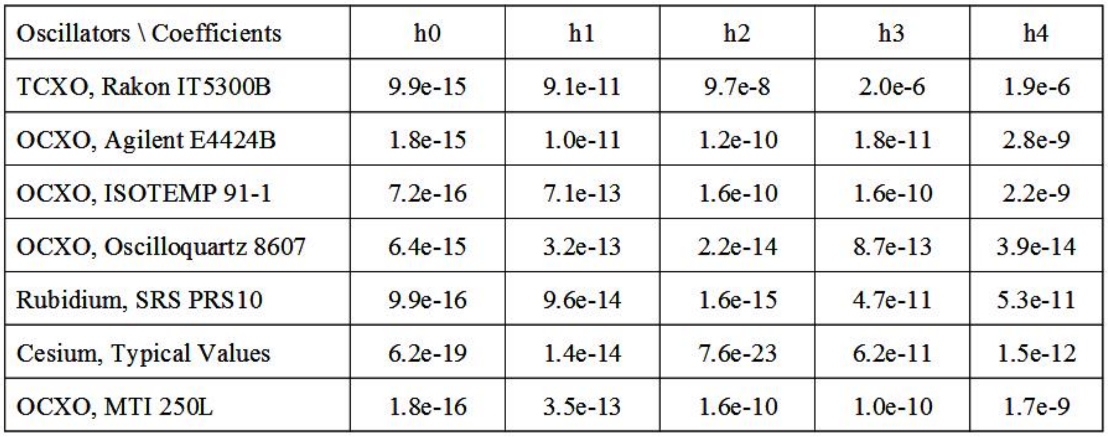

Oscillators \ Coefficients	h0	h1	h2	h3	h4
TCXO, Rakon IT5300B	9.9e-15	9.1e-11	9.7e-8	2.0e-6	1.9e-6
OCXO, Agilent E4424B	1.8e-15	1.0e-11	1.2e-10	1.8e-11	2.8e-9
OCXO, ISOTEMP 91-1	7.2e-16	7.1e-13	1.6e-10	1.6e-10	2.2e-9
OCXO, Oscilloquartz 8607	6.4e-15	3.2e-13	2.2e-14	8.7e-13	3.9e-14
Rubidium, SRS PRS10	9.9e-16	9.6e-14	1.6e-15	4.7e-11	5.3e-11
Cesium, Typical Values	6.2e-19	1.4e-14	7.6e-23	6.2e-11	1.5e-12
OCXO, MTI 250L	1.8e-16	3.5e-13	1.6e-10	1.0e-10	1.7e-9

Table 2.2: Coefficients of Oscillator's PSD

dynamics. The expression for $\sigma_{\delta\varphi sv}$ is the same as those in Eqs. (2.17) and (2.18) except that the coefficients, h_i , were taken from Table 2.2 for the Cesium clock.

2.4.4 Vibration Induced Phase Jitter ($\sigma_{\delta\varphi v}$)

The phase jitter induced by the platform vibration can be calculated by

$$\sigma^2_{\delta\varphi v} = \int\limits_0^\infty \left|1 - H\left(j2\pi f\right)\right|^2 S_{\delta\phi v}\left(f\right) df \quad radians^2 \tag{2.19}$$

where $S_{\delta\phi v}\left(f\right)$ is the PSD of the phase noise induced by the platform vibrations. $S_{\delta\phi v}\left(f\right)$ can be further expressed as [27]

$$S_{\delta\phi v}\left(f\right) = \left(k_g N f_0\right)^2 \frac{G_g\left(f\right)}{f^2} \tag{2.20}$$

where k_g is the oscillator's acceleration-sensitivity in parts/g (values given in Table 2.1 on the preceding page); f_0 is the center frequency of the oscillator (values given in Table 2.1 on the facing page); N has been defined in Eq.(2.13); and, $G_g(f)$ is the one-sided vibration spectral density in ${}^{g^2}\!/_{Hz}$. The most up-to-date vibration spectral density curve for an instrument panel installation on a turbojet aircraft is shown in Figure 2.8 [37]. Figure 2.8 also shows a vibration spectrum of an automobile (sedan) under normal driving conditions [15]. Table 2.3 summarizes the two curves in Figure 2.8. Eq.(2.19) was evaluated numerically in this work.

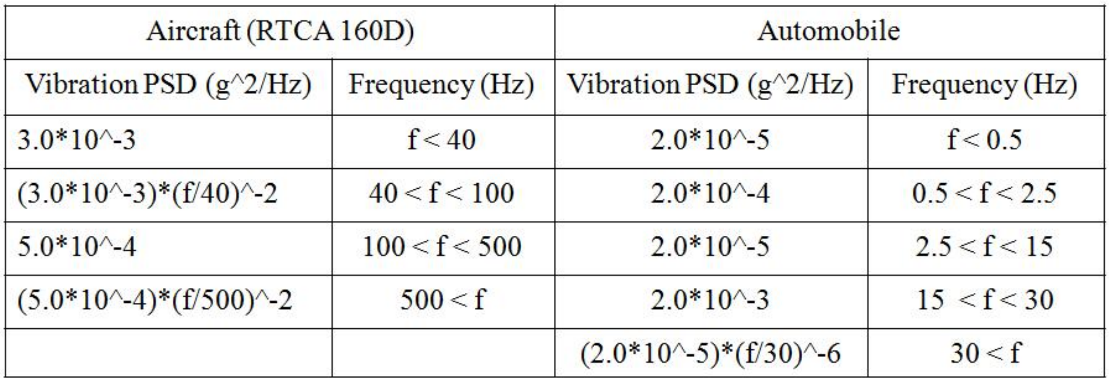

Aircraft (RTCA 160D)		Automobile	
Vibration PSD (g^2/Hz)	Frequency (Hz)	Vibration PSD (g^2/Hz)	Frequency (Hz)
3.0*10^-3	f < 40	2.0*10^-5	f < 0.5
(3.0*10^-3)*(f/40)^-2	40 < f < 100	2.0*10^-4	0.5 < f < 2.5
5.0*10^-4	100 < f < 500	2.0*10^-5	2.5 < f < 15
(5.0*10^-4)*(f/500)^-2	500 < f	2.0*10^-3	15 < f < 30
		(2.0*10^-5)*(f/30)^-6	30 < f

Table 2.3: Vibration PSDs

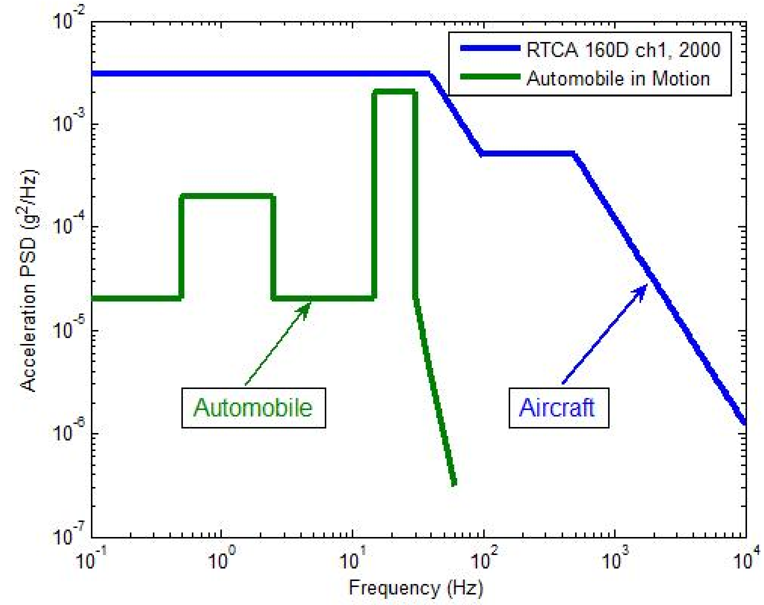

Figure 2.8: Vibration PSDs: The PSD of the aircraft is given by RTCA 160D[37] and the PSD of the automobile is provided by Alban's dissertation in 2004[15]. The two resonances in the automobile PSD are the body mode and the wheel-hop mode around 1 Hz and 20 Hz, respectively[15].

2.4.5 Phase Jitter from Phase Scintillation ($\sigma_{\delta\varphi p}$)

Likewise, the phase jitter induced by the ionospheric phase scintillation is determined by substituting Eq.(2.1) into the second integrand of Eq.(2.7) on page 21 as

$$\sigma^2_{\delta\varphi p} = \int_0^\infty \left|1 - H\left(j2\pi f\right)\right|^2 S_{\delta\phi p}\left(f\right) df \quad radians^2 \tag{2.21}$$

The result of Eq.(2.21) in a closed form was elaborated upon in [1, 3, 29] with constraints imposed on the slope index p depending on the order of the closed loop PLL. The closed form solution of Eq.(2.21) is given as [3]

$$\sigma^2_{\delta\varphi p} = \frac{\pi T_{sct}}{k f_n^{p-1} sin\left(\frac{[2k+1-p]\pi}{2k}\right)} \quad for \;\; 1 < p < 2k \tag{2.22}$$

where

T_{sct} is the magnitude of the phase scintillation PSD at the frequency of 1 Hz;

k is the order of the closed-loop;

f_n is the natural frequency of the closed loop in Hz; and,

p is the slope of the phase scintillation PSD (usually in the range of 1 to 4 and typically 2.5).

In this research, p is set at 2.5, which is a valid value based on the current data analysis [1]. More experimental results from measuring phase scintillation spectral density also suggested that p is close to 2.5 [8, 68, 70, 71]. Physically, we would see that the spectral density decays 25 dB per decade. If $T_{sct} = -20$ $(dB - radians^2)$, then the power of phase scintillation at 10 Hz would be -45 $(dB - radians^2)$. From Eq.(2.22), we see that to have smaller $\sigma^2_{\delta\varphi p}$, we need to enlarge f_n. However, increasing f_n introduces much thermal noise into the system.

2.4.6 Dynamic Stress in the PLL (θe)

Because of the abrupt motion, the PLL experiences excessive phase error. Of interest is the peak error, i.e., the transient phase error response of the phase acceleration or phase jerk. For the second-order loop, the phase error due to dynamic stress (phase acceleration) is bounded by [28, p.180]

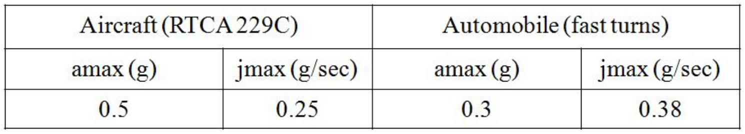

Aircraft (RTCA 229C)		Automobile (fast turns)	
amax (g)	jmax (g/sec)	amax (g)	jmax (g/sec)
0.5	0.25	0.3	0.38

Table 2.4: Accelerations and Jerks

$$\theta_{e2} = \frac{\overset{\bullet}{\triangle} f}{\omega_n^2} \quad cycles \tag{2.23}$$

where $\overset{\bullet}{\triangle} f$ is a frequency ramp input in Hz/sec, and ω_n is the natural frequency of the closed loop in rad/sec. Converting the frequency ramp input into the phase acceleration along the line-of-sight direction, we have [17]

$$\theta_{e2} = \frac{\overset{\bullet}{\triangle} f}{\omega_n^2} \cong 2\pi \frac{2.7599 a_{max}}{\lambda_{carrier} B_n^2} \quad radians \tag{2.24}$$

where a_{max} is the maximum value of line-of-sight phase acceleration in g, and $\lambda_{carrier}$ is the wavelength of the carrier in meters.

Furthermore, for the third-order loop, the phase error resulting from the dynamic stress (phase jerk) is given by [27, p.390]

$$\theta_{e3} = 2\pi \frac{\overset{\bullet\bullet}{\triangle} f}{\omega_n^3} \cong 2\pi \frac{5.67 j_{max}}{\lambda_{carrier} B_n^3} \quad radians \tag{2.25}$$

where j_{max} is the maximum value of line-of-sight jerk experienced by the receiver in g/sec. In [25], a_{max} and j_{max} have been defined to regulate the performance of the GPS receivers used in aviation. Table 2.4 provides the values of a_{max} and j_{max} for aircraft and normal driving automobiles (for comparison).

2.4.7 Residual Dynamic Stress from External Aiding (θ_{eaid})

At this point, we will introduce an error model for the aiding source of the IMU. The results of vector processing will be provided in Chapter 4 on page 63. If the PLL is inertial-aided, the platform dynamics are tracked by the inertial measurement unit (IMU). It is unnecessary for the PLL to track high platform dynamics. As a result, the bandwidth of the PLL can be reduced such that more wideband noise can be tolerated. However, the Doppler estimate provided by the IMU is not perfect. There is a residual Doppler estimate error leaking into the PLL. Therefore, this residual Doppler estimate error must be tracked by the PLL.

This Doppler estimate error depends on the quality of the IMU used for the carrier-tracking loop aiding. This Doppler estimate error can be modeled as either a frequency step error [13] or a frequency ramp error. In this work, we modeled the estimate error as a frequency ramp. The upper bound of the 3-sigma Doppler estimate error, $\triangle \dot{f}_{aid}$, can be found in [14]. The 3-sigma of $\triangle \dot{f}_{aid}$ is 0.015 Hz/sec for a navigation grade IMU and 1.8 Hz/sec for an automotive grade IMU. The effect of this frequency ramp error is evaluated by examining the peak phase error of the tracking loop. Again, this transient peak error of both second order and third order PLLs, given a frequency ramp input, is bounded by the same form depicted in Eq.(2.23) [27, p.390] and [28, p.180]. Therefore,

$$\theta_{eaid} = 2\pi \frac{\triangle \dot{f}_{aid}}{\omega_n^2} = 2\pi \frac{\triangle \dot{f}_{aid}}{(1.885 B_n)^2} \quad radians \tag{2.26}$$

2.4.8 Phase Jitter from the Acceleration-Sensitivity of the Local Oscillator (θ_{acc})

In the case of aided tracking loops, the oscillator's acceleration-sensitivity must be considered. The frequency error, at the input of the tracking loop, induced by the acceleration-sensitivity of the oscillator is expressed as [28, p.190]

$$\triangle f_g = k_g f_{carrier} A(t) \quad Hz \tag{2.27}$$

where k_g is the oscillator's acceleration-sensitivity in parts/g (values listed in Table 2.1 on page 26); $f_{carrier}$ is the carrier frequency; and, $A(t)$ is the acceleration stress in g as a function of time. If $A(t)$ is a jerk stress, g/sec, then the units of $\triangle f_g$ are Hz/sec. As a result, $\triangle f_g$ is a frequency ramp error induced into the PLL. Similar to the analysis for the error in the external Doppler estimate, we obtain the peak phase error of the tracking loop as

$$\theta_{acc} = 2\pi \frac{\triangle f_g}{\omega_n^2} = 2\pi \frac{\triangle f_g}{(1.885 B_n)^2} \quad radians \tag{2.28}$$

Until this step, we have analyzed the phase jitter for both unaided and aided PLL. Thus, we have each term of Eq.(2.5) on page 20 for both cases. In Section 2.5, the same analysis

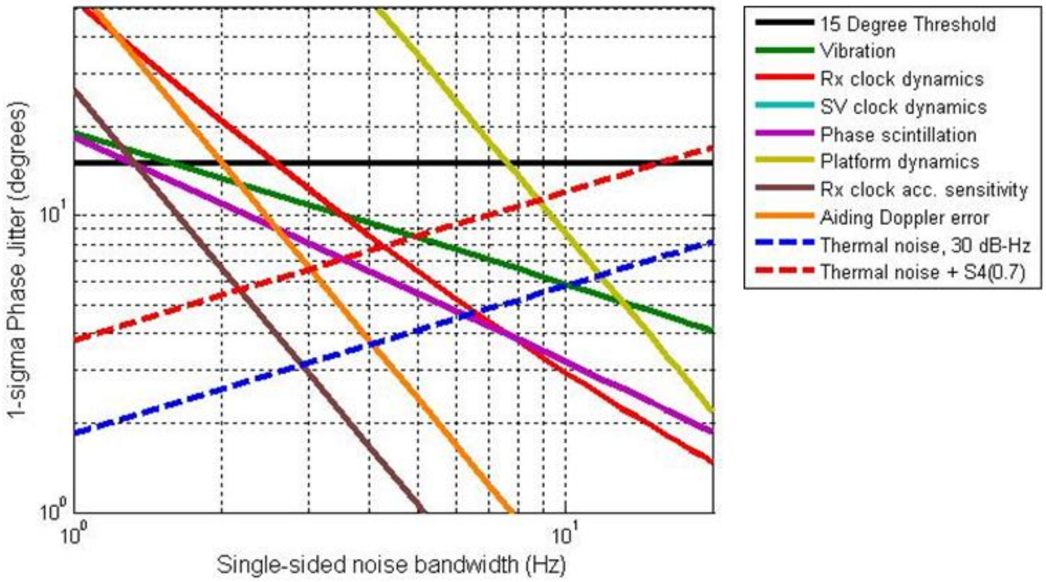

Figure 2.9: Error sources of a coherent tracking loop (PLL)

is applied to the FLL.

2.4.9 Summary of the Phase Jitter Analysis

To visualize the error sources and their dependency of the phase jitter, we draw each of the error sources versus noise bandwidth in Figure 2.9. From Figure 2.9, we see that the errors from platform dynamics, thermal noise, and amplitude scintillation dominate the total phase jitter. However, when the coherent tracking loop is Doppler aided, receiver clock dynamics and vibration effects on clock dynamics start to contribute the major parts of the total phase jitter. Phase scintillation may also dominate the phase jitter if the noise bandwidth of the coherent tracking loop is small. Note that the impacts of satellite clock dynamics are not comparable to the other error sources. This is why we would not see the curve of the error from satellite clock dynamics in Figure 2.9. The idea of designing a PLL is to find the optimized bandwidth for circumstances which have all of the possible error sources. The optimized noise bandwidth of the PLL is determined through a trade-off process. Details of selecting the best bandwidth is depicted in Section 4.3 on page 66. In the next paragraph, we will demonstrate the final phase jitter of the optimized noise bandwidths for an unaided and a Doppler aided PLL.

Figure 2.10 concludes the aforementioned phase jitter analysis. This figure consists of all

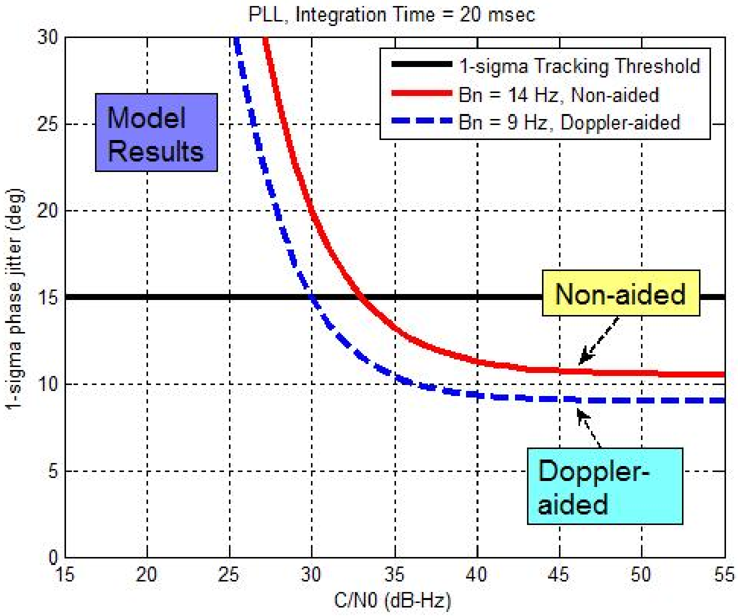

Figure 2.10: Total phase jitter, with ionospheric scintillation

of the error sources of the phase jitter. The important ideas we learn from Figure 2.10 are as follows:

1. In the presence of scintillation with $S_4 = 0.7$, the optimized bandwidth of the unaided PLL is 14 Hz. The corresponding minimum C/N_0 is 33 dB-Hz.

2. For the same scintillation condition as Item 1, if the Doppler aiding is applied, the optimized bandwidth of the aided PLL is 9 Hz. As a result, the minimum C/N_0 is 30 dB-Hz. This is a 3 dB improvement comparing to the unaided PLL.

3. From Figure 2.10, we see that the sensitivity improvement by applying the Doppler aiding technique is not significant. This is because of the counter-effects of decreasing the loop bandwidth. The phase jitter (apart from the thermal noise and the amplitude scintillation) increase when decreasing the loop bandwidth. The margin that is saved by rejecting the thermal noise has been offset by the residual dynamic stress, clock dynamics, and the phase scintillation. As will be seen in Section 2.5, the same phenomenon also exists while using an FLL. The difference is that the margin is more greatly preserved when using an FLL. In other words, Doppler aiding is more effective for the FLL than the PLL.

2.5 Performance of a GPS Receiver with a Doppler-Aided Frequency-Locked Loop

An FLL (a non-coherent tracking loop) was formerly referred to as an automatic frequency control (AFC) loop. The fundamental idea of a frequency discriminator is to measure the frequency change in the carrier signal. Various types of frequency discriminators have been investigated in [20]. Since the frequency discriminators are affected by the navigation data bits, the sign changes between successive data bits must be resolved. Among those AFC's, the cross-product AFC with decision-feedback (CPAFCDF) solves the bit-changing problem as well as resulting in the best noise performance [21]. As will be seen, the frequency estimate is achieved by performing a cross-product operation on the successive in-phase (I) and quadrature (Q) samples.

On the other hand, the sign change, used as decision feedback to the tracking loop, is evaluated by completing a dot-product operation on the successive I and Q samples. These sign changes can be used to demodulate the data differentially (differential phase shift keying (DPSK) demodulation) [27, p.381]. In the analysis here, we perform the cross-product within a navigation data bit period. So there is no need to perform the dot-product for sign determination. The integration of the 20 msec in-phase data can be decomposed into two parts, the first 10 msec for I_{k-1} and the second 10 msec for I_k. The same process is also done for the quadrature channel. The cross-product operation is done every 20 msec. After the current cross-product is done, the current 20 msec of data will be discarded. The loop will wait for the next 20 msec of data to perform the next cross-product. Thus, a cross-product AFC (CPAFC) will provide the frequency estimate at each 20 msec with the integration time of 10 msec. Figure 2.11 illustrates the block diagram of the CPAFC [20]. As demonstrated in [20], the frequency discriminator output is represented by

$$V_f(k) = I_{k-1}Q_k - Q_{k-1}I_k \tag{2.29}$$

where I_k and Q_k are the baseband in-phase and quadrature samples at the outputs of the integrate-and-dump filters. The cross-product must be performed within a data-bit period [27, p.379]. Therefore, the maximum coherent integration time for this frequency tracking loop is half of the data-bit period. For example, T_{coh} is 10 msec for the GPS tracking.

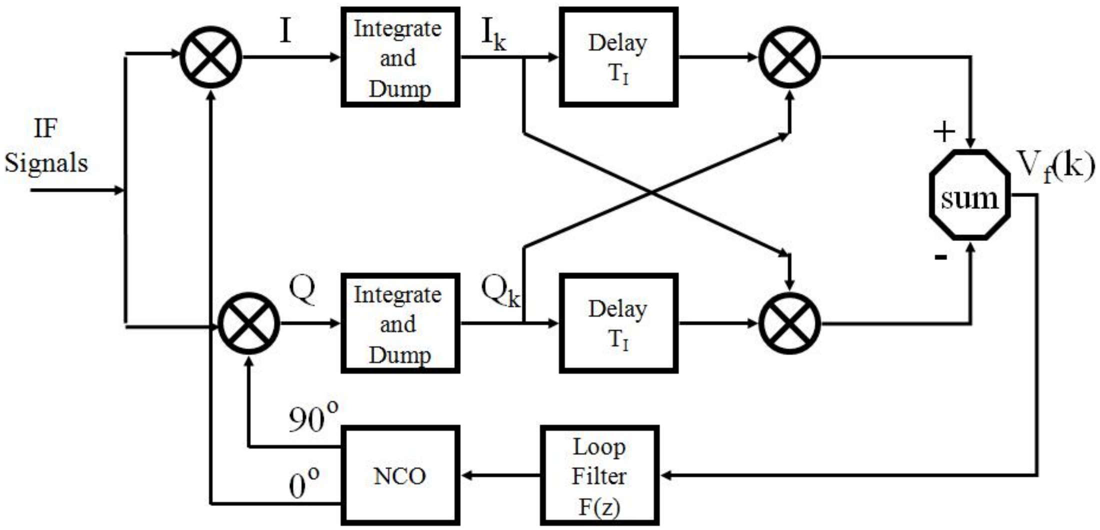

Figure 2.11: Cross Product AFC(CPAFC)

The linear mode of this type of FLL has exactly the same form as the PLL shown in Figure 2.6 on page 19, except that the input is replaced by f_i; the output is f_o; and, the frequency estimate error is defined as δf. It is important to note that the carrier NCO in an FLL does not act as an integrator. It is simply a means of converting a frequency number to sine and cosine of frequency [27, p.384]. Therefore, the order of the closed loop is the same as the order of the loop filter. Traditionally, a second order FLL is used for a receiver, which can track a constant phase acceleration. From now on, we focus on the error performance evaluation of this second order cross-product automatic frequency control loop.

Similar to the PLL, the one-sigma frequency error is defined as the frequency jitter [28], which is represented by

$$\sigma_{\delta f} = \sqrt{\sigma^2_{\delta f\omega} + \sigma^2_{\delta fsv} + \sigma^2_{\delta frx} + \sigma^2_{\delta fv} + \sigma^2_{\delta fp}} + \frac{v_e + v_{acc}}{3} \quad Hz \tag{2.30}$$

where

$\sigma_{\delta f\omega}$= the frequency jitter from thermal noise and the amplitude scintillation (if applied);

$\sigma_{\delta fsv}$= the frequency jitter from the instability of the satellite's oscillators;

$\sigma_{\delta frx}$= the frequency jitter from the instability of the receiver's oscillators;

$\sigma_{\delta fv}$= the vibration induced frequency jitter;

$\sigma_{\delta fp}$= the frequency jitter caused by the phase scintillation;

v_e= the dynamic stress in the FLL tracking loop; and,

v_{acc}= the excessive bias frequency error induced by the acceleration sensitivity of the local oscillator.

Each term of the error sources will be evaluated separately in the following sub-sections.

2.5.1 Thermal Noise and Amplitude Scintillation ($\sigma_{\delta f\omega}$)

The thermal noise tracking error of the FLL with a cross-product frequency discriminator is given by [27, p.381] in the following form:

$$\sigma_{\delta f\omega}^2 = \frac{1}{4\pi^2}\frac{4B_n}{T_{coh}^2\frac{C}{N_0}}\left[1+\frac{1}{2T_{coh}\frac{C}{N_0}}\right] \quad Hz^2 \tag{2.31}$$

Analogous to the derivations in [1, p.92] and [17], in the presence of the amplitude scintillation, the tracking error was derived and given as

$$\sigma_{\delta f\omega}^2 = \frac{1}{4\pi^2}\frac{4B_n}{T_{coh}^2\frac{C}{N_0}(1-S_4^2)}\left[1+\frac{1}{2T_{coh}\frac{C}{N_0}(1-2S_4^2)}\right] \quad Hz^2 \tag{2.32}$$

Figure 2.12 demonstrates the results of Eq.(2.32) with $B_n = 1\ Hz$ and $T_{coh} = 0.01\ sec.$ From Figure 2.12, we see that if $S_4 = 0.7$, the minimum allowable C/N_0 is degraded by 9 dB when compared to $S_4 = 0$ (from point A to point B in the figure). Similar to the phase jitter shown in Figure 2.7 on page 23, we also see degradation in sensitivity caused by the amplitude scintillation. The key work is to shift the dotted red curve in the figure to as far left as possible. However, this is just the first error source of the frequency jitter. Other error sources may push the red curve back to the right. To determine the optimal bandwidth, we need to evaluate all of the error sources.

As will be seen in the following sub-sections, the analysis of the remaining error sources is found using the following equation:

$$\sigma_{\delta fx}^2 = \int_0^\infty \left|1-H(j2\pi f)\right|^2 S_{\delta f_x}(f)df \quad Hz^2 \tag{2.33}$$

where $S_{\delta f_x}$ is the corresponding frequency noise PSD of each error source. Usually, the frequency noise PSD can be approximated by the phase noise PSD based on the following relation:

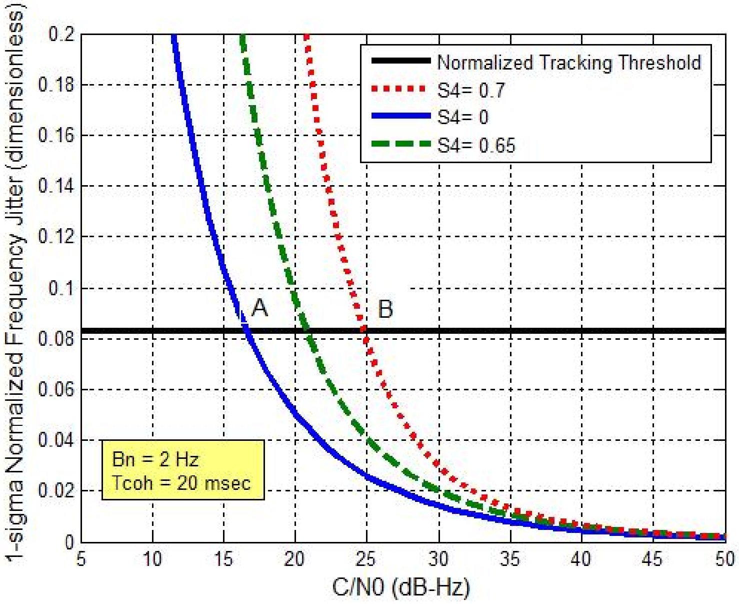

Figure 2.12: Normalized Frequency jitter caused by thermal noise and amplitude scintillation

$$S_{\delta f_x} = f^2 S_{\delta \phi_x} \tag{2.34}$$

From Eqs. (2.33) and (2.34), and given the phase noise PSDs, the error performance of the second order FLL was analyzed and provided as follows.

2.5.2 Frequency Jitter Resulting from Receiver Oscillator Phase Noise ($\sigma_{\delta f}$) and Satellite Oscillator Phase Noise ($\sigma_{\delta fsv}$)

$\sigma_{\delta frx}$ is calculated by substituting Eq.(2.14) on page 24 into Eqs. (2.33) and (2.34). Since $S_{\delta f_x}$ is 0 when $f \geq f_h$ and $f_h = \frac{1}{2T_{coh}}$, we can further simplify Eq.(2.33) as

$$\begin{aligned}\sigma^2_{\delta frx} =& N^2 \Bigg\{ X h_4 \int_0^{x_h} \frac{x^2}{1+x^4} dx + h_3 \int_0^{x_h} \frac{x^3}{1+x^4} dx + \frac{h_2}{X} \int_0^{x_h} \frac{x^4}{1+x^4} dx \\ &+ \frac{h_1}{X^2} \int_0^{x_h} \frac{x^5}{1+x^4} dx + \frac{h_0}{X^3} \int_0^{x_h} \frac{x^6}{1+x^4} dx \Bigg\} \quad Hz^2\end{aligned} \tag{2.35}$$

where $X = \frac{2\pi}{\omega_n}$, $x_h = \frac{2\pi f_h}{\omega_n}$. Note that Eq.(2.35) is valid only for the second order FLL. Unlike the results in Eq.(2.16) on page 25, Eq.(2.35) must be calculated numerically. Because

Eq.(2.16) satisfies the conditions of the following formula, Eq.(2.16) can have a closed form solution.

$$\int_0^\infty \frac{x^{m-1}}{1+x^n}dx = \frac{\pi}{nsin(\frac{m\pi}{n})} \quad for \ \ 0 < m < n \tag{2.36}$$

Except for the first term, terms in Eq.(2.35) do not have the conditions in Eq.(2.36). Therefore, it is not practical to have a closed form solution. The key difference between Eq.(2.16) and Eq.(2.35) is that the power spectral density for the frequency tracking loop is obtained by using Eq.(2.34). The numerators of Eq.(2.35) have been enlarged by a power of two. This is why Eq.(2.36) cannot be applied when solving Eq.(2.35).

Satellite Oscillator Phase Noise ($\sigma_{\delta fsv}$)

$\sigma_{\delta fsv}$ has the same form as in Eq.(2.35) except that the coefficients, h_i , are values for the Cesium clock.

2.5.3 Vibration-Induced Frequency Jitter ($\sigma_{\delta fv}$)

The frequency jitter induced by the platform vibration can be calculated by substituting Eqs. (2.20) and (2.34) into Eq.(2.33). The three equations are repeated in the following three equations, respectively.

$$S_{\delta\phi v}(f) = (k_g N f_0)^2 \frac{G_g(f)}{f^2} \tag{2.37}$$

$$S_{\delta f_x} = f^2 S_{\delta\phi_x} \tag{2.38}$$

$$\sigma^2_{\delta fx} = \int_0^\infty |1 - H(j2\pi f)|^2 S_{\delta f_x}(f)df \quad Hz^2 \tag{2.39}$$

The vibration-induced frequency jitter can then be written as

$$\sigma^2_{\delta fx} = (k_g N f_0)^2 \int_0^\infty \frac{f^{2k}}{f_n^{2k} + f^{2k}} G_g(f)\,df \quad Hz^2 \tag{2.40}$$

where

k_g is the oscillator's acceleration-sensitivity in parts/g (values listed in Table 2.1 on page 26);

f_0 is the center frequency of the oscillator (values given in Table 2.1 on page 26);

N is as defined in Eq.(2.13) on page 24;

k is the order of the closed-loop; and,

$G_g(f)$ is the one-sided vibration spectral density in $^{g^2}/_{Hz}$.

The most up-to-date vibration spectral density curve for an instrument panel installation on a turbojet aircraft is shown in Figure 2.8 on page 28. Given the profile of $G_g(f)$, Eq.(2.40) must be calculated using a numerical method.

2.5.4 Frequency Jitter Resulting from Phase Scintillation ($\sigma_{\delta fp}$)

The frequency jitter induced by the ionospheric phase scintillation can be evaluated by substituting Eq.(2.1) on page 14 and Eq.(2.38) into Eq.(2.39). Eq.(2.41) shows the final result of the substitutions. If $3 < p < 2k + 2$, there is an approximated closed-form solution given in [1, p.149]. As discussed in Subsection 2.4.5 on page 29, $p = 2.5$ is considered in this work. Therefore, we numerically integrate Eq.(2.41) to evaluate the frequency jitter resulting from phase scintillation.

$$\sigma^2_{\delta fx} = \int_0^\infty \frac{f^{2k+2}}{f_n^{2k} + f^{2k}} \frac{T_{sct}}{(f_0^2 + f^2)^{p/2}} df \quad Hz^2 \tag{2.41}$$

$$\approxeq T_{sct} \int_0^\infty \frac{f^{2k+2-p}}{f_n^{2k} + f^{2k}} df \quad for \quad p < 2k+2 \tag{2.42}$$

where

T_{sct} is the magnitude of the phase scintillation PSD at the frequency of 1 Hz;

k is the order of the closed-loop;

f_n is the natural frequency of the closed loop in Hz; and,

p is the slope of the phase scintillation PSD (usually in the range of 1 to 4 and typically 2.5).

2.5.5 Dynamic Stress in the FLL (v_e)

Given the same order of the closed loop, the FLL can track one order higher dynamic than the PLL [28]. Therefore, the peak frequency error of the second-order FLL due to a range (phase) jerk input can be bounded by the following form [28, p.192]:

$$v_e = \frac{\overset{\bullet\bullet}{\triangle f}}{\omega_n^2} = \frac{2.7599 j_{max}}{\lambda_{carrier} B_n^2} \quad Hz \tag{2.43}$$

where j_{max} is the maximum line-of-sight phase jerk in g/sec.

2.5.6 Residual Dynamic Stress from External Aiding (v_{eaid})

We model the residual error of the external Doppler estimate as a frequency ramp. Therefore, of interest is the peak frequency error caused by a frequency ramp input in the second-order FLL. For the FLL, the steady state error is given by the first derivative of the phase error in the second-order PLL. The response of the frequency step input to the second-order PLL is [28, p.192]

$$\theta = 0.45 \frac{\triangle f_{aid}}{\omega_n} \quad cycles \tag{2.44}$$

where $\triangle f_{aid}$ is the frequency step input. Performing one derivative on Eq.(2.44), we obtain the response of the second-order FLL due to the frequency ramp input. Thus,

$$v_{eaid} = 0.45 \frac{\triangle \dot{f}_{aid}}{1.885 B_n} \quad Hz \tag{2.45}$$

2.5.7 The Frequency Jitter from the Acceleration-Sensitivity of the Local Oscillator (v_{acc})

The frequency error at the input of the tracking loop induced by the acceleration-sensitivity of the oscillator is exemplified in Eq.(2.27). If the induced frequency error is a frequency ramp, the final frequency jitter has the same form in Eq.(2.45). Therefore,

$$v_{acc} = 0.45 \frac{\triangle f_g}{1.885 B_n} \quad Hz \tag{2.46}$$

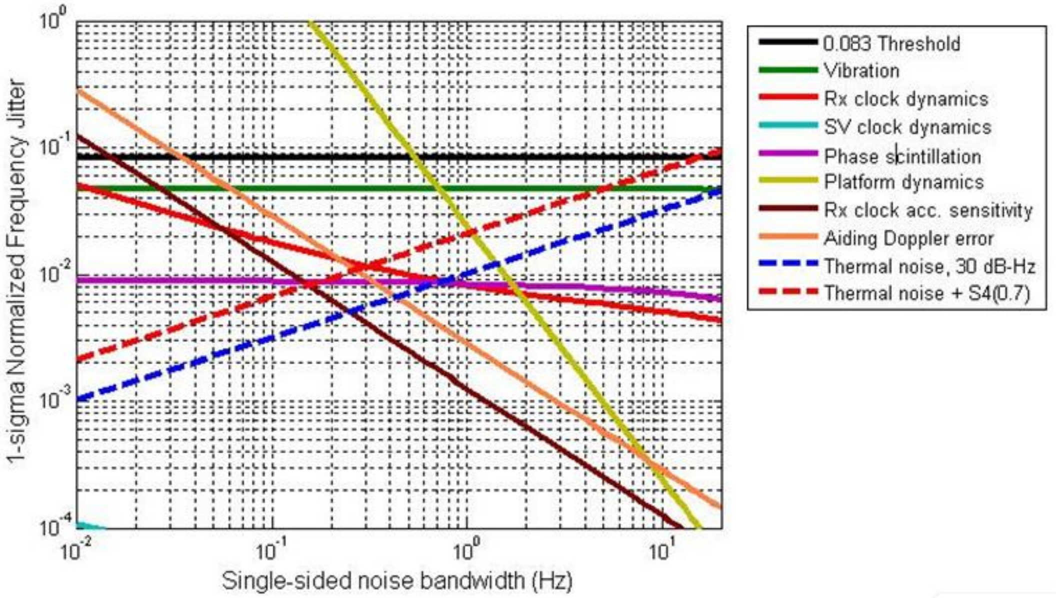

Figure 2.13: Error sources of a non-coherent tracking loop (FLL)

where $\triangle f_g$ is the frequency ramp induced by the acceleration-sensitivity of the local oscillator in the presence of constant range (phase) jerk dynamics.

2.5.8 Summary of the Frequency Jitter Analysis

We summarize the error sources of the frequency jitter in Figure 2.13. From this figure, we can evaluate the relative strength of each error sources contributed to the total frequency jitter. For an unaided FLL, the dominant error sources are thermal noise, platform dynamics, vibration impacts on receiver clock, and amplitude scintillation. If the FLL is Doppler aided, the clock dynamics start to dominate the frequency jitter. The key of a tracking loop design is to determine an optimized noise bandwidth such that the frequency jitter is minimized. Figure 2.13 provides the information for optimizing the noise bandwidth of a non-coherent tracking loop (FLL). Details of selecting the best bandwidth is depicted in Section 4.3 on page 66. In the next paragraph, we illustrate the trade-off results and discuss the benefits of applying the technique of Doppler aiding.

Similar to Section 2.4.9 on page 32, we include the total frequency jitter in Figure 2.14. This figure consists of all of the error sources of the frequency jitter. The summary of the findings from Figure 2.14 is as follow.

1. In the presence of scintillation with $S_4 = 0.7$, the optimized bandwidth of the unaided

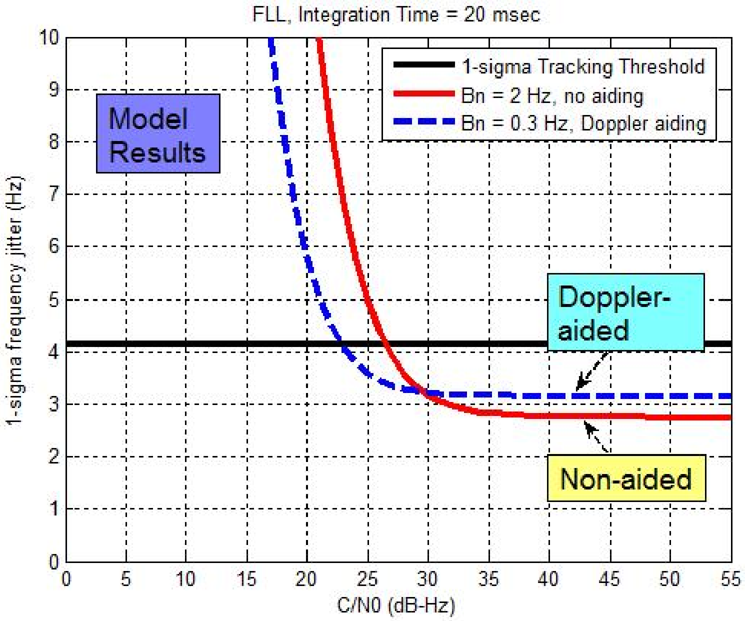

Figure 2.14: Total frequency jitter, with ionospheric scintillation

FLL is 2 Hz. The corresponding minimum C/N_0 is 27 dB-Hz.

2. For the same scintillation condition as Item 1, if the Doppler aiding is applied, the optimized bandwidth of the aided FLL is 0.3 Hz. As a result, the minimum C/N_0 is 23 dB-Hz. This is a 4 dB improvement compared to the unaided FLL.

3. Remember that the minimum C/N_0 of the aided PLL is 30 dB-Hz (shown in Figure 2.10 on page 33). The minimum allowable C/N_0 for the aided FLL is 7 dB lower than the aided PLL.

2.6 Word Error Rate (WER) Analysis

The purpose of this section is to derive the needed equations for evaluating WER. The WER for both PLL and FLL, with or without scintillation, will be discussed. The new aspects, as compared to the literature, in this section are:

1. Introduce the biased Probability Density Function (PDF) of a PLL to evaluate the bit error rate (BER). Currently, the BER of a PLL is calculated using the Tikhonov density function, which assumes no dynamic stress on the PLL. Traditionally, one would inflate the Tikhonov density function to cover the extra error due to dynamics.

However, as will be seen in this section, the estimated BER by this arrangement is somewhat conservative (i.e., the estimated BER is larger than the true BER).

2. The traditional way of evaluating the BER of an FLL also assumes zero mean of the frequency-estimate error. This leads to the calculated BER of an FLL only depending on the pre-detection integration time and the C/N_0. We introduce a way of evaluating the BER while the FLL is dynamically stressed.
3. The BER and WER for both PLL and FLL with scintillation are appraised.

As will be seen from the results of this section, satisfying the WER ($< 10^{-4}$) imposes more stringent requirements on the tracking error as well as the signal strength than the requirements for keeping phase or frequency locked. The Doppler aiding technique does not significantly facilitate the problem of WER degradation under weak signal conditions.

2.6.1 Biased Probability Density Function (PDF) of a PLL

To evaluate the average bit error rate (BER) conditioned on the phase-estimate error, it is required to solve the PDF of the phase-estimate error in a PLL. The steady state PDF of the first-order PLL has been found by solving its corresponding Fokker-Planck equation [38, p.89]. The PDF of the first-order PLL is also referred to as the Tikhonov density function. However, the Tikhonov density function was obtained by assuming that no dynamic stress was imposed on the first-order PLL. We are interested in finding the PDF when the tracking loop is dynamically stressed. Using the stressed PDF more accurately predicts the BER for this aviation application of a GPS receiver.

The steady state PDF of the standard first-order PLL is given as [38, p.89]

$$\begin{aligned} p_\phi(\phi) = Cexp(\alpha cos(\phi) + \beta\phi)\Big[1+ \\ D\int_{-\pi}^{\phi} exp(-\alpha cos(x) - \beta x)dx\Big] \quad -\pi \le \phi \le \pi \end{aligned} \tag{2.47}$$

with the boundary condition

$$p_\phi(\pi) = p_\phi(-\pi) \tag{2.48}$$

and the normalizing condition

$$\int_{-\pi}^{\pi} p_{\phi}(\phi)d\phi = 1 \tag{2.49}$$

ϕ is the phase-estimate error, which is $\delta\varphi$ in the previous sections. C and D are constants which can be resolved by the boundary and normalizing conditions. α and β are related to the variance and the dynamic stress of the phase jitter by the following forms: $\alpha = \frac{1}{\sigma_{\phi}^2}$ and $\beta = \frac{\theta_e}{\sigma_{\phi}^2}$, where σ_{ϕ}^2 is the variance of the noise component in the phase jitter in Eq.(2.5) on page 20, and θ_e is the constant dynamic stress in the bias component of the phase jitter. If there is no dynamic stress, $\beta = 0$, Eq.(2.47) becomes the well known Tikhonov density function [38, p.90] written as

$$p_{\phi}(\phi) = \frac{exp(\alpha cos(\phi))}{2\pi I_0(\alpha)} \quad -\pi \leq \phi \leq \pi \tag{2.50}$$

where $I_0(\bullet)$ is the zero-order modified Bessel function. For the Costas PLL, the phase-estimate error, ϕ and θ, must double to account for the dot-product of the in-phase and quadrature channels. Accordingly, the PDF of the first-order Costas PLL is given as [39, p.274]

$$p_{\phi}(\phi) = \frac{exp(\alpha_c cos(2\phi))}{\pi I_0(\alpha_c)} \quad -\frac{\pi}{2} \leq \phi \leq \frac{\pi}{2} \tag{2.51}$$

where $\alpha_c = \frac{1}{4\sigma_{\phi}^2}$.

If there is a dynamic stress for the Costas loop, $\beta = \beta_c = \frac{\theta_e}{2\sigma_{\phi}^2}$. Similar to Eq.(2.47), we can find the expression for the stressed PDF of the Costas loop as

$$\begin{aligned} p_{\phi}(\phi) = C_c exp(\alpha_c cos(2\phi) + 2\beta_c\phi)\Big[1+ \\ D_c \int_{-\pi/2}^{\phi} exp(-\alpha_c cos(2x) - 2\beta_c x)dx\Big] \quad -\frac{\pi}{2} \leq \phi \leq \frac{\pi}{2} \end{aligned} \tag{2.52}$$

From the boundary condition, $p_{\phi}(\frac{\pi}{2}) = p_{\phi}(-\frac{\pi}{2})$, the constant D_c can be found as

$$D_c = \frac{exp(-2\beta_c\pi) - 1}{\int_{-\pi/2}^{\pi/2} exp(-\alpha_c cos(2x) - 2\beta_c x)dx} \tag{2.53}$$

Given D_c and the normalizing condition, $\int_{-\pi/2}^{\pi/2} p_\phi(\phi)d\phi = 1$, the constant C_c can be found as

$$C_c = \frac{1}{\int_{-\pi/2}^{\pi/2} E(\phi)[1 + D_c F(\phi)]d\phi} \tag{2.54}$$

where

$$E(\phi) = exp(\alpha_c cos(2\phi) + 2\beta_c \phi)$$

and,

$$F(\phi) = \int\limits_{-\pi/2}^{\phi} exp(-\alpha_c cos(2x) - 2\beta_c x)dx$$

A numerical computation is required to evaluate Eq.(2.52). In the case of the Costas PLL, it is important to note that for $\frac{\beta_c}{\alpha_c} = \theta_e > sin(\frac{\pi}{4})$, the steady-state solution does not hold. Furthermore, for $\alpha_c > 1$, the PDF yields more reasonable accuracy [38, p.93]. One can note that if $\theta_e = 0$, i.e., no dynamic stress, Eq.(2.52) becomes Eq.(2.51). Also note that the closed-form of a stressed PDF given in [39, p.118] is incorrect. One can confirm this simply by performing the normalizing condition test. Figure 2.15 illustrates the main idea of this section. Both curves represent the PDF with the same amount of phase jitter. The blue curve indicates the non-stressed PDF, whereas the red curve represents the stressed PDF. Obviously, from Figure 2.15, the BER is different for each case. It would be too optimistic if one were to ignore the bias phase error due to the dynamics. On the other hand, it is too pessimistic to treat the bias term as part of the total noise component. In the latter case, one would obtain the exact same BER because the BER is evaluated at the same value of the total phase jitter no matter that the tracking loop is dynamically stressed or not. Accordingly, it would be misleading to state that applying inertial aiding to the carrier-tracking loop would not improve the BER at all since the blue curve always holds.

Thus far, we can calculate the BER conditioned on the phase-estimate error for the PLL tracking loop. In contrast, for the FLL tracking loop, we will use the traditional DPSK upper bound for BER, which assumes zero frequency-estimate error. In Sections 2.6.2 and 2.6.3, details about the BER and WER will be discussed.

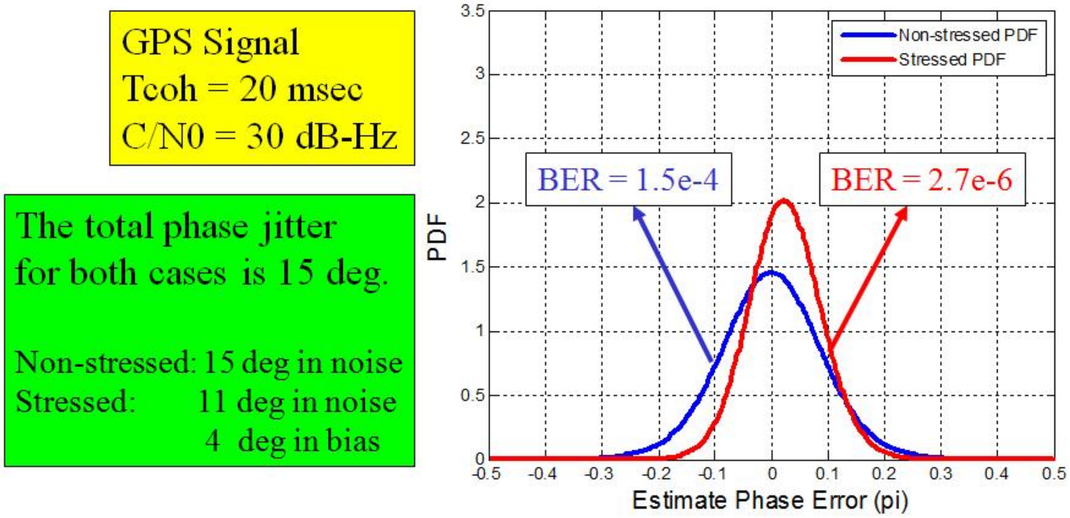

Figure 2.15: The PDF of a dynamically-stressed PLL

2.6.2 Bit Error Rate (BER)

In this section, we evaluate BER and WER for GPS data with both PLL and FLL tracking loops. Analyses of BER and WER for WAAS are beyond the scope of this dissertation and some preliminary discussions are provided in Appendix A.

The evaluation of the BER for GPS will be divided into two aspects. The first is the BPSK demodulation BER for the PLL tracking; the second is the DPSK demodulation for the FLL tracking.

BER in the Case of PLL Tracking Without Scintillation

As in Subsection 2.6.1 on page 43, define ϕ as the phase estimate error. The BER for the GPS messages utilizing PLL tracking is represented by the expression for BPSK [39] as

$$P_{b,GPS,PLL}(\phi) = \frac{1}{2} erfc\left(\sqrt{T_{GPS,PLL}\frac{C}{N_0}} cos(\phi)\right) \tag{2.55}$$

where $T_{GPS,PLL}$ is the coherent integration time which must be the bit period of the GPS data bits, which is 0.02 sec and the complementary error function, $erfc(\bullet)$, is defined as

$$erfc(x) = \frac{2}{\sqrt{\pi}} \int_{x}^{\infty} e^{-y^2} dy \tag{2.56}$$

Therefore, the average bit error probability (BER) for GPS is given by averaging $P_b(\phi)$ over the phase-error distribution illustrated in Eq.(2.51) on page 44 and Eq.(2.52) on page 44 for no dynamic stress and with dynamic stress, respectively.

$$BER_{PLL} = \int_{-\pi/2}^{\pi/2} P_b(\phi)p_{\phi}(\phi)d\phi \tag{2.57}$$

BER in the Case of PLL Tracking With Scintillation

In the presence of scintillation, the signal amplitude has the Nakagami-m distribution as in Eq.(2.3) on page 16. The BER in this case is [1, p.204]

$$BER_{PLL,scint} = \int_{0}^{\infty}\int_{-\pi/2}^{\pi/2} P_b(\phi, A)p_{\phi}(\phi)f_A(A)d\phi dA \tag{2.58}$$

Further simplification of Eq.(2.58) can be found in [1, p.204]. The final BER with PLL tracking in the presence of scintillation is then

$$BER_{PLL,scint} = \int_{0}^{\infty}\int_{-\pi/2}^{\pi/2} P_b(\phi, \rho_0)p_{\phi}(\phi)f_{\rho_0}(\rho_0)d\phi d\rho_0 \tag{2.59}$$

where

$f_{\rho_0}(\rho_0) = \frac{m^m \rho_0^{m-1}}{\Gamma(m)\left(\frac{C}{N_0}\right)^m}\exp\left(-\frac{m\rho_0}{\frac{C}{N_0}}\right)$ and ρ_0 represents the instantaneous carrier-to-noise density ratio of the received signal;

$P_{\phi}(\phi)$ is the PDF defined in Eq.(2.51) and Eq.(2.52) on page 44; and,

For GPS ($T_{GPS,PLL} = 0.02\ sec$): $P_b(\phi, \rho_0) = \frac{1}{2}erfc\left(\sqrt{T_{GPS,PLL}\rho_0}cos(\phi)\right)$.

BER for FLL Tracking Without Scintillation

The navigation data bit demodulation is achieved by sensing the successive sign changes by applying the dot-product operation on the in-phase channel [27, p.381]. Therefore, it is a DPSK demodulation. The maximum coherent integration time of the FLL is limited to being half of the symbol period. As defined, δf is the frequency-estimate error of the FLL. Thus, the phase error after a period of the coherent integration time of the FLL is $2\pi\delta f T_{FLL}$ in radians. With this amount of phase error, the conditional probability of bit error is evaluated as [41] and [42, Eq. (5.4-54)]

$$\begin{aligned} P_{b,FLL}(\delta f) &= Q_1(a,b) - \frac{1}{2}e^{-(a^2+b^2)/2}I_0(ab) \\ a &= \sqrt{T_{FLL}\frac{C}{N_0}(1-cos(2\pi\delta f T_{FLL}))} \\ b &= \sqrt{T_{FLL}\frac{C}{N_0}(1+cos(2\pi\delta f T_{FLL}))} \end{aligned} \tag{2.60}$$

where $Q_1(\bullet)$ is the well-known first-order Marcum's Q function; $I_0(\bullet)$ is the zero-order modified Bessel function; and, $T_{FLL} = 0.01\ sec$ for GPS signal.

If we assume zero frequency-estimate error, $\delta f = 0$, Eq.(2.60) reduces to the traditional probability of bit error of a DPSK signal as [27, p.381]

$$P_{b,FLL} = \frac{1}{2}e^{-T_{FLL}\frac{C}{N_0}} \tag{2.61}$$

In short, the BER of a GPS message with FLL tracking is predicted by Eq.(2.61).

BER in the Case of FLL Tracking With Scintillation

In the presence of scintillation, the signal amplitude again has the Nakagami-m distribution depicted in Eq.(2.3) on page 16. However, the BER for the FLL tracking is not averaged over the distribution of the frequency-estimate error. Thus, Eq.(2.61) will be applied to determine the BER in this case. Therefore, the BER is

$$BER_{FLL,scint} = \int_0^\infty P_{b,FLL}(\rho_0)f_{\rho_0}(\rho_0)d\rho_0 \tag{2.62}$$

where

$f_{\rho_0}(\rho_0) = \frac{m^m\rho_0^{m-1}}{\Gamma(m)\left(\frac{C}{N_0}\right)^m}exp\left(-\frac{m\rho_0}{\frac{C}{N_0}}\right)$ and ρ_0 represents the instantaneous carrier-to-noise density ratio of the received signal; and,

For GPS ($T_{FLL} = 0.01\ sec$): $P_{b,FLL}(\rho_0) = \frac{1}{2}e^{-T_{FLL}\rho_0}$.

Finally, we have completed the evaluation for the BER for GPS using either PLL or FLL tracking in the environment with or without ionospheric scintillation. This BER evaluation also depends on the full analysis of linear model. Without the inclusive linear model analysis of the tracking errors (with and without ionospheric scintillation), we can not determine the BER for the stand alone PLL or FLL; Doppler-aided PLL or FLL under conditions with and without ionospheric scintillation.

2.6.3 WER for GPS

The word error rate for GPS data is approximated as

$$WER = 1 - (1 - BER)^M \tag{2.63}$$

where $M = 30$ for a GPS word. The assumption for Eq.(2.63) is that the probability of bit error in successive bits is independent. Without scintillation, this assumption is reasonable. However, in the presence of scintillation, the independence holds only for a rapid scintillation [1, p.209]. For example, if the fading lasts for 0.6 sec, the signal amplitude for the GPS follows the Nakagami-m distribution. In this case, the WER predicted by Eq.(2.63) would be too conservative. In this research, an enormously deep fading scenario was considered with fading period being much less than 0.6 sec. Hence, Eq.(2.63) was used to approximate the WER. The details for the case of slow scintillation can be found in [1, p.209].

2.6.4 Results of WER Analysis

To summarize the WER analysis, we demonstrate the WER for PLL in Figure 2.16 on the following page. We use the WER of the PLL as an example. The WER of the FLL has a similar trend of the case to be shown here. From the following findings, we see that the improvement of WER by applying the technique of Doppler aiding is not substantial. What follows are the important results learned from Figure 2.16.

1. The sensitivity for achieving WER $< 10^{-4}$ is degraded by 4 dB due to the impact of ionospheric scintillation (compare the blue and red solid curves).

2. The red curves, i.e., those with scintillation affects, do not have the same smooth and monotonic behavior as the blue curves. This is due to the characteristic of the Nakagami-m distribution. In the presence of scintillation, the minimum C/N_0 for maintaining the WER is 32 dB-Hz (see the red solid curve). Once the signal strength is below 32 dB-Hz, the WER increases dramatically.

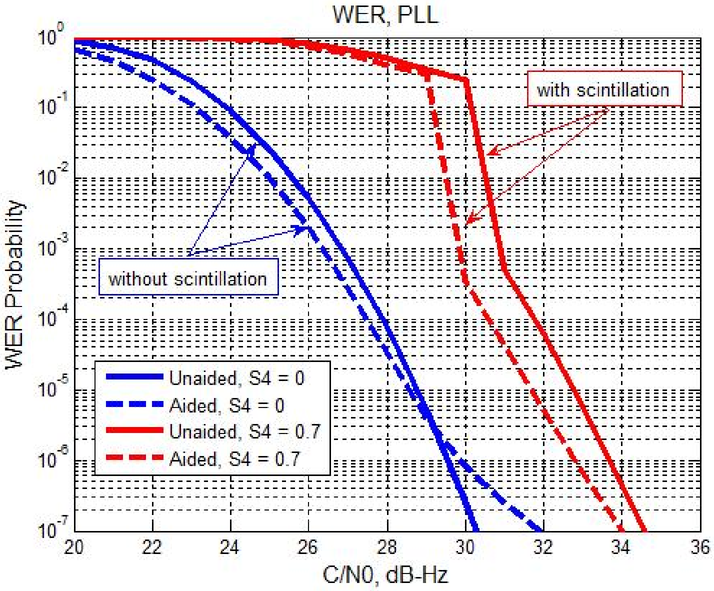

Figure 2.16: WER for PLL

3. The technique of Doppler aiding does not improve the WER significantly. From the figure (compare the red solid and the red dashed curves), we see only 1 dB improvement when S_4 is 0.7.

2.7 Summary

Thus far, we have completed the linear model analysis for both the PLL (a coherent tracking loop) and the FLL (a non-coherent tracking loop). The minimum allowable C/N_0 is obtained by examining the point at which the tracking threshold is exceeded. The rule-of-thumb threshold for a PLL is 15^o and for an FLL $\frac{1}{12T_{coh}}$ [28] . The results of these model analyses will be presented in Chapter 4 on page 63 together with the experimental results. Generally, based on the criteria of the linear tracking thresholds, the minimum allowable C/N_0 for GPS using an inertial-aided FLL is 7 dB lower than that using an inertial-aided PLL. This result suggests that using an inertial-aided FLL is effective in coping with a fast and deep scintillation channel.

From this study, it is also shown that clock dynamics start to dominate the performance of the carrier tracking loop when Doppler aiding is applied. The trade-off is to determine the lowest allowable carrier loop bandwidth for tracking the clock dynamics and the residual error from Doppler aiding. Once this optimized bandwidth is determined, one then estimates the lowest allowable C/N_0 that the carrier tracking can tolerate. The larger the gain in C/N_0 by applying Doppler aiding, the more robust the receiver will be to ionospheric scintillation.

In Chapter 4, a contour describing the relationship of C/N_0 versus bandwidth will be introduced. Using this contour makes it easy to find the optimized loop noise bandwidth and the allowable C/N_0 at the same time. Before demonstrating the final theoretical and experimental results, a hardware simulation is presented in the next chapter.

Chapter 3

Enabling a Hardware Simulation that Includes Scintillation, Aircraft Dynamics, and Vibration

3.1 Chapter overview

To enable a hardware simulation that includes scintillation, aircraft dynamics, and vibration, we construct a hardware experiment platform which is composed of the Spirent 7700 GPS constellation simulator and a clock emulator driven by the Agilent E4424B RF signal generator (both courtesy of SiRF, Inc.). The Spirent simulator is utilized to generate scintillation and aircraft dynamics whereas the clock emulator is employed to create vibration-affected clock signals. Figure 3.1 depicts the architecture of the whole experimental setup. The purpose of this chapter is to present the steps for conducting the experiments illustrated in Figure 3.1. An overview of this chapter is as follows.

1. The scenario with a landing aircraft is created in the Spirent GPS simulator. The Spirent GPS simulator provides the capability for generating the GPS measurements from a flying vehicle with a specified rate of descent and deceleration. The location of the airport and the corresponding constellation for the specified time can also be determined in the Spirent GPS simulator. Finally the signal power of the generated GPS signals can be specified according to the GPS ICD as well as the desired receiver antenna pattern. The desired antenna pattern for aviation is regulated by the

RTCA/DO-229 [25]. We produce the signal with a power of -130 dBm at the zenith and degrade the signal power according to the antenna pattern for different elevation angles. In consequence, a realistic scenario with healthy GPS signals is created.

2. The clock emulator makes the vibration-affected RF clock signals. The vibration is based on the aircraft vibration PSD shown in Figure 2.8 on page 28. The clock emulator generates the desired RF wave form by taking the specified points of the desired phase noise density in the frequency domain. These RF clock signals are then used to drive the front-end of the NordNav GPS receiver kits. The front-end then creates the RF carrier, using the vibration-affected clock signals, for down-converting the GPS RF signals to an intermediate frequency (IF) carrier, and passes the signal through the analog to digital converter (ADC) for the data sampling in the next step. In doing so, the sampled GPS IF data have included the vibration effects on the received signals.

3. To construct the scintillation in the received GPS signals, we "add" the amplitude and phase scintillations onto the healthy GPS signals originally created in the Spirent simulator in Step 1. The process of adding the profile of the scintillation onto the healthy signals is done by using the external commands provided by the Spirent simulator. The simulator reads the script which specifies the amount of power fading and phase rotation at each 0.01 second. As a result, the external commands control the simulator and pollute (based on the desired scintillation) the healthy signals at a rate of 100 Hz. The desired amplitude and phase scintillations are extracted from the real scintillated GPS data, which were collected by the Air Force Research Lab (AFRL) on Ascension Island in 2001.

Given the above steps, this chapter demonstrates the processes of building the channel model for aircraft landing using a GPS under strong scintillation conditions. By building the channel model, a realistic GPS radio frequency (RF) signal for the considered conditions is obtained. The channel model includes strong ionospheric scintillation, vibration effects on the receiver clock, and aircraft platform dynamics.

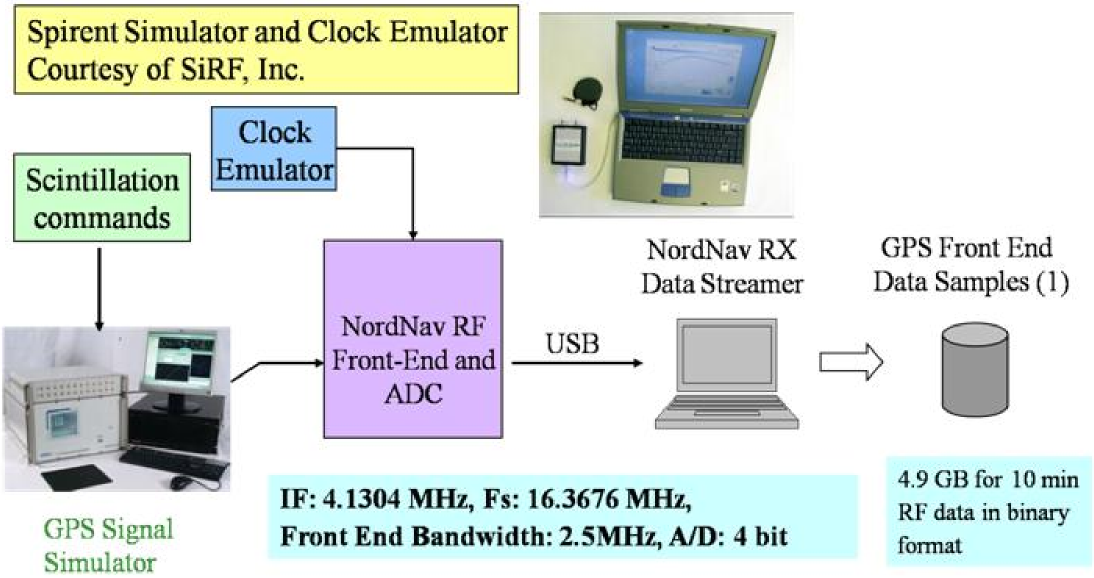

Figure 3.1: The Experimental Setup

3.2 Model of Aircraft Dynamics

The first challenge is the dynamic stress due to the maneuvers of the aircraft. The actual flight path of an aircraft is not as smooth as the straight path portrayed in Figure 3.2. There are disturbances, wind gusts, and pilot maneuvers. In the document of Minimum Operational Performance Standards for Sensors Using GPS/WAAS, i.e., RTCA/DO-229 [25], it requires a GPS receiver to continuously operate when the platform is subject to an acceleration of $0.58\ g$ or a jerk of $0.25\ {}^{\mathrm{g}}/_{\mathrm{sec}}$, where g is gravity, $9.8\ {}^{\mathrm{m}}/_{\mathrm{sec}^2}$.

Figure 3.2 illustrates the position error due to acceleration and jerk, respectively. If the GPS receiver does not track the platform dynamics, the position error increases rapidly. Therefore, to overcome the dynamic stress, the GPS receiver demands a higher bandwidth.

We have included these platform dynamics in the linear model analysis for determining the optimal bandwidth. Since we are applying Doppler-aiding to the carrier tracking loop of the GPS receiver, the platform dynamics are removed by the Doppler-aiding. Therefore, we only construct the nominal aircraft landing dynamics in the Spirent simulator. This setup is reasonable because once the bandwidth of the un-aided GPS receiver is large enough, the tracking error due to platform dynamics is tiny. When the Doppler-aiding is applied, the platform dynamics are tracked by the inertial system. Hence, the dominant error in a low bandwidth is the clock dynamics, which will be considered in the next section.

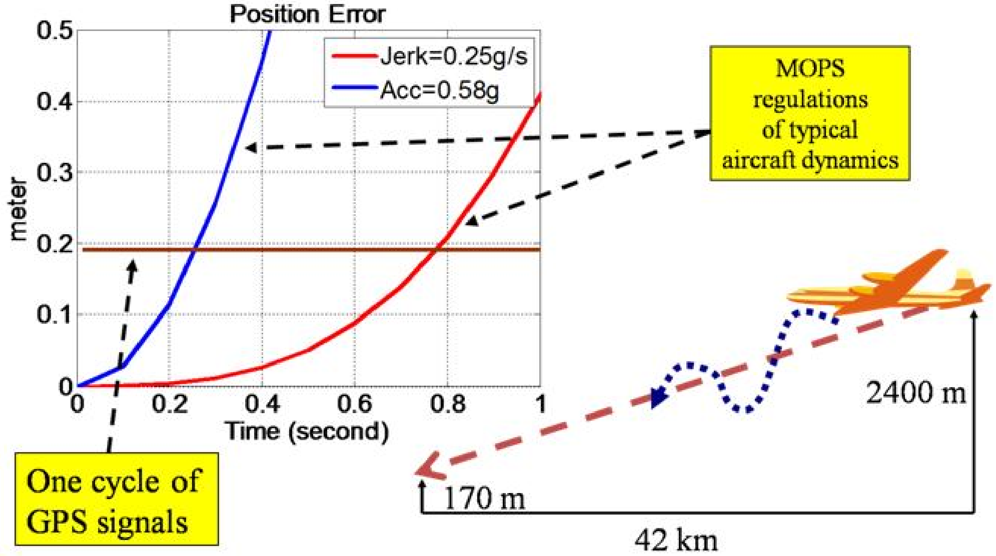

Figure 3.2: Aircraft Platform Dynamics

3.3 Construction of Aircraft Vibration-Affected Receiver Clock Signals

A GPS receiver must generate a replica GPS signal to track the received GPS signal. The quality of the replica signal depends on the stability of the local oscillator. A low-cost GPS receiver typically uses a crystal oscillator for the timing function. The stability of an oscillator can be characterized by the phase-noise power spectrum density (PSD). Figure 3.3 depicts the generic phase-noise PSD of a typical temperature-compensated crystal oscillator (TCXO) [32]. The details of deriving the model of the clock phase noise are provided in [61, pp. 336-397]. Note that the phase offset in the replica signal due to the phase noise of the oscillator must be tracked by the carrier tracking loop.

However, the oscillator is sensitive to vibration. The phase noise is boosted by the aircraft's platform vibration. The PSD of this vibration is given in Figure 2.8 on page 28. Provided the acceleration-sensitivity of the TCXO clock (Table 2.1 on page 26) and the aircraft vibration PSD (Figure 2.8 on page 28), we derived the vibration-affected phase noise PSD. Figure 3.4 describes the vibration-affected phase-noise PSD. For the considered TCXO under the aircraft vibration condition represented in Figure 3.4, the maximum increase in the phase-noise PSD floor is 9 dB. The analysis of this vibration impact on the stability

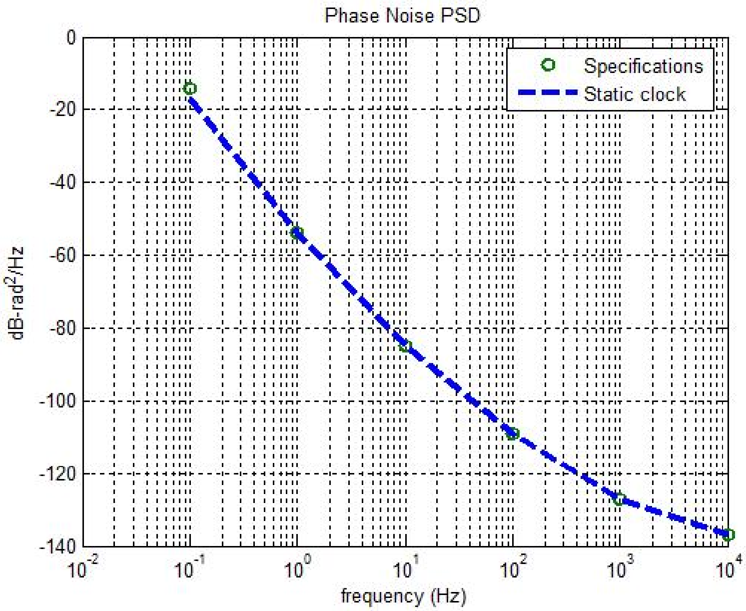

Figure 3.3: The Generic Phase Noise of a TCXO

of an oscillator can be found in [61, pp. 336-397]. This additional phase noise due to the platform vibration also demands a higher bandwidth for the GPS receiver.

The measured position error due to the overall clock dynamics (Figure 3.4) is plotted as a function of time in Figure 3.5. From Figure 3.5, we learn that the clock error exceeds one wave length of the GPS L1 carrier within 1 second.

To obtain the vibration effects on the oscillator, we utilize a clock emulator (courtesy of SiRF, Inc.) to generate the vibration-affected clock signals. The NordNav front-end used to collect GPS RF data from the Spirent simulator can be driven by an external clock (shown in Figure 3.1 on page 54). We use the clock emulator as the external clock. The clock emulator itself is a high-quality clock with low phase noise (Agilent E4424B). It can generate an arbitrary waveform to emulate the defects of an inexpensive crystal oscillator in the following three ways:

1. Specify points of the desired phase noise density in the frequency domain;
2. Specify points of the desired discrete spurious signals in the frequency domain; and,
3. Emulate thermal perturbations as a function of time.

We use Method 1 to generate the clock signals with desired phase noise PSDs (the blue dashed and red dotted curves) in Figure 3.4 on the next page. The GPS data were then collected

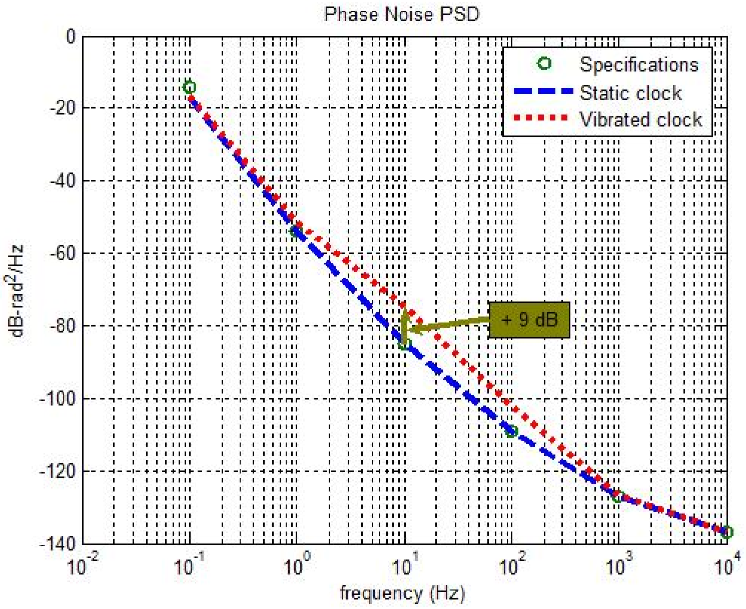

Figure 3.4: The Vibration-Affected Phase Noise of a TCXO

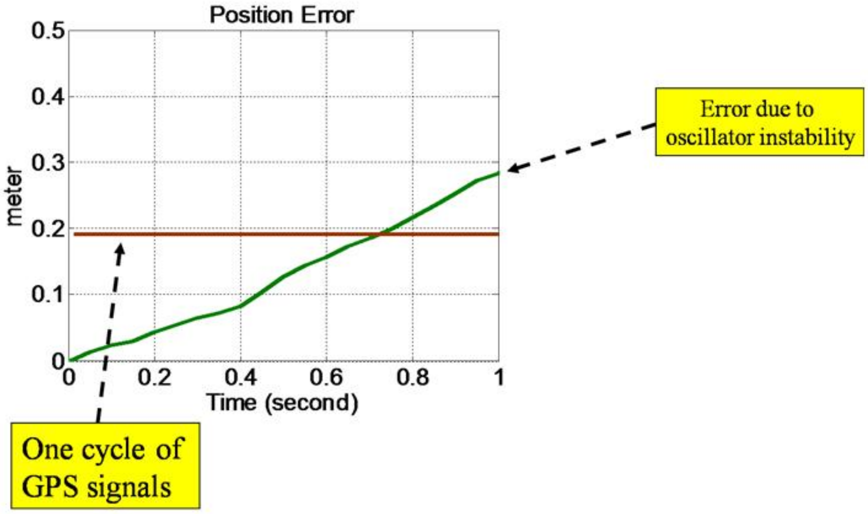

Figure 3.5: The Measured Position Error Due to the Clock Dynamics of a Typical TCXO for a GPS Receiver in an Aircraft Vibration Environment

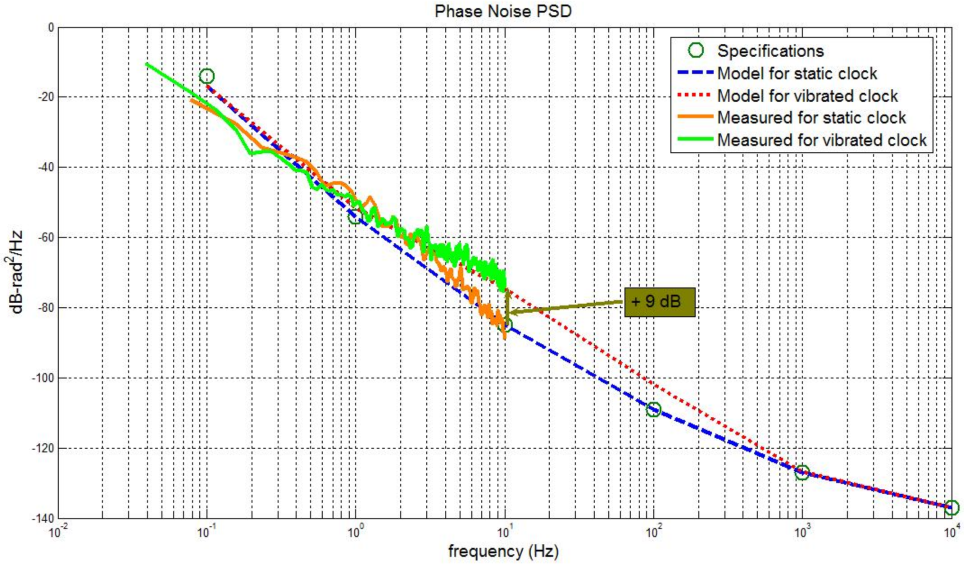

Figure 3.6: The emulated TCXO clock signals with and without aircraft vibration

using the front-end which was driven by the emulated TCXO clock signals (Figure 3.1 on page 54). We used a software receiver to process the collected GPS data and obtained the clock error from the PVT solutions at 20 Hz rate. Then, we calculated the power spectral density of the clock error data. Finally, Figure 3.6 presents the calculated phase noise PSD of the static and vibration-affected TCXO clock signals.

In Figure 3.6, we prove that the emulated clock signals follow the desired spectra, which were programmed into the clock emulator. Through these processes, we successfully imposed the aircraft vibration effects on the TCXO signals. We confirm that the clock signal truly represents the behavior of the clock when it is on-board a vibrating aircraft.

3.4 Construction of Ionospheric Scintillation Effects on GPS RF Signals

Ionospheric scintillation is caused by local ionosphere plasma anomalies. The process of electron-ion recombination after sunset is not uniform. Therefore, patches containing irregular electron density are formed. If the GPS signal passes through these patches, the signal is diffracted and scattered. This causes the signal received on the ground to have temporal fluctuations in both amplitude and phase. Figure 3.7, analyzed by Goodman in 1990 [75],

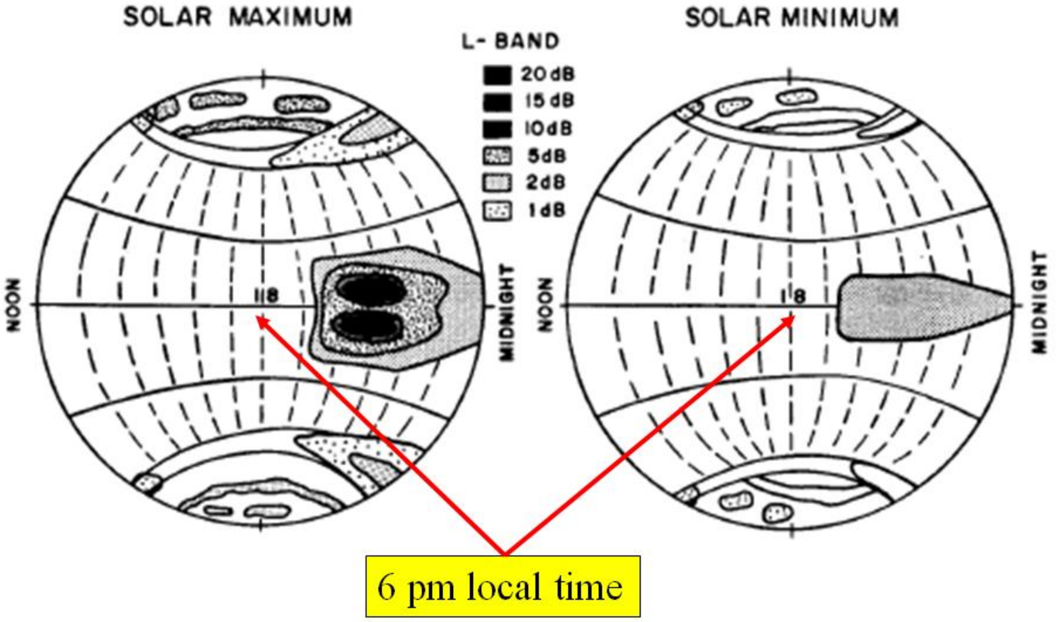

Figure 3.7: Fading depths at L-band worldwide for solar maximum and solar minimum given by [75]

shows the distribution of fading depths at L-band worldwide for solar maximum and solar minimum. Results in Figure 3.7 were derived from WBMOD [68]. From that figure, we find the deepest power fading occurs in equatorial regions. This pictorial chart also reveals the temporal information about scintillation. The center point of each plot in Figure 3.7 represents 6 pm local time. So scintillation usually appears after sunset and continues from 7 pm to midnight. This model result is also supported by the recent real scintillation data analysis done by Beniguel in 2007. One of Beniguel's results is shown in Figure 3.8 on the following page. This figure demonstrates the local time dependency of ionospheric scintillation. From Figure 3.8, we also find that S_4 becomes larger than 0.7 after 7 pm local time and keeps high values through midnight. The scintillation becomes subtle after 6 am local time. The data for Figure 3.8 on the next page were collected from N'Djamena (Tchad), Cayenne (French Guyana), Douala (Cameroon) in October 2006, October 2006, and 2004, respectively. More than 764 thousands of samples were collected from GPS receivers deployed in the above three locations, all of which are located in equatorial regions.

Either the power fading or the phase variations may lead to the loss of signal lock or increases in measurement errors. As a result, the occurrence of ionospheric scintillation is a continuity threat to a GPS receiver.

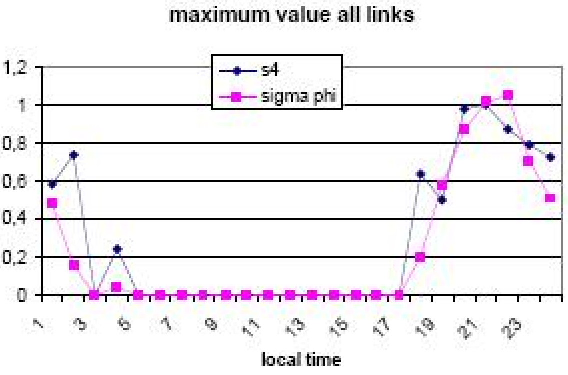

Figure 3.8: Local time dependency of ionospheric scintillation provided by [76]

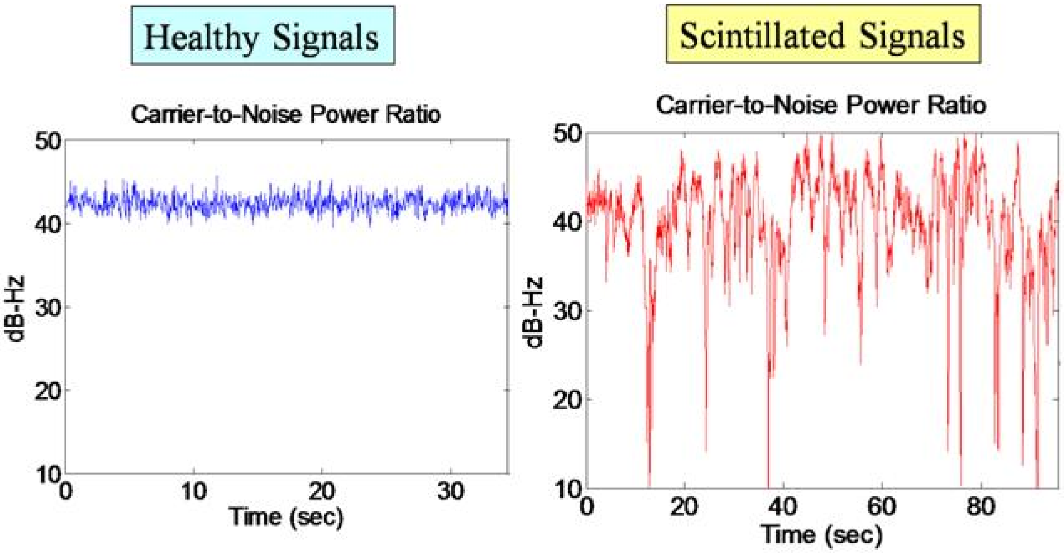

Figure 3.9: GPS Signal-to-Noise Power Ratio for Healthy and Scintillated Signals

Figure 3.9 (repeated from Figure 1.1 on page 3) illustrates the impact of scintillation on the signal power of the GPS. The left plot of Figure 3.9 portrays a healthy GPS signal. Typical healthy signals usually range between 40 and 50 dB-Hz. However, if ionospheric scintillation occurs, at some moments, we have deep power fades up to 20 dB or more. As you can see in the right plot of Figure 3.9, during a period of 90 seconds, there are 10 power fades of up to 20 dB or more. The signal level during these deep power fades is below the receiver tracking threshold.

To evaluate the performance of the designed GPS receiver under scintillation condition, we construct the scintillation effects on GPS signals using the Spirent 7700 GPS constellation simulator (courtesy of SiRF, Inc.). The healthy GPS RF signals can easily be generated by

- Data Source: Dr. Theodore Beach, AFRL
- Location: Ascension Island (UTC + 0)
- Time: 7 pm to 10 pm on
  18, 19, 21 March, 2001, the last solar maximum

Figure 3.10: Scintillated GPS Data Collection on Ascension Island, 2001

the simulator. Both the amplitude and the phase scintillations are added onto the healthy signals by applying external commands to the simulator.

To have high fidelity amplitude scintillation for generating the external commands, we utilize real scintillated GPS intermediate frequency (IF) data provided by the Air Force Research Lab (AFRL). The scintillated GPS IF data were collected on Ascension Island in 2001 (Figure 3.10).

The profile of the amplitude scintillation (the right plot of Figure 3.9) is extracted using a NordNav software receiver to process the scintillated GPS IF data. Furthermore, this amplitude profile is applied as the external commands to dither the original healthy GPS signals. Each simulated channel is one-to-one mapped to the real scintillated GPS channels. As a result, we have built a realistic amplitude scintillation scenario in the GPS simulator based on real data.

In addition to the amplitude scintillation, we also consider the phase scintillation effects on GPS signals. Since the phase of the real scintillated GPS data cannot be tracked due to the deep power fading, we cannot obtain the phase scintillation directly from the real data. Instead, we generate the profile of the phase scintillation based on the most widely accepted inverse power law model of phase scintillation [8]. Likewise, this phase scintillation is applied as the external commands to dither the original healthy phase generated in the simulator.

With the aforementioned implementations, we obtain GPS RF signals with realistic scintillation effects.

3.5 Summary

In summary, we have demonstrated the processes of building up a high fidelity hardware simulation for use as the database of this research. From this process, we have confirmed that the vibration impact on a TCXO has been generated in the collected GPS IF data. This is done using a high quality clock signal generator as an external clock source of a GPS front-end for IF data sampling. The clock signal generator has been configured such that it generates the clock sinusoidal signals based on the vibration-affected phase noise PSD. Power fading due to scintillation also has been successfully reproduced by a GPS constellation simulator based on the real scintillated GPS data. As a result, the hardware simulation has been conducted with the key error sources to the carrier tracking loop included.

Chapter 4

Theoretical and Experimental Results

4.1 Chapter Overview

This chapter demonstrates how the concept of Doppler-aiding is implemented and verified. First of all, the technique of Doppler-aiding is implemented in a part of a GPS software receiver. Through the work of this research, a novel GPS software receiver, which runs PLL and FLL for carrier tracking in parallel has been developed. Furthermore, the receiver is also flexible in applying Doppler-aiding from either simulated inertial measurements or the technique of vector processing. Note that a phase-locked loop (PLL), also called a coherent tracking loop, tracks the phase of the received GPS signal. In contrast, a frequency-locked loop (FLL), also called a non-coherent tracking loop, tracks the frequency of the received GPS signal. The tracking loop configurations such as bandwidth and predetection integration time of the software receiver are determined by a trade-off study in this chapter. The trade-off study is based on the model analysis presented in Chapter 2 on page 12. A useful contour of bandwidth versus C/N_0 is introduced to optimize loop bandwidth. This contour is generated by the theory introduced in Chapter 2. Details of completing the contour will be presented in Section 4.3. In short, the contour consists of all the possible combinations of bandwidths versus C/N_0 given various conditions of ionospheric scintillation and dynamic stresses. Finally, the experimental setup and data collection method are illustrated. The results of this dissertation are presented in the end of this chapter.

4.2 Doppler-Aided GPS Receiver

The main idea to resolve the scintillation problem is to find the aiding source, which allows us to reduce the receiver bandwidth. In this work, we consider two Doppler-aiding sources: vector processing and an inertial system. Vector processing calculates the Doppler estimate of the weak channels using the strong channels. This aiding method [2] is effective when there are at least four or more strong channels. However, if there are fewer than four healthy channels, the Doppler estimate must rely on an external measurement, i.e., an inertial system. The Doppler-aiding using an inertial system is achieved by tightly coupling the GPS receiver with the inertial measurement unit (IMU). In addition to the two Doppler aiding sources, we also evaluate the performance of applying Doppler aiding to both coherent and non-coherent carrier tracking loops.

Figure 4.1 demonstrates the architecture of the Doppler-aided GPS receiver developed in this work. The receiver runs coherent and non-coherent carrier tracking in parallel. Depending on the availability of pseudorange measurements, the navigation function switches between the two tracking modes to calculate position, velocity, and time (PVT). The bit and frame synchronization of the non-coherent tracking is provided by the coherent tracking channels.

To apply Doppler aiding to both carrier tracking loops, the function of channel Doppler estimation is developed (Figure 4.1). This Doppler estimate function is synchronized to each channel according to the navigation data bit boundary of each channel. This Doppler estimate function utilizes two inputs to calculate the channel Doppler frequencies. The first input is the PVT of the satellite and the second input is the PVT of the receiver.

The satellite's PVT information is obtained from the navigation data at the beginning of the tracking process.

The PVT of the receiver is from either the vector processing or tightly coupling the GPS with the IMU. Using vector processing requires at least four healthy satellites. We implement this technique to validate the receiver effectiveness under the strong scintillation condition.

However, if there are fewer than four healthy channels, the receiver uses the Doppler estimates by tightly coupling the GPS with the IMU. In this chapter, we analyze:

1. receiver with no aiding;
2. receiver with vector aiding; and,

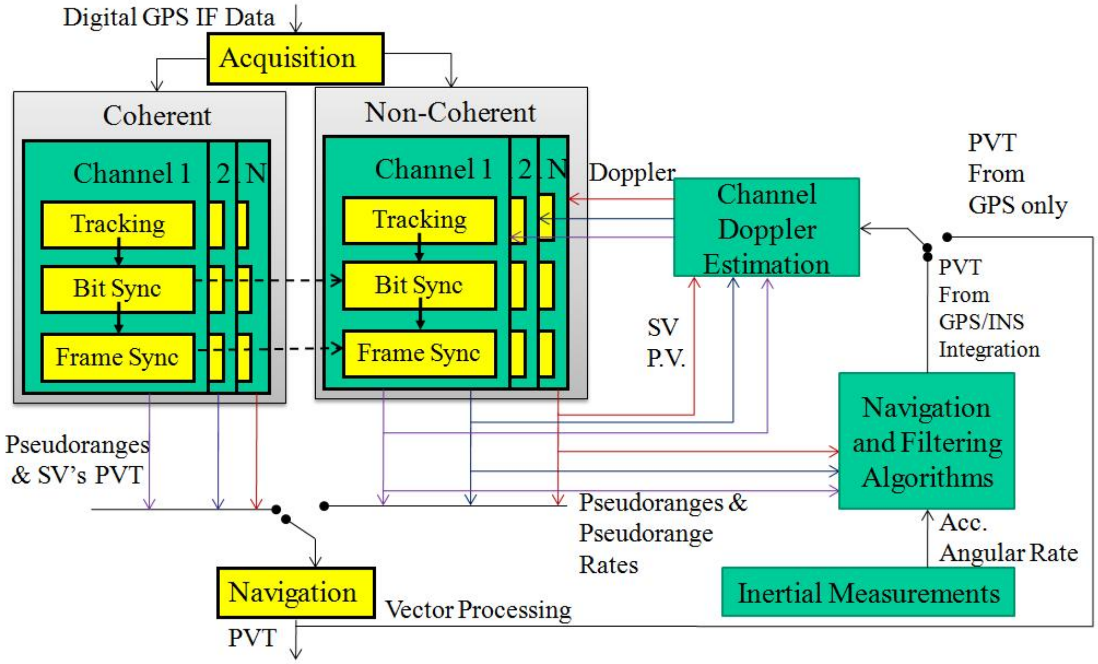

Figure 4.1: Doppler-Aided GPS Receiver

3. receiver with inertial aiding.

As illustrated in Figure 4.1, the IMU measures accelerations and platform angular rates. These inertial measurements are fed into navigation and filtering algorithms [66] combined with the measurements of the pseudorange as well as the pseudorange rate from the GPS receiver. The output of this blending function is the best estimated PVT of the receiver. This PVT is then fed into the channel Doppler estimation to calculate the Doppler frequency of each channel.

In this work, the tightly-coupled GPS/INS is simulated by applying noise to the reference Doppler provided by the Spirent simulator. The quality of the simulated Doppler estimate is designed to represent the use of the automotive grade IMU that is defined quantitatively in [67].

By applying this technique, the bandwidth of the carrier tracking loops can be reduced, such that more radio interference is tolerated by the GPS receiver. Section 4.3 quantitatively evaluates the performance of the technique of tightly-coupled GPS/INS.

4.3 Discussions of Model Results

This section presents the design parameters of the Doppler-aided GPS receiver illustrated in Figure 4.1. The two key parameters of the carrier tracking loop are the loop noise bandwidth and the pre-detection integration time (PDI). To be more capable of noise rejection, a GPS receiver needs a longer PDI. However, because of the presence of the navigation data bits in the current GPS L1 signal, the maximum value of PDI is limited to 20 ms [27]. Longer PDI can be enabled by predicting the navigation bits and removing their influence. This technique is not considered here. Given the PDI, the loop noise bandwidth is the parameter for the carrier tracking loop designer. We prefer the noise bandwidth to be as low as possible for better noise rejection. However, the gain of the reduced bandwidth comes with a limitation. We cannot reduce the bandwidth indefinitely. This issue leads to the discussion of the trade-off study for the bandwidth in Section 4.3.1.

4.3.1 Trade-Off Study for the Optimal Bandwidth

Figure 4.2 shows the concept of designing the loop bandwidth to obtain a smaller frequency error in the non-coherent carrier tracking loop. The red line represents the frequency error due to thermal noise and the amplitude scintillation, whereas the blue line indicates the frequency error due to dynamics and the phase scintillation. As can be seen in Figure 4.2, decreasing the bandwidth reduces the error due to thermal noise and amplitude scintillation (red line), but increases the error due to dynamics and phase scintillation (blue line).

The idea of Doppler-aiding is to shift the blue line as low as possible by removing the platform dynamics. When the platform dynamics are removed, a lower loop bandwidth can be applied in the carrier tracking loop. Furthermore, the clock dynamics start to dominate the frequency or phase error when Doppler-aiding is implemented. Note that the phase scintillation is comparable to the phase errors due to the TCXO. Therefore, the clock dynamics and the phase scintillation prevent the reduction of the loop bandwidth. For every combination of the red and blue lines, there is an optimal loop bandwidth. In Subsections 4.3.2 and 4.3.3, we present the final results of the trade-off study for coherent and non-coherent tracking loops, respectively.

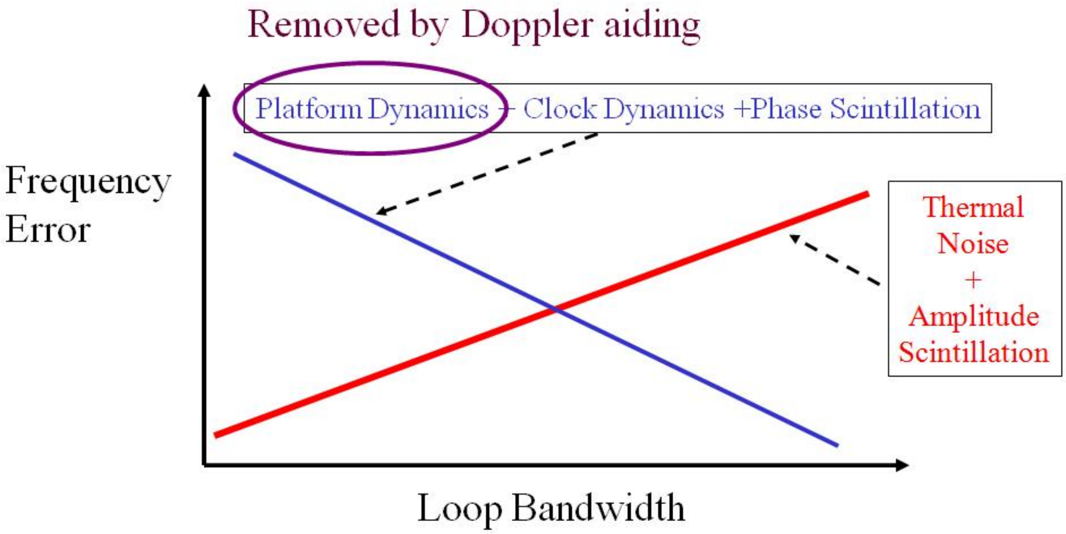

Figure 4.2: The trade-off study of Loop Bandwidth

4.3.2 Bandwidth versus C/N_0 Contour for Coherent Tracking (PLL)

In this subsection, we discuss the method used to determine the optimal bandwidth of the coherent carrier tracking loop. Figure 4.3 demonstrates the contour of feasible bandwidth as a function of C/N_0. Imagine that if we draw curves with different loop bandwidths in Figure 2.10 on page 33, each curve may intersect the one-sigma tracking threshold at two points. One is at the minimum allowable bandwidth and the other is at the maximum allowable bandwidth. The collections of all of the possible intersections comprise the contour shown in Figure 4.3. Therefore, the boundary of the contour represents the tracking threshold. Any combination of bandwidth and C/N_0 within the contour indicates that phase lock can be achieved. The region of phase-locked is defined as the feasible region. It is preferred that the feasible region be as large as possible. The optimal bandwidth via the model analysis is represented at the lower-left corner of the contour. From Figure 4.3, we discover that there is a gain of 3 dB by applying Doppler-aiding to a coherent tracking architecture under conditions including strong amplitude scintillation, phase scintillation, aircraft dynamics, and aircraft vibration-affected TCXO. The lowest allowable C/N_0 for these conditions with Doppler aiding is 30 dB-Hz.

This result indicates that the Doppler-aided coherent carrier tracking is not robust to strong scintillation. Note that the clock is TCXO and the IMU is an automotive grade IMU. An expensive IMU for Doppler-aided coherent tracking is not the focus in this work.

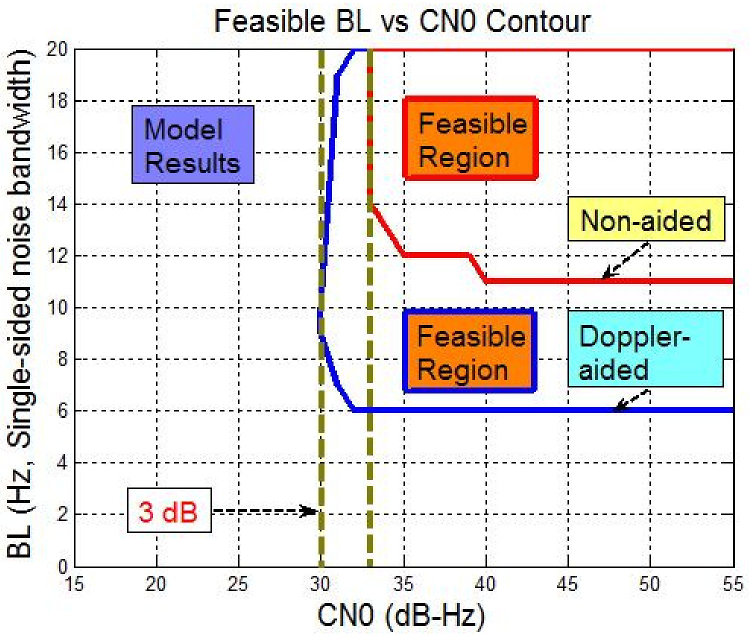

Figure 4.3: Bandwidth versus C/N_0 Contour for Coherent Tracking (PLL). BL is the single-sided noise bandwidth of the PLL.

4.3.3 Bandwidth versus C/N_0 Contour for Non-Coherent Tracking (FLL)

In contrast to the coherent tracking, the Doppler-aided non-coherent tracking architecture has a gain of 4 dB (Figure 4.4 on the next page). We can reduce the bandwidth of the frequency-locked loop from 2 Hz down to 0.3 Hz. The lowest allowable C/N_0 is 23 dB-Hz. As will be seen in Section 4.4, the Doppler-aided non-coherent tracking loop is robust to the conditions considered.

Comparing Figure 4.4 on the facing page with Figure 4.3, we find that the allowable signal strength for the non-coherent tracking is 7 dB lower than the signal strength for the coherent tracking (from 30 dB-Hz down to 23 dB-Hz). Why can the bandwidth be more reduced for the non-coherent than the coherent tracking loops? The key difference is the slope of the blue line in Figure 4.2 on the preceding page. The slope of the blue line for the coherent tracking loop is steeper than the blue line for the non-coherent tracking loop. This means that the increase in tracking errors due to platform dynamics, clock dynamics, and phase scintillation while decreasing the loop bandwidth is more severe for the coherent loop than for the non-coherent loop. As a result, we can have more bandwidth reduction for the non-coherent than for the coherent tracking loops.

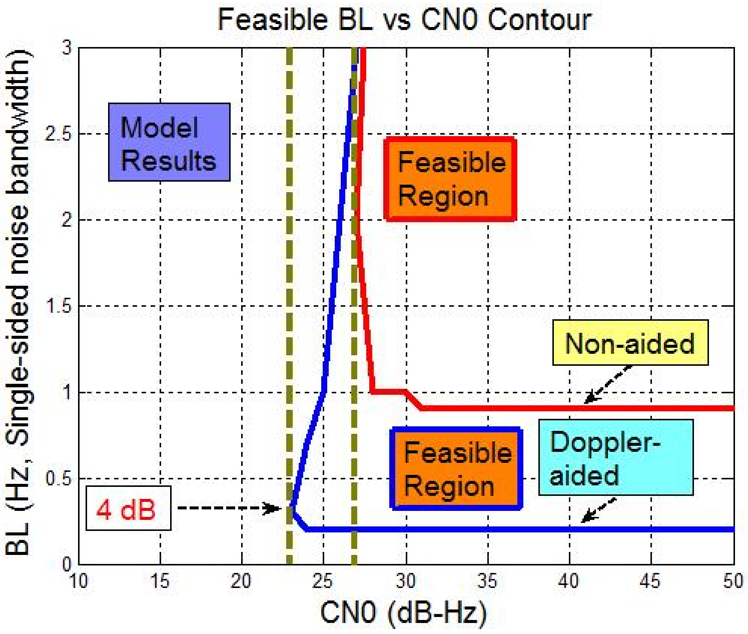

Figure 4.4: Bandwidth versus C/N_0 Contour for Non-Coherent Tracking (FLL). BL is the single-sided noise bandwidth of the FLL.

4.4 Experiments and Results

4.4.1 Data Collection

Thus far, we have covered steps to build high-fidelity GPS RF signals including scintillations, platform dynamics, and vibration-affected TCXO. In this section, we demonstrate the overall experimental setup.

Figure 4.5 (repeated from Figure 3.1 on page 54) portrays the flow diagram for collecting the GPS RF signals. The scenario of aircraft landing using GPS in equatorial regions is created in the Spirent simulator. The scintillation commands are used to modify the amplitude and the phase of the healthy signals in the simulator. At the output of the simulator, the scintillated GPS RF signals are generated. The GPS RF signals are then collected using the NordNav front-end to store the IF data. The NordNav front-end utilizes external clock signals to generate the replica GPS signals. The external clock is the aforementioned clock emulator. The vibration-affected TCXO clock signal is generated using the clock emulator. With this experimental setup, a realistic scenario for aircraft landing using GPS under strong scintillation conditions is created.

Note that there is an assumption in the scenario. The GPS RF signals are designed to be

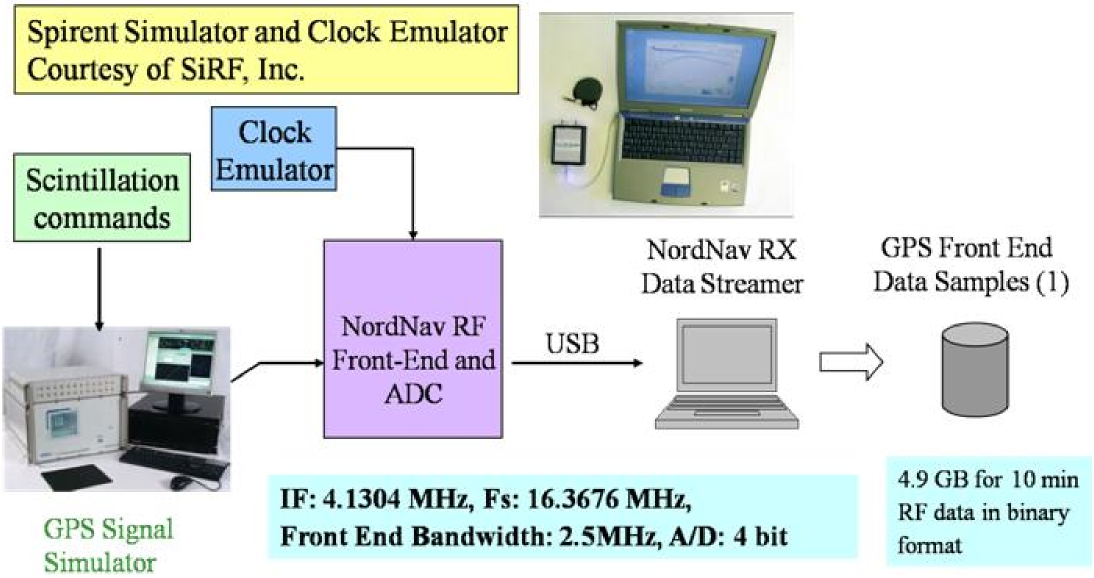

Figure 4.5: The Experimental Setup

healthy for the first two minutes. Scintillation occurs at the beginning of the third minute and lasts for seven minutes. With this setup, the navigation data bits are decoded within the first two minutes. Furthermore, this arrangement allows us to focus on the performance of carrier tracking during the period of strong scintillation. The analysis of bit error rate (BER) under strong scintillation is recommended for future work.

The collected IF data are then processed by the designed GPS software receiver for testing performance of various combinations of Doppler-aiding sources and tracking architectures (Figure 4.1).

4.4.2 Experimental Results

The performance of the designed receiver is evaluated based on the RMS-smoothed code pseudorange measurement. Figure 4.6 defines the metric that we use for comparison. In this work, the target smoothed code pseudorange error is 0.36 meter. The criterion of 0.36 meter comes from the required steady state value of RMS pseudorange error at the minimum signal levels for airborne accuracy designator A in RTCA DO-229D [25].

Figure 4.7 and Figure 4.8 illustrate the profile of the power fading for the channel that we will use to present the RMS range error.

Figure 4.9 on page 73 reveals the results of RMS error for various tracking architectures.

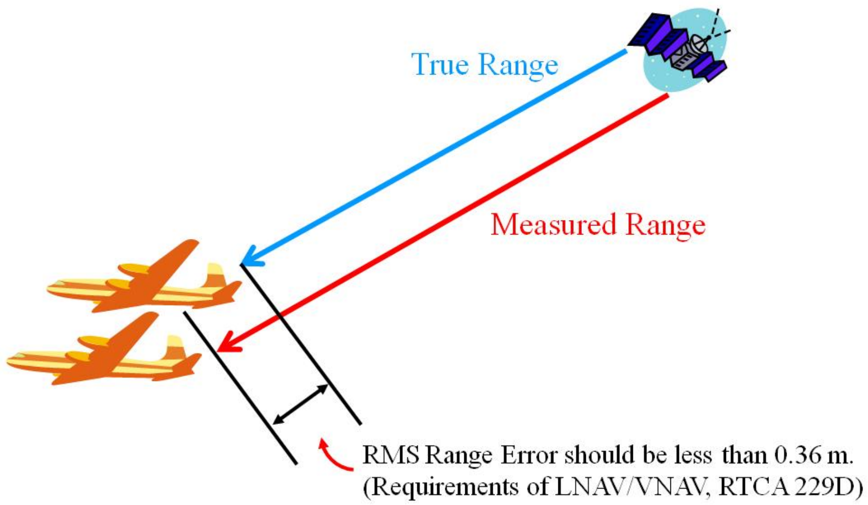

Figure 4.6: The RMS Smoothed Pseudorange Error

From Figure 4.9, we see that the unaided coherent tracking loop cannot operate continuously during this strong scintillation. The jumps of the blue curve indicate cycle slips during deep power fading. The performance of the unaided non-coherent tracking loop is better than the unaided coherent tracking loop. However, the RMS value is larger than the requirement. In addition, we have noticed that the unaided non-coherent loop also lost frequency lock during a few of the deep fades.

After applying those two Doppler-aiding techniques to the non-coherent tracking loop, the pink and the red curves in Figure 4.9 demonstrate the effectiveness of Doppler-aiding.

Figure 4.10 presents the vertical error and velocity error of Doppler-aided non-coherent tracking architecture. In Figure 4.10, there are seven channels, five of which are affected by scintillation. In Figure 4.10, we demonstrate that the receiver does not drop any channel during moments of deep power fading. This means that the receiver operates continuously without losing the satellite geometry. Furthermore, for the same scintillation conditions, or specifically the same signal levels, the conventional PLL receiver loses lock every time.

4.5 Summary

We have built a realistic channel model for aircraft landing under scintillation conditions. We have demonstrated that a Doppler-aided non-coherent tracking loop can provide continuous operation with the required pseudorange accuracy under strong scintillation conditions. Two

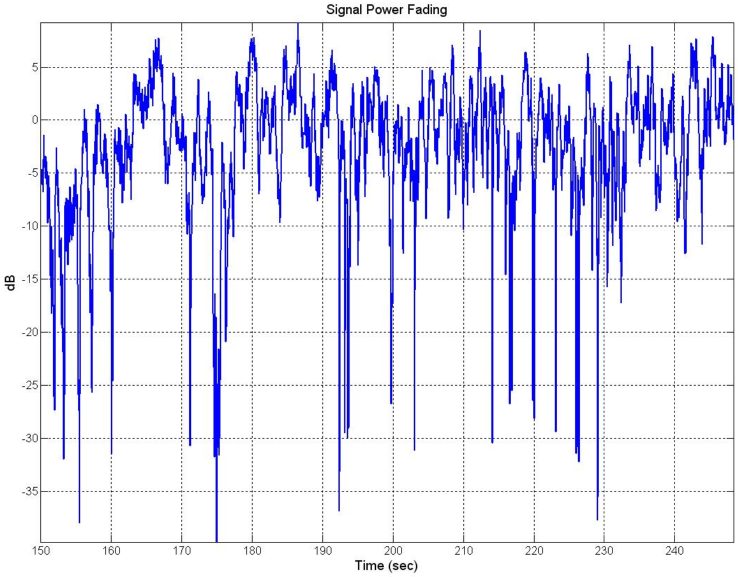

Figure 4.7: The Profile of Signal Power Fading

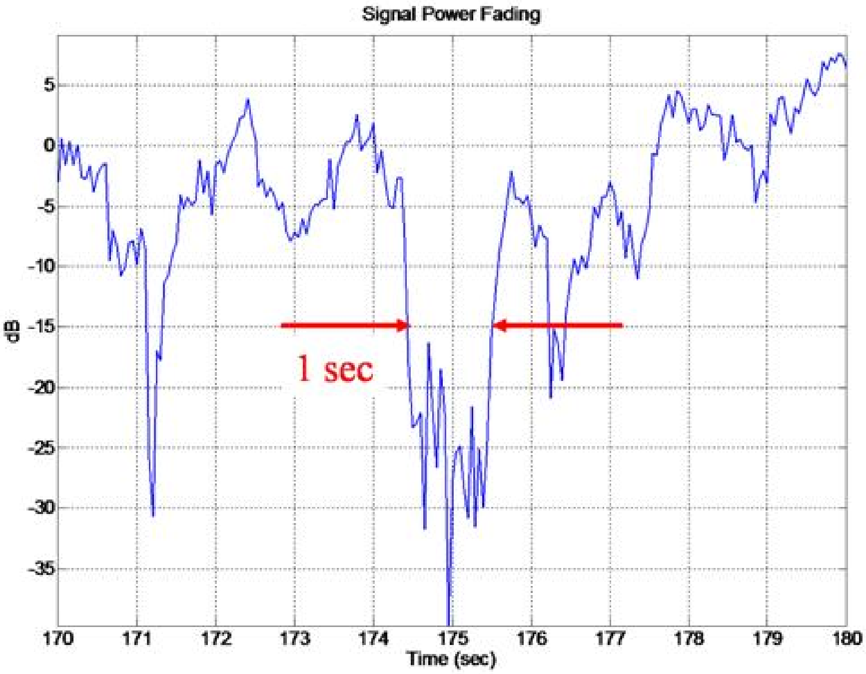

Figure 4.8: The Profile of Signal Power Fading (Zoomed in)

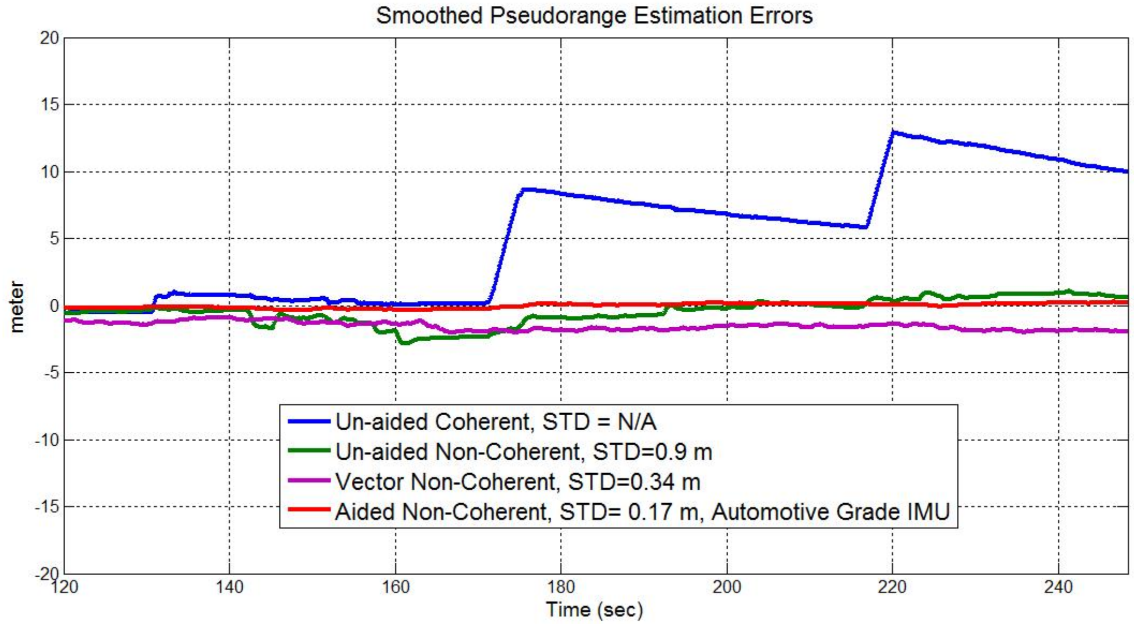

Figure 4.9: The Smoothed Pseudo-range Error

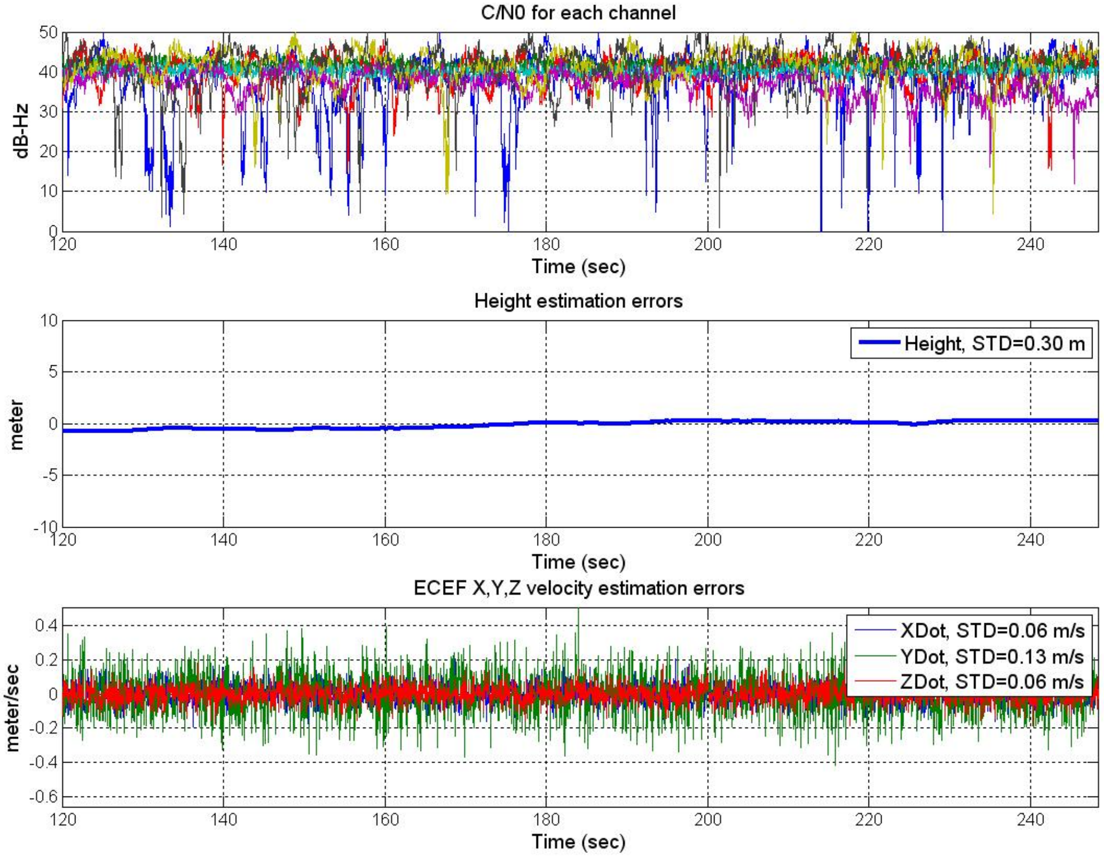

Figure 4.10: Vertical and Velocity Errors

effective Doppler aiding sources have been tested:

vector processing and the tightly coupled GPS with an automotive grade IMU.

Chapter 5

Probability Density Function and Stability Properties for a Cross-Product Frequency-Locked Loop

5.1 Chapter Overview

First of all, this chapter provides the work beyond understanding the impact of scintillation. The work in this chapter provides the background for analyzing the bit error rate (BER); probability of losing lock; and, integrity of a GPS receiver which uses an FLL as its carrier tracking loop. The success of analyzing the BER, probability of losing lock, and integrity depend on the knowledge of the probability density function (PDF) for the frequency estimate by the FLL. Solving for the PDF is the purpose of this work while the use of the PDF for the aforementioned analysis is not the focus of this work.

In this chapter, we wish to emphasize that we completed the following analyses of the FLL behavior based on its nonlinear model for the first time.

1. Analyzing the stability of the FLL based on the deterministic nonlinear model in the absence of noise.

2. Deriving the stochastic model of the FLL and the corresponding governing equation of the PDF.

3. Realizing that the aforementioned governing equation of the PDF is indeed a Fokker-Planck equation (FPE), which is also a governing equation of the PLL's PDF.
4. Applying the Crank-Nicolson method to solve the transient PDFs of the FLL.
5. Determining the existence and the solution of the steady-state PDF for the FLL.
6. Reducing the Fokker-Planck equation (FPE) to a second-order nonlinear ordinary differential equation (ODE) given the existence of the steady-state solution.
7. Confirming that the solution from the FPE matches with the solution from the ODE.

This chapter presents the details of the above emphasized points. In the following sections, we will start with the basics and the previous work on FLL. Then, the fundamentals lead to the comprehensive nonlinear analysis of the FLL. Finally, the numerical results for the analysis will be presented. The error PDF described in Chapter 2 is the error PDF of a PLL. However, the error PDF of an FLL has not yet been derived. In this chapter, we analyze the nonlinear model of the FLL and derive the error PDF of the FLL. The PDF of the FLL solved in this chapter then can be applied in Chapter 2 to evaluate the BER or probability of losing lock for a receiver using FLL as its carrier tracking loop.

5.2 Background of the FLL

The frequency locked-loop (FLL) has received new attention for modern Global Navigation Satellite Systems (GNSS) receivers, especially for its performance in severe noise interference and high dynamic environments. It has been shown that an FLL is more robust to interference and dynamics than a phase locked-loop (PLL). Therefore, it is beneficial to use an FLL as a fallback tracking loop when the primary PLL is unable to maintain carrier tracking in hostile environments. Besides tracking, it is also crucial to preserve the Bit Error Rate (BER) of the data demodulation and the probability of losing lock when a receiver operates based on FLL. These characteristics rely on the probability density function (PDF) of the frequency estimate made by the frequency discriminator in the FLL. However, the PDF has not been determined as of yet. The purpose of this chapter is to solve the PDF and evaluate the stability region which is essential for determining the statistics of loss of lock. In this work, a nonlinear model was developed and the corresponding Fokker-Planck equation (FPE) for the cross-product FLL was derived. The PDF of the frequency estimate was then solved applying the Crank-Nicolson numerical method.

The use of a frequency-locked loop (FLL) can be traced back to the 1930s [59], when an FLL was referred to as an automatic frequency control (AFC) loop. The function of an FLL in a GNSS receiver is to steer the frequency of the replica carrier close enough to the frequency of the received carrier such that a further data demodulation is possible. Instead of a coherent tracking, meaning that the signal phase is tracked by a phase-locked loop (PLL), an FLL performs non-coherent tracking only. For example, only the frequency in the carrier is tracked, assuming that the phase is uniformly distributed over $[0, 2\pi]$. It is believed that an FLL is more robust in the presence of noise interference in high dynamic environments than a PLL [60]. The applications of an FLL can generally be divided into two categories, in which an FLL can be used to improve the initial tracking of a PLL [19] or used as a backup tracking loop when the received signal power is weak for a short period [61]. Hence, investigating the performance of an FLL used in a GNSS receiver is significant and important.

Research on the linear model analysis of various types of FLLs has already been accomplished [21, 60]. The noise performance of the FLL in the presence of Gaussian noise has been evaluated in [21, 60]. However, the probability density function (PDF) of an FLL has not been solved. Obtaining the PDF is crucial to evaluating the bit error rate (BER) in the demodulation process. Moreover, estimating the probability of losing lock also relies on the PDF of the FLL.

The objective of the present chapter is to develop the nonlinear model of the cross-product FLL, evaluate the nonlinear stability characteristics in the absence of noise, and solve for the PDF in the presence of noise.

5.3 Basic Operation of the Cross-Product FLL

In this section, the operation of the cross-product FLL is reviewed without providing details of the mathematical derivations. For the details, references [21, 60] are recommended. Figure 5.1 (repeated from Figure 2.11 on page 35) illustrates the configuration of the cross-product FLL. The essential characteristic of this FLL is a cross-product frequency discriminator, which is a conventional FLL design in modern digital baseband implementation [60]. With

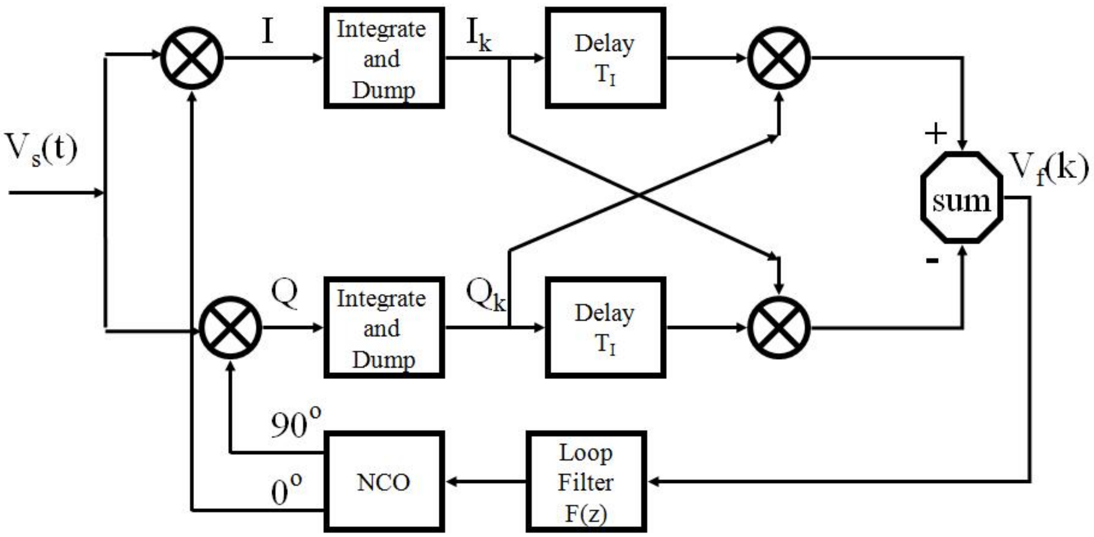

Figure 5.1: Cross Product FLL

the exception of the cross-product discriminator, the functionality depicted in Figure 5.1 is the well-known Costas loop, which is based on an architecture of a carrier tracking loop using two multipliers fed with the in-phase and quadrature replica carriers [62].

The input signal, $V_s(t)$, is assumed to be a carrier, at a frequency of ω_0, modulated with differentially-encoded data and corrupted by an additive white Gaussian noise with a spectral density of $N_0/2$. $V_s(t)$ is then multiplied by the local replica carrier, at a frequency of ω_1, generated by the numerically-controlled oscillator (NCO). The multiplications were performed by the in-phase and quadrature replica carrier to produce the I and Q channels, respectively. The I and Q channels are then passed through the integrate-and-dump filters to further reject the input noise prior to performing the frequency error determination in the following step. Prior to explaining the details of the frequency discriminator, we define a complex signal composed of the outputs of the integrate-and-dump filters, I_k and Q_k , as the following:

$$\overline{V_s}(k) = I_k + jQ_k \tag{5.1}$$

The operation of the cross-product frequency discriminator is the cross product of the current sample of $\overline{V_s}(k)$ with the previous sample of $\overline{V_s}(k)$. This operation is suggested by [21]

$$\begin{aligned} V_f(k) &= \overline{V_s}(k)\overline{\times V_s}(k-1) \\ &= I_{k-1}Q_k - Q_{k-1}I_k \\ &= d_k d_{k-1} A^2 sinc^2\left(\frac{\triangle\omega T_I}{2}\right) \cdot sin\left(\triangle\omega T_I\right) + N(k) \end{aligned} \tag{5.2}$$

where

d_k is the data symbol at the kth integrate-and-dump step;

A is signal amplitude;

$\triangle\omega = \omega_0 - \omega_1$;

T_I is the period of the integration;

$sinc(x) = \frac{sin(x)}{x}$; and,

$N(k)$ is the noise term.

Obviously, the sign of $V_f(k)$ depends on the sign of the symbol product $d_k d_{k-1}$. The sign changes can be removed by performing the dot product of the current sample, $\overline{V_s}(k)$, with the previous sample of $\overline{V_s}(k)$ [21, 60]. The output of the dot-product operator is then used as decision feedback to remove the sign changes in Eq.(5.2). In this work, we assume that the data have been wiped off by the dot-product operation. This assumption is reasonable since we are solving for the generic performance of a carrier tracking loop. Without loss of generality, one can further assume that the input signal is a pure sinusoidal carrier. The plot of the frequency discriminator, assuming that it is noise free is illustrated in Figure 5.2. Note that the frequency error presented in Figure 5.2 has been normalized by multiplying $\triangle f$ by the integration time T_I.

In Figure 5.2, we observe that unlike the periodic property of the phase discriminator in a PLL [38], there is no exact periodicity in the frequency discriminator. The main lock point is located at the origin. Once the frequency error deviates away from the first zero-crossing point, the loop starts to lose lock. As can be seen in Figure 5.2, the characteristic of the discriminator is close to linear when the value of $\triangle f \cdot T_I$ is small. A rule-of-thumb threshold for preserving this linearity assumption is when [28]

$$\triangle f \cdot T_I \leq \frac{1}{12} \cong 0.083 \tag{5.3}$$

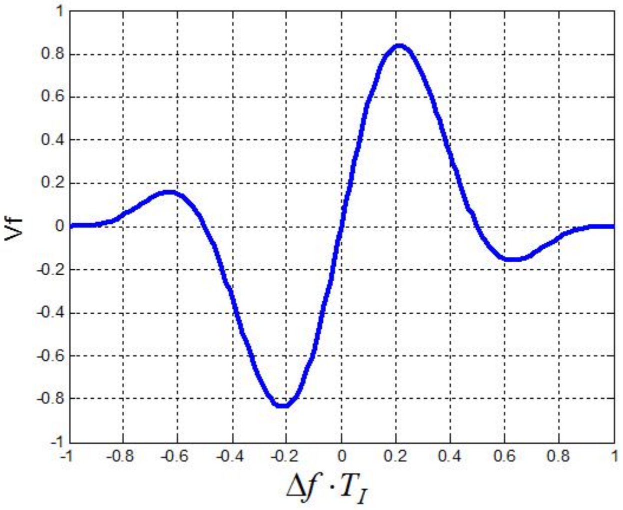

Figure 5.2: Cross Product FLL Discriminator Curve

Although the input signal is corrupted by the Gaussian noise, $N(k)$ in Eq.(5.2), in fact, is not Gaussian-distributed noise because of the nonlinear process of the discriminator. It is proved that $N(k)$ is zero mean and uncorrelated between successive samples [21]. To advance the model analysis, one usually assumes that $N(k)$ is Gaussian. As a result, given that the noise at the input signal is white Gaussian noise with two-sided spectral density $N_0/2$ and the pre-detection baseband bandwidth, $1/T_I$, one can obtain the mean, variance or the second moment, and power spectral density (PSD) of $N(k)$ as [21]

$$E[N(k)] = 0; \tag{5.4}$$

$$E[N^2(k)] = \frac{2N_0^2}{T_I}\left[\frac{2C}{N_0} + \frac{1}{T_I}\right];\ and, \tag{5.5}$$

$$S_N(f) = N_0^2\left[\frac{2C}{N_0} + \frac{1}{T_I}\right](two - sided) \tag{5.6}$$

where C/N_0 is the signal-power to noise-power density ratio.

With the assumption of Eq.(5.3), a spectral analysis is performed based on the linear model of the FLL. Thus, the normalized tracking error variance of the cross-product FLL is [27, p.381]

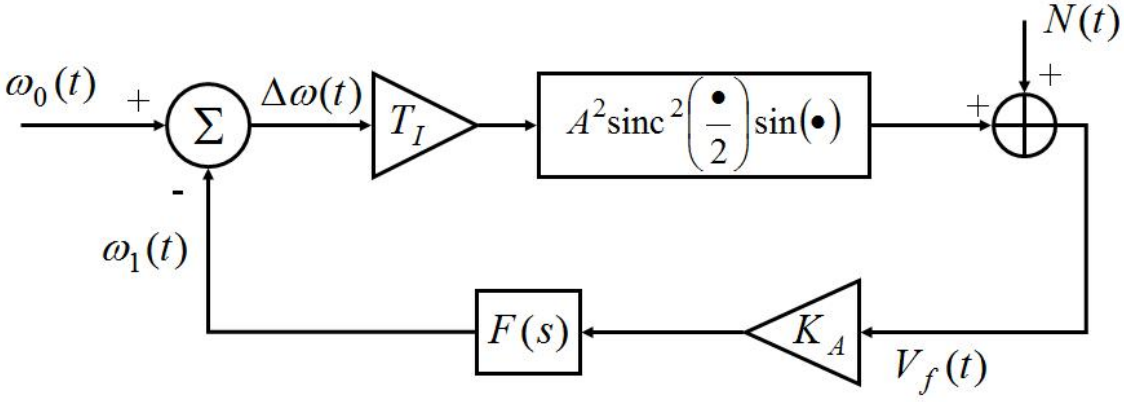

Figure 5.3: Nonlinear Model of the Cross Product FLL

$$\sigma^2_{\triangle f T_I} = \frac{1}{4\pi^2}\frac{4B_n}{\frac{C}{N_0}}\left[1 + \frac{1}{2T_I\frac{C}{N_0}}\right] \tag{5.7}$$

where B_n , in Hz, is the one-sided noise bandwidth of the closed-loop FLL. It should be noted that the normalized tracking error variance in Eq.(5.7) is dimensionless.

5.4 Nonlinear Model and Stability of the FLL in the Absence of Noise

5.4.1 Nonlinear Model

Given the block diagram in Figure 5.1 on page 78 and the characteristic of the cross-product discriminator in Eq.(5.2) on page 79, the nonlinear model representing the cross-product FLL is derived in Figure 5.3. The additive noise, $N(t)$, which will be temporarily ignored in this section and will be considered in Section 5.5 on page 85, has the properties described in Eqs. (5.2) through (5.6).

$F(s)$ is the loop filter represented in the Laplace domain, and K_A is the loop gain. Note that the carrier NCO in an FLL does not act as an integrator. It is simply a means of converting a frequency number to the sine and cosine of the frequency [27, p.384]. Therefore, the order of the closed-loop is the same as the order of the loop filter.

To simplify the nonlinear analysis, we investigate the performance of the first-order loop FLL. In fact, the famous Tikhonov PDF for a PLL is based on the model of a first-order nonlinear PLL [38]. The Tikhonov PDF has been used for analyzing the integrity and word error rate of a GPS receiver using a PLL for its carrier tracking loop [12]. As mentioned at the beginning of this chapter, the purpose of this chapter is to determine the corresponding PDF for an FLL, which plays the same role as the Tikhonov PDF of a PLL. However, due to the complexity of the FLL, it is unfeasible to solve for the closed form solution. Thus, a numerical approach is proposed in Section 5.6 on page 90.

In the first-order loop, $F(s) = 1/s$. We can obtain the following state equation describing the closed-loop in Figure 5.3 as:

$$\begin{aligned}\frac{d\triangle\omega(t)}{dt} = & \frac{d\omega_0(t)}{dt} \\ & - A^2 K_A sinc^2\left[\frac{\triangle\omega(t)T_I}{2}\right] sin\left(\triangle\omega(t)T_I\right) \\ & - K_A N(t)\end{aligned} \tag{5.8}$$

We consider primarily frequency-ramp sinusoidal inputs, so that $d\omega_0(t)/dt = v$ which is a constant in units of rad/sec^2. If v is 0, we say that the loop is unstressed. In the unstressed case, the distribution of the tracking error would be a zero mean. If v is nonzero, then FLL is dynamically stressed and the mean of the tracking error would be biased from 0. Let $z = \triangle f \cdot T_I$ and we have

$\triangle\omega = \frac{2\pi}{T_I}z$ and $d\triangle\omega = \frac{2\pi}{T_I}dz$.

Performing the change of variables in $\triangle\omega$ and z for Eq.(5.8), we obtain the following governing equation of the cross-product FLL in the domain of the normalized frequency error.

$$\frac{dz(t)}{dt} = \frac{T_I}{2\pi}\left[v - A^2 K_A sinc^2(\pi z) sin\left(2\pi z\right) - K_A N(t)\right] \tag{5.9}$$

Eq.(5.9) is a stochastic and first-order ordinary differential equation which fully describes the behavior of the cross-product FLL. The solution of $z(t)$ in Eq.(5.9) is of interest. In the next section, I will solve the statistical solution to Eq.(5.9). In the remainder of this section, I discuss the stability performance in the absence of noise, which is essential to obtaining the boundary of z where the FLL loses lock.

5.4.2 Stability of the FLL in the Absence of Noise

The system trajectory described in Eq.(5.9) is investigated without considering the noise term, $N(t)$. For the first-order loop, the loop noise bandwidth is [27]

$$B_n = \frac{A^2 K_A}{4} \tag{5.10}$$

The input frequency ramp, v, can be written as

$$v = 2\pi \overset{\bullet}{\triangle} f_i \tag{5.11}$$

where $\overset{\bullet}{\triangle} f_i$ is the frequency ramp input in Hz/sec.

Substituting Eqs. (5.10) and (5.11) into Eq.(5.9) and ignoring the noise term, we have

$$\frac{dz(t)}{dt} = \left[\overset{\bullet}{\triangle} f_i T_I - \frac{4B_n T_I}{2\pi} sinc^2(\pi z) sin\,(2\pi z) \right] \tag{5.12}$$

The system trajectory of Eq.(5.12) is described in Figure 5.4 for the case of an unstressed FLL. The system is stable when it reaches a value of z for which $dz/dt = 0$. There are multiple stable points for the system. However, the FLL is allowed to be locked only within the main lobe for a physical meaning of tracking. One discovers that the system moves toward the right when $dz/dt > 0$ and vice versa. Therefore, there are dynamically-stable points for $z = \ldots -1, 0, 1, 2 \ldots$, where the system will return to the stable points after any perturbation of z in either direction. However, for other stable points, any perturbation of z in either direction causes the system to move until it reaches the next dynamically-stable point.

We define the dynamically-stable point in the main lobe, z_{lock}, and the next non-dynamically stable point, z_{loss}. Once z is larger than z_{loss}, the system moves farther away from the main lobe and stops when it reaches the next stable point. However, when the system is dynamically stressed, there may be no stable points beyond z_{loss}. Figure 5.5 illustrates the issue of having only two stable points.

With a positive frequency ramp input, one can ascertain that once $z > z_{loss}$, the system migrates toward infinity and never returns to any stable points. Thus, z_{loss} is the threshold at which the FLL starts to lose lock. If the input frequency ramp increases again, the whole curve shifts upward such that z_{lock} and z_{loss} move further toward each other. This means

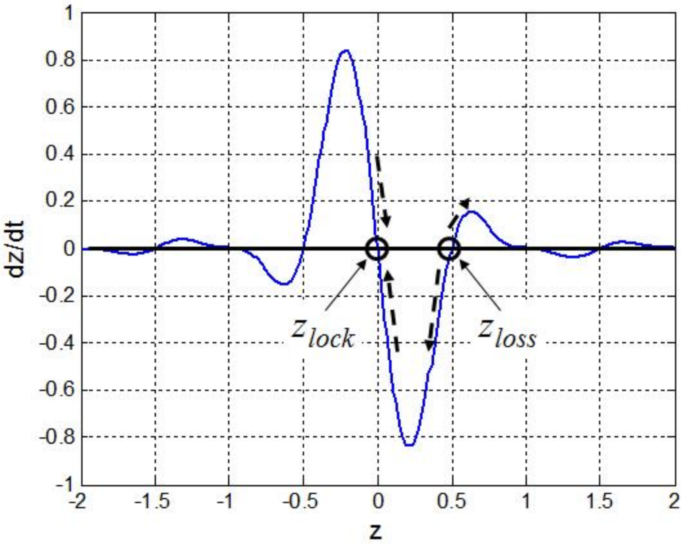

Figure 5.4: System Trajectory, Non-Stressed. The normalized frequency ramp input is zero, and $T_I = 1,\ 4B_n = 2\pi$

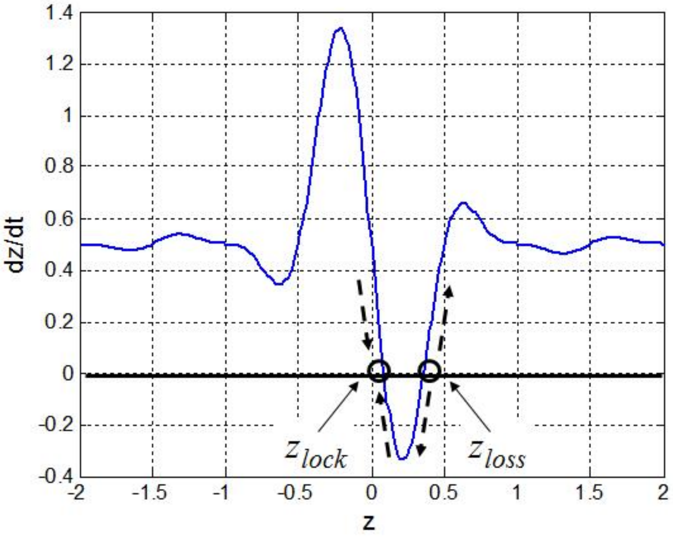

Figure 5.5: System Trajectory, Dynamically Stressed. The normalized frequency ramp input is 0.5 Hz, and $T_I = 1, 4B_n = 2\pi$

that the FLL is more likely to lose lock under stronger dynamics. The frequency ramp for the case that z_{lock} and z_{loss} coincide is the maximum allowable frequency ramp for the first-order FLL. Any input beyond the maximum allowable ramp frequency causes the FLL to become unstable.

Knowing the values of z_{loss} is crucial for evaluating the probability of loss-of-lock in the presence of noise. The probability of loss-of-lock is defined as

$$p\left(z > z_{loss} \mid B_{n,} \dot{\triangle f}_i T_I\right) \tag{5.13}$$

Determining the value of Eq.(5.13) relies on the PDF of z, which is provided in the next section.

5.5 Fokker-Planck Equation and the PDF of the Cross-Product FLL

In this section, a statistical approach to Eq.(5.9) on page 82 is discussed. Eq.(5.9) is a stochastic ordinary differential equation driven by Gaussian noise, $N(t)$. Therefore, given $z(t)$, the PDF of dz/dt is Gaussian, too. As a result, the complete solution of $z(t)$ is determined by its PDF.

Since $N(t)$ is Gaussian, the process described in Eq.(5.9) is a Markov process and the relation governing a PDF of a Markov process is given as [38]

$$\frac{\partial p(z,t)}{\partial t} = \sum_{n=1}^{\infty} \frac{(-1)^n}{n!} \frac{\partial^n}{\partial z^n} \left[A_n(z) p(z,t)\right] \tag{5.14}$$

with the initial condition $p(z,0) = \delta(z - z_0)$, where $p(z,t)$ is the PDF of $z(t)$; $A_n(z)$ is the limit of the nth moment of the increment of the process $\triangle z$, given that it started at some value z at time t, normalized by the time increment, $\triangle t$, as the latter approaches zero, and $\delta(z - z_0)$ is the Dirac delta function.

It is evident that for a first-order stochastic ordinary differential equation with a white Gaussian driving function, the quantities $A_n(z)$ vanish for n greater than 2 [38]. Accordingly, Eq.(5.14) becomes the well-known Fokker-Planck equation (FPE) as

$$\begin{aligned}\frac{\partial p(z,t)}{\partial t} =& -\frac{\partial}{\partial z}[A_1(z)p(z,t)] + \frac{1}{2}\frac{\partial^2}{\partial z^2}[A_2(z)p(z,t)] \\ p(z,0) =& \delta(z - z_0)\end{aligned} \tag{5.15}$$

In order to obtain the corresponding FPE for the cross-product FLL, we must determine the quantities of $A_1(z)$ and $A_2(z)$ according to Eq.(5.9). From the definition of $A_n(z)$ in Eq.(5.14), the expression of $A_n(z)$ can be written as [38]

$$\begin{aligned}A_n(z) &= \lim_{\triangle t \to 0} \frac{1}{\triangle t} \int_{-\infty}^{\infty} (\triangle z)^n p(\triangle z \mid z) d(\triangle z) \\ &= \lim_{\triangle t \to 0} \frac{E\left[(\triangle z)^n \mid z\right]}{\triangle t}\end{aligned} \tag{5.16}$$

By integrating both sides of Eq.(5.9) on page 82 over the infinitesimal interval from t to $t + \triangle t$, we have

$$\begin{aligned}\triangle z &= z(t + \triangle t) - z(t) \\ &= \frac{T_I}{2\pi}\left[v - A^2 K_A sinc^2(\pi z) sin(2\pi z)\right] \triangle t \\ & -\frac{T_I}{2\pi} K_A \int\limits_{t}^{t+\triangle t} N(t) dt\end{aligned} \tag{5.17}$$

Recalling that $N(t)$ is white Gaussian noise of zero mean and the two-sided spectral density given in Eq.(5.6) on page 80, we find that the first two normalized moments of Eq.(5.16) are

$$\begin{aligned}A_1(z) &= \lim_{\triangle t \to 0} \frac{E\left[(\triangle z) \mid z\right]}{\triangle t} \\ &= \frac{T_I}{2\pi}\left[v - A^2 K_A sinc^2(\pi z) sin(2\pi z)\right]\end{aligned} \tag{5.18}$$

$$\begin{aligned}
A_2(z) &= \lim_{\triangle t \to 0} \frac{E\left[(\triangle z)^2 \mid z\right]}{\triangle t} \\
&= \lim_{\triangle t \to 0} \left(\frac{T_I}{2\pi}\right)^2 \frac{K_A^2}{\triangle t} \int\limits_{t}^{t+\triangle t} \int\limits_{t}^{t+\triangle t} E\left[N(u)N(v)\right] dudv \\
&= \lim_{\triangle t \to 0} \left(\frac{T_I}{2\pi}\right)^2 \frac{K_A^2}{\triangle t} N_0^2 \left[\frac{2C}{N_0} + \frac{1}{T_I}\right] \int\limits_{t}^{t+\triangle t} \int\limits_{t}^{t+\triangle t} \delta(u-v) dudv \\
&= \left(\frac{T_I}{2\pi}\right)^2 K_A^2 N_0^2 \left[\frac{2C}{N_0} + \frac{1}{T_I}\right] \qquad (5.19)
\end{aligned}$$

In addition to the initial condition stated in Eq.(5.15), solving the FPE requires two boundary conditions. It is a fact that the total area under a PDF should be 1, which is one of the boundary conditions; accordingly the two tails of the PDF approach 0 as the independent variable approaches plus and minus infinities. The two boundary conditions are then defined as follows:

The normalization condition is

$$\int\limits_{-\infty}^{\infty} p(z,t)dz = 1 \qquad (5.20)$$

and the symmetric condition is

$$p(\infty,t) = p(-\infty,t) = 0 \quad for \;\; all \;\; t \qquad (5.21)$$

Note that the symmetric condition is a heritage of the normalized condition, since the total area has to be finite and, therefore, the two tails have to vanish at the infinities.

To further advance the solution of the FPE, we parameterize the FPE in terms of B_n ; C/N_0 ; T_I ; the normalized initial frequency offset, $\triangle f_i T_I$; and, the normalized frequency ramp input, $\triangle \dot{f}_i T_I$. To obtain the final FPE, we start the derivations from Eq.(5.15) and repeat Eq.(5.15) here.

$$\begin{aligned}
\frac{\partial p(z,t)}{\partial t} &= -\frac{\partial}{\partial z}[A_1(z)p(z,t)] + \frac{1}{2}\frac{\partial^2}{\partial z^2}[A_2(z)p(z,t)] \qquad (5.22) \\
p(z,0) &= \delta(z-z_0) \qquad (5.23)
\end{aligned}$$

where $A_1(z)$ and $A_2(z)$ are given in Eqs. (5.18) and (5.19). Let $\eta = A_2(z)$. Given the one-sided noise bandwidth in Eq.(5.10) on page 83 and the variance of the normalized frequency error in Eq.(5.7) on page 81, we can find that

$$\eta = 2T_I^2 \cdot B_n \cdot \sigma^2_{\triangle f T_I} \tag{5.24}$$

If we define $\alpha = \frac{A^2 K_A}{K_A^2 N_0^2 \left[\frac{2C}{N_0} + \frac{1}{T_I}\right]}$ and $\beta = \frac{v}{K_A^2 N_0^2 \left[\frac{2C}{N_0} + \frac{1}{T_I}\right]}$, then Eq.(5.22) can be written as

$$\begin{aligned} \frac{\partial p(z,t)}{\partial t} =& \eta \left\{ -\frac{\partial}{\partial z}[D(z)p(z,t)] + \frac{1}{2}\frac{\partial^2}{\partial z^2} p(z,t) \right\}; \\ p(z,0) =& \delta(z - z_0); \\ \int_{-\infty}^{\infty} p(z,t)dz = 1;& \\ p(\infty) =& p(-\infty) = 0 \end{aligned} \tag{5.25}$$

where $D(z) = \frac{2\pi}{T_I}\left[\beta - \alpha sinc^2(\pi z) sin(2\pi z)\right]$. For the first order FLL here, the dimensionless dynamic stress can be written as [27, p.389]

$$\gamma_z = \frac{\frac{T_I}{2\pi} v}{4B_n} = \frac{\overset{\bullet}{\triangle} f_i T_I}{4B_n} \quad \text{dimensionless} \tag{5.26}$$

With γ_z defined in Eq.(5.26) and $\sigma^2_{\triangle f T_I}$ in Eq.(5.7), α and β can be further represented as

$$\alpha = \frac{1}{2\pi^2 \sigma^2_{\triangle f T_I}} \tag{5.27}$$

$$\beta = \alpha \cdot \frac{2\pi}{T_I} \gamma_z \tag{5.28}$$

Finally, Eqs. (5.25), (5.26), (5.27), (5.28), and (5.7) on page 81 completely define the FPE for the cross-product FLL in the domain of the normalized frequency error. Furthermore, the FPE is in terms of B_n; C/N_0; T_I; normalized initial frequency offset, $\triangle f_i T_I$; and, normalized frequency ramp input, $\overset{\bullet}{\triangle} f_i T_I$. Eq.(5.29) summarizes the final FPE to be solved.

$$\begin{aligned}\frac{\partial p(z,t)}{\partial t} =& \eta\left\{-\frac{\partial}{\partial z}[D(z)p(z,t)]+\frac{1}{2}\frac{\partial^2}{\partial z^2}p(z,t)\right\}; \\ p(z,0) =& \delta(z-z_0); \\ \int\limits_{-\infty}^{\infty} p(z,t)dz =& 1; \\ p(\infty,t) =& p(-\infty,t)=0\end{aligned} \tag{5.29}$$

where

$z=\triangle f \cdot T_I$, the normalized frequency error;

$p(z,t)$ =the PDF of the FLL in the domain of the normalized frequency error;

$\eta=2T_I^2 \cdot B_n \cdot \sigma^2_{\triangle f T_I}$;

$D(z)=\frac{2\pi}{T_I}\left[\beta-\alpha sinc^2(\pi z)sin(2\pi z)\right]$;

$\alpha=\frac{1}{2\pi^2\sigma^2_{\triangle f T_I}}$;

$\beta=\alpha\cdot\frac{2\pi}{T_I}\gamma_z$;

$\gamma_z=\frac{\overset{\bullet}{\triangle} f_i T_I}{4B_n}$, the dimensionless dynamic stress; and,

$z_0=\Delta f_i \cdot T_I$, the normalized initial frequency offset.

Because of the nonlinearity of the discriminator (shown in $D(z)$), the closed-form representation of the steady-state PDF is not yet achievable. A numerical method of solving the FPE is discussed in the next section.

5.6 Numerical Results using the Crank-Nicolson Method

To solve the partial differential equation of Eq.(5.29), the Crank-Nicolson method [63] was utilized. The corresponding time difference equation to Eq.(5.29) is, therefore,

$$\begin{aligned} \frac{p_i^{j+1}-p_i^j}{\triangle t} = \; & \frac{1}{2}\eta \cdot \left\{ \left[-\frac{D(z_{i+1})p_{i+1}^j - D(z_{i-1})p_{i-1}^j}{2\triangle z} + \frac{1}{2}\frac{p_{i+1}^j - 2p_i^j + p_{i-1}^j}{(\triangle z)^2} \right] \right. \\ & \left. + \left[-\frac{D(z_{i+1})p_{i+1}^{j+1} - D(z_{i-1})p_{i-1}^{j+1}}{2\triangle z} + \frac{1}{2}\frac{p_{i+1}^{j+1} - 2p_i^{j+1} + p_{i-1}^{j+1}}{(\triangle z)^2} \right] \right\} \end{aligned} \tag{5.30}$$

where the subscripts, i ,denote the spatial domain of z; and the superscripts, j , denote time. Note that $D(z)$, given in Eq.(5.29), is time independent and hence there is no superscript for $D(z)$. Figure 5.6 demonstrates the time and spatial meshes for Eq.(5.30). Given $p(z_{i,}t_j)$ at time t_j, solving Eq.(5.30) will yield the PDF at time t_{j+1} for all z_j. The initial condition for the numerical solution is the Kronecker delta function, which satisfies both the normalized conditions and the boundary conditions at the initial state. The symmetric boundary condition is approximated using an absorbing boundary condition. It is reasonable to assume that the tails of the PDF approach 0 within a finite range of z. Once the accuracy of the solution is met given an absorbing boundary condition, the solution is considered to be valid. The aforementioned accuracy was calculated from the difference of the total area under the solved PDF to 1. In other words, the normalized boundary condition is used as a metric for claiming a successful solution.

In this dissertation, the accuracy requirement is set to be 1e-12. The number of grids in the z direction was 7000 or more. Intuitively, as more grids are used for the mesh, the more accurate the results will be. However, the amount of memory on the computer limits the grid number. The required number of grids also depends on C/N_0. As expected, the PDF for a lower C/N_0 has a wider range in the z direction. Therefore, to preserve the required accuracy, more grids are needed to encompass the wider range of z. The time step size also depends on the grid size in z. The details of the trade-off between the grid size in z and the time step size are evaluated in [63].

For calculations of $D(z)$, one should know that the definition of the function in Matlab differs from what was defined in Eq.(5.2) on page 79, which says $sinc(x) = \frac{sin(x)}{x}$. In Matlab, the $sinc$ function is defined as

$$sinc(x) = \frac{sin(\pi x)}{\pi x}$$

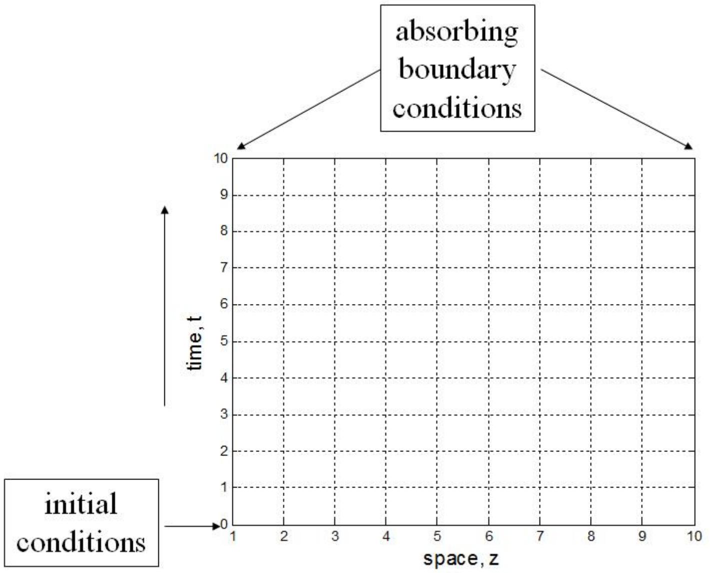

Figure 5.6: The time and spatial meshes for numerical solution of FPE

Figure 5.7 on the next page reveals one example of the PDF solution. In Figure 5.7 , there is an assumed initial frequency offset. The initial impulse is at $z = 0.05$. The green curve represents the PDF at half of the evolving time and the red curve is the PDF at the end of the evolving time. The coincidence of the green and red curves shows that the FLL has reached the steady state. Figure 5.7 also demonstrates that the steady-state error is 0 as expected for the performance of a first-order loop with an initial impulse input.

Figure 5.8 on the following page depicts another example for the case in which the PDF is dynamically stressed. The final PDF is centered at the steady-state value of the frequency error.

5.7 Discussion

Obviously, one may not examine the correlation between the system trajectory, shown in Figure 5.4 on page 84, and the PDF, shown in Figure 5.7. Remember that there are dynamically-stable points (z_{lock}) and non-dynamically stable points (z_{loss}) shown in Figure 5.4. We also call this a wavelet behavior. The dynamically-stable points means the system would be at the state with higher possibility. For example, we expect the PDF should have a peak at zero frequency error if the system is not dynamically-stressed. Furthermore, we also expect that the system should have lower possibility staying at those z_{loss}. To illustrate this correlation,

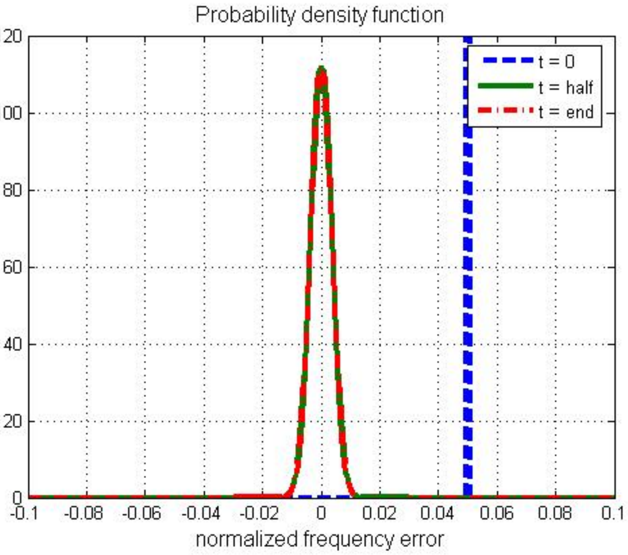

Figure 5.7: PDF of the FLL, Non-Stressed. $C/N_0 = 20\,dB - Hz$, $B = 2\,Hz$, $\triangle f_i T_I = 0.05$, and the normalized frequency ramp input is zero.

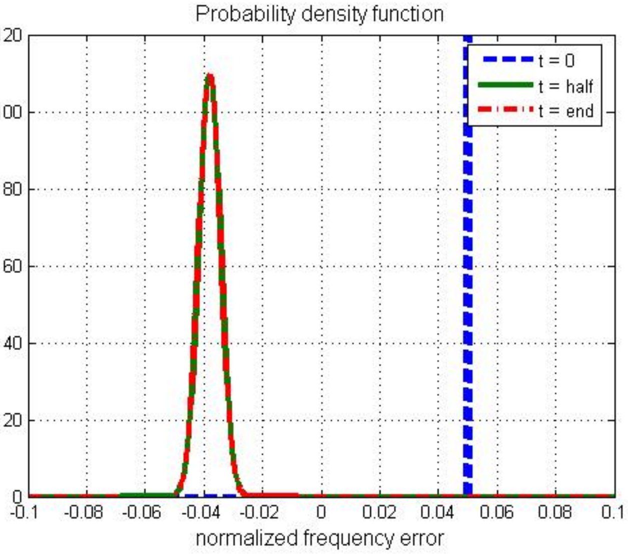

Figure 5.8: PDF of the FLL, Dynamically-Stressed. $C/N_0 = 20dB - Hz$, $B = 2Hz$, $\triangle f_i T_I = 0.05$, and the normalized frequency ramp input is -0.006 Hz.

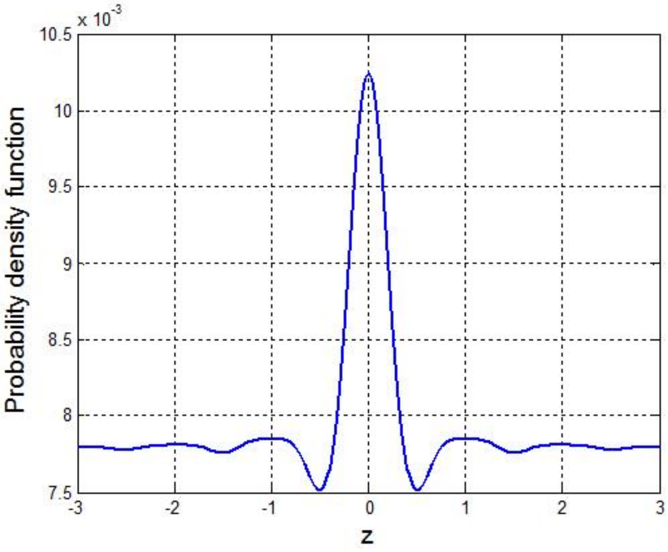

Figure 5.9: PDF of the FLL, Weak Signal. $C/N_0 = 0\,dB - Hz$, $B_n = 10\,Hz$, $\triangle f_i T_I = 0$, and the normalized frequency ramp input is zero.

a PDF with $C/N_0 = 0$ dB-Hz is plotted in Figure 5.9. From the case of a weak signal shown in Figure 5.9, we observe two troughs in the PDF for $|z| = 0.5$. This, again, reveals the fact that the z_{loss} points in Figure 5.4 are not dynamically-stable points. The system has the lowest probabilities to remain at these two troughs. The wavelet behavior, which is the characteristic of the FLL system trajectory in Figure 5.9, also represents the same behavior as observed in Figure 5.4. The system has relatively lower probabilities compared to its adjacent points, to remain at those non-dynamically stable points.

Since there is a steady-state PDF solution for the FLL, we can eliminate the time dependence of the PDF in Eq.(5.29) on page 89. The left-hand side of Eq.(5.29) becomes 0, and the PDF on the right-hand side of Eq.(5.29) does not have the variable t. As a result, Eq.(5.29) becomes a second-order nonlinear ordinary differential equation (ODE) shown in Eq.(5.31).

$$\begin{aligned} 0 &= -\frac{\partial}{\partial z}[D(z)p(z)] + \frac{1}{2}\frac{\partial^2}{\partial z^2}p(z) \\ &\int_{-\infty}^{\infty} p(z)dz = 1 \\ &p(\infty) = p(-\infty) = 0 \end{aligned} \tag{5.31}$$

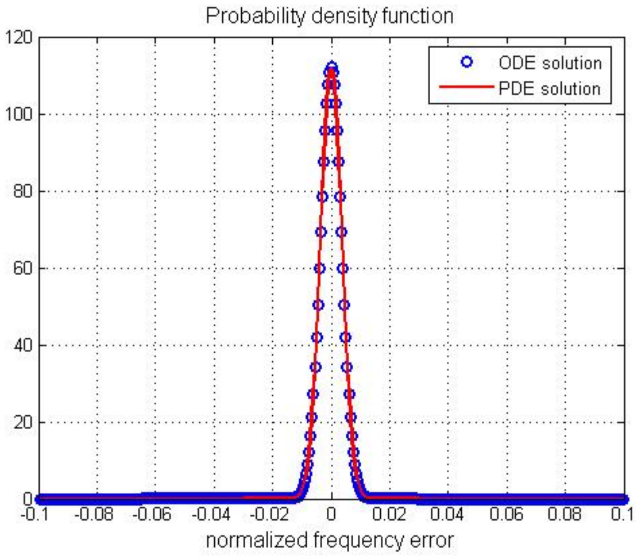

Figure 5.10: PDF of the FLL, ODE and PDE Solutions, Non-Stressed. $C/N_0 = 20\ dB - Hz$, $B_n = 2\ Hz$, $\triangle f_i T_I = 0.05$, and the normalized frequency ramp input is zero.

The solution in Eq.(5.31) is the final snapshot of the time-dependent solutions obtained from solving Eq.(5.29). A simple finite difference method was applied to solve Eq.(5.31) for the steady-state PDF. Figure 5.10 shows the solutions from both the ODE (Eq.(5.31)) and the PDE (Eq.(5.29)). The solution of the ODE further verified the PDE solution. Therefore, it is true that the steady-state PDF of the FLL can be directly solved from the ODE in Eq.(5.31) without solving the PDE in Eq.(5.29) using the Crank-Nicolson method. However, without investigating the PDE solution, we cannot conclude that the steady-state solution exists. If one is interested in the steady-state PDF of the FLL, one can directly solve the ODE in Eq.(5.31). However, if the transient properties are of interest, solving the PDE is necessary.

Once the PDF of the FLL is available, one can, for example, estimate the probability of exceeding the linear threshold given in Eq.(5.3) on page 79. Figure 5.12 shows the curve of this probability versus a different C/N_0 with a fixed noise bandwidth and integration time. The curve was obtained by calculating the tail area of the PDF beyond the linear threshold defined in Eq.(5.3) for the FLL. Figure 5.13 also shows the probability for a Costas PLL. Since the PDF of the Costas PLL has been solved [38, 64], this probability can be evaluated by using the closed-form solution. Note that the PDF of the PLL given in [38, 64] must be modified to account for the use of a Costas loop. The modified PDF of the PLL can be

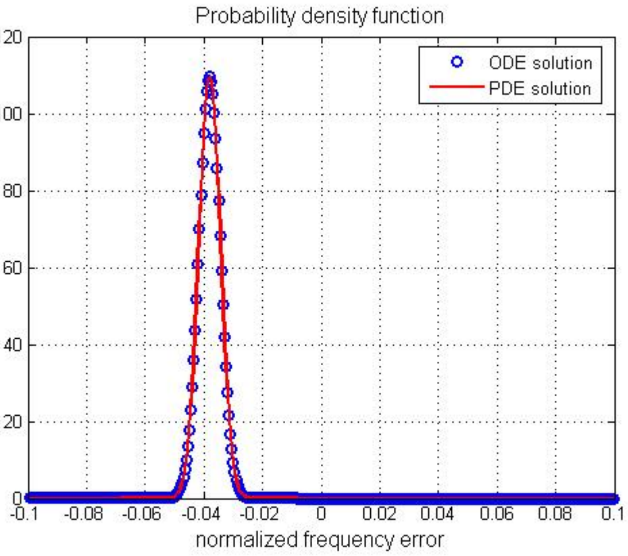

Figure 5.11: PDF of the FLL, ODE and PDE Solutions, Dynamically-Stressed. $C/N_0 = 20\, dB - Hz$, $B_n = 2\, Hz$, $\triangle f_i T_I = 0.05$, and the normalized frequency ramp input is -0.006 Hz.

found in [39, p.274] or [61]. The linear threshold of the PLL was set at 15^o [28]. Curves in both figures are all dynamically stressed. The dynamic stress is not the same for the PLL and the FLL. However, if we consider a stable case (the dynamic is not large enough to cause an unstable result for the FLL or the PLL), we have the following findings.

As seen in Figures 5.12 and 5.13, the probability of exceeding the linear threshold for the FLL is smaller than that for the Costas PLL. Figure 5.12 suggests that if the PLL does not maintain lock due to a low C/N_0 , one may switch to using FLL with good effect.

5.8 Summary

The nonlinear model of the cross-product FLL has been developed, and a stability analysis as well as the PDF for the FLL has been solved for the first time. The PDF of the FLL was solved numerically in both PDE and ODE approaches. With the PDF, one can estimate a more accurate Bit Error Rate (BER) due to imperfect frequency estimation of the FLL. Given the system trajectories of z_{lock} and z_{loss} shown in Figure 5.4 and Figure 5.5 on page 84 and the solution of the Fokker-Planck equation, one can estimate the probability of the loss-of-lock defined in Eq.(5.13) on page 85.

In conclusion, this chapter solves the probability-density function of the cross-product

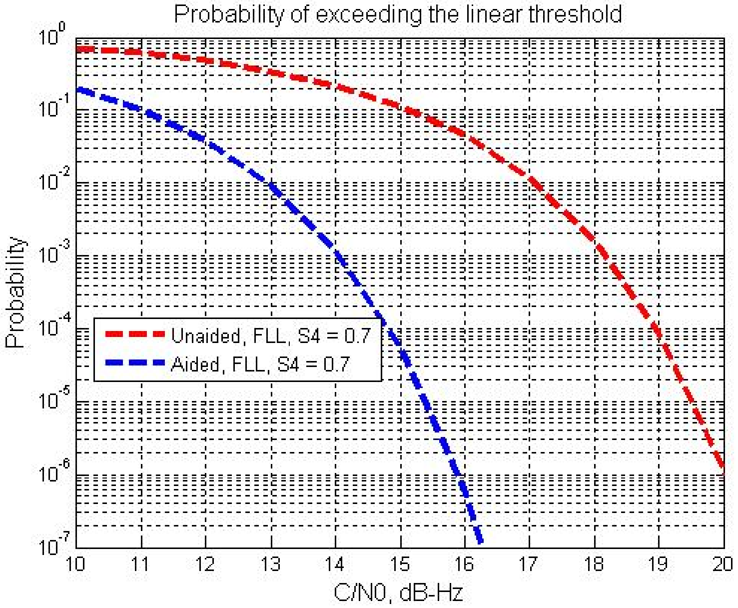

Figure 5.12: Probability of Exceeding the Linear Threshold, FLL

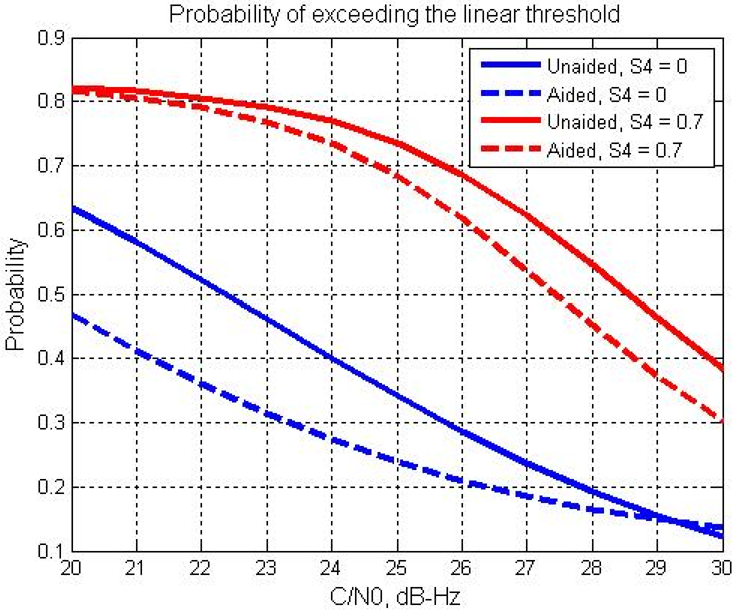

Figure 5.13: Probability of Exceeding the Linear Threshold, PLL

FLL and provides the stability analysis for evaluating the probability of the loss-of-lock for a GNSS receiver using FLL.

Chapter 6

Conclusions

6.1 Conclusions

The work in this dissertation demonstrated the design and performance of a Doppler-aided GPS navigation system for weak signals caused by strong ionospheric scintillation.

The contributions of this work are:

1. Developed and implemented a GPS hardware simulation for receiver operation in environments which include aircraft dynamic, aircraft vibration-affected receiver clock, and deep fading;

2. Validated two well known tracking architectures in this environment: inertial aiding of the GPS tracking loops and the so-called vector delay lock loop; and,

3. Developed a nonlinear model for the non-coherent tracking loop (FLL) and solved its probability density function for frequency error.

The replaced Doppler-aided GPS navigation system is capable of providing continuous navigation with the frequent occurrence of signal power fading due to strong ionospheric scintillation.

In summary, the key research results of this dissertation are:

1. Investigated the impacts of scintillation on GPS carrier tracking loops through the analysis using linear models. This analysis includes evaluating the improvements of Doppler-aiding on both Phase-Locked Loop (PLL) and Frequency-Locked Loop (FLL)

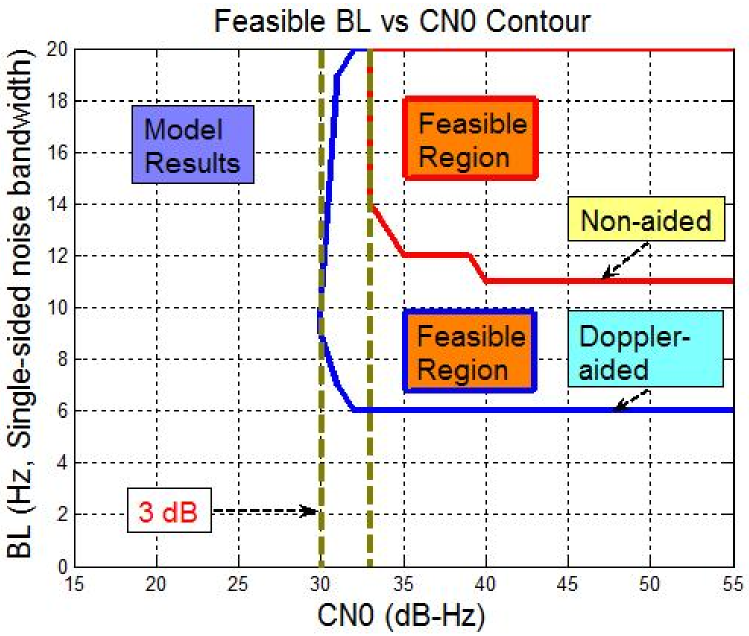

Figure 6.1: Bandwidth versus C/N_0 Contour for Coherent Tracking (PLL)

processes. Note that a phase-locked loop (PLL), also called a coherent tracking loop, tracks the phase of the received GPS signal. In contrast, a frequency-locked loop (FLL), also called a non-coherent tracking loop, tracks the frequency of the received GPS signal. The analysis was demonstrated in Chapter 2 on page 12. The key result shows that the minimum C/N_0 for the Doppler aided FLL is 7 dB lower than the minimum C/N_0 for the Doppler aided PLL. The improvement of applying the Doppler aiding on the PLL is 3 dB whereas the improvement for the aided FLL is 4 dB. Figures 6.1 and 6.2 on the next page (repeated from Figures 4.3 on page 68 and 4.4 on page 69) emphasize the findings of the analysis. These results show that it is worthwhile to apply the Doppler aiding technique to an FLL when an aided PLL is unable to maintain phase lock in the presence of ionospheric scintillation.

2. Validated the vibration effects on receiver clock via a sophisticated clock emulator. In Section 3.3 on page 55, the method was demonstrated for emulating the aircraft vibration effects on a receiver clock. Figure 3.6 on page 58, repeated here in Figure 6.3 on the following page, shows a 9 dB clock phase noise increase caused by the aircraft vibration effects.

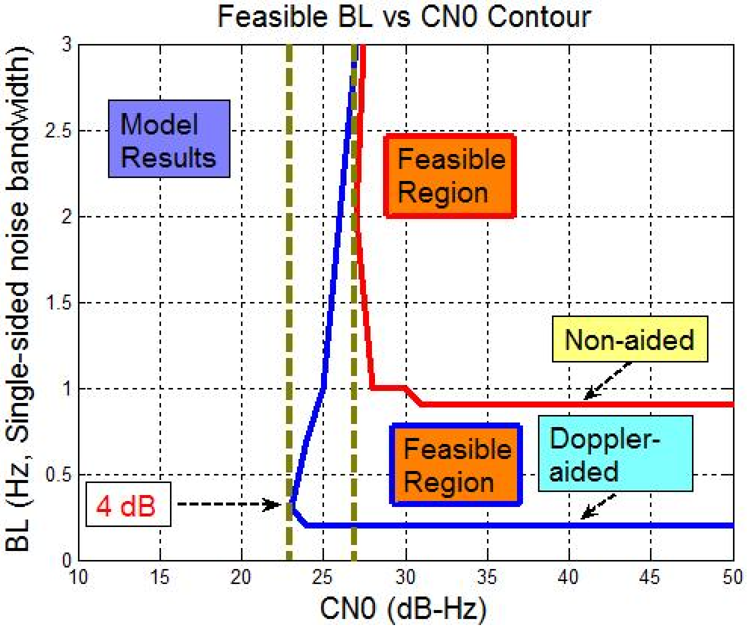

Figure 6.2: Bandwidth versus C/N_0 Contour for Non-Coherent Tracking (FLL)

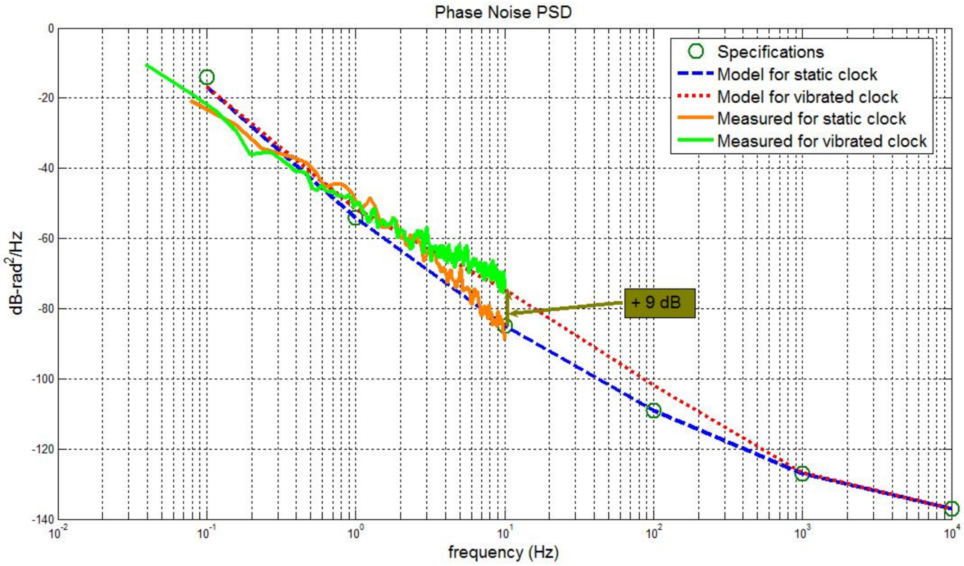

Figure 6.3: The emulated TCXO clock signals with and without aircraft vibration

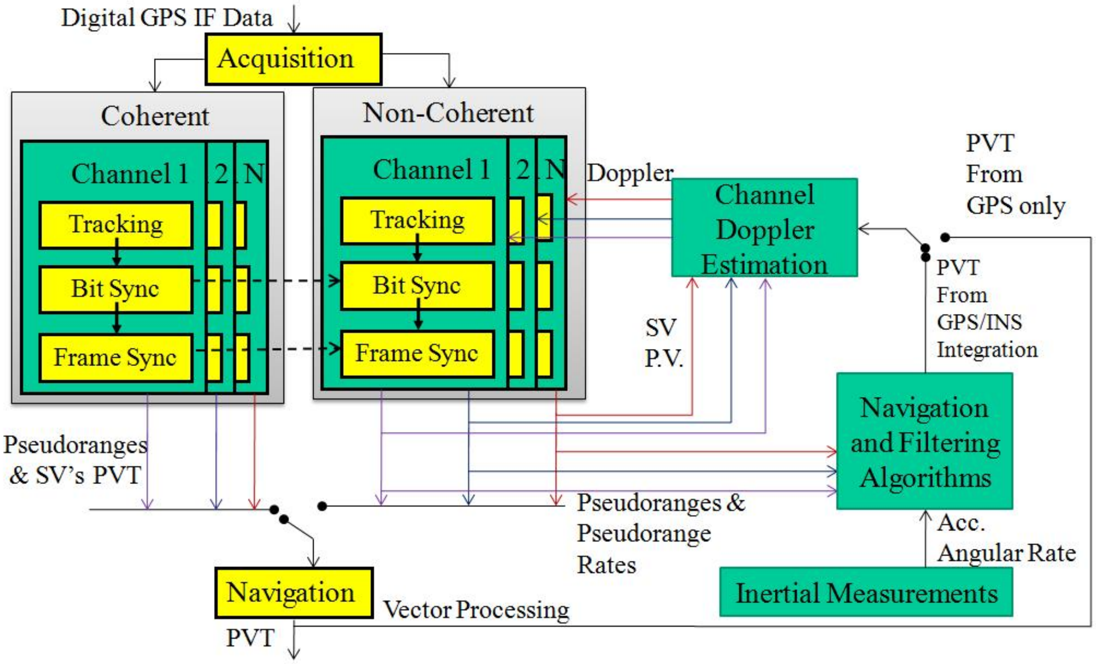

Figure 6.4: Doppler-Aided GPS Receiver

3. Realized high fidelity experiments on a GPS constellation simulator including scintillation, platform dynamics, and clock dynamics. Chapter 3 on page 52 illustrates how we enabled a hardware simulation which consisted of the considered error sources in the carrier tracking loops. Through these processes, one can obtain the GPS RF data that have been corrupted by the scintillation (extracted from real scintillated GPS data), aircraft vibration, platform dynamics, and clock dynamics.

4. Developed a software defined receiver which accomplishes both vector processing and inertial aiding for use as the Doppler aiding source. Substantial efforts went into developing a software defined receiver. Figure 6.4 (repeated from Figure 4.1 on page 65) shows the architecture of the designed software GPS receiver. This is a flexible testbed which offers options of different code and carrier tracking loops, as well as options of stand-alone, GPS/IMU, or vector FLL processing. With this software receiver, algorithms can easily be implemented as compared to the traditional hardware receiver.

In conclusion, a Doppler-aided and non-coherent tracking loop (FLL) can provide continuous operation with the required pseudo-range accuracy under strong scintillation conditions. Two effective Doppler aiding sources have been tested: vector processing and tightly coupled GPS with an automotive grade IMU. As shown in Figure 4.9 on page 73, the error of the smoothed pseudorange achieves the required accuracy in the presence of strong ionospheric scintillation. In Figure 4.10 on page 73, the position and velocity solutions are also provided continuously under strong scintillation condition.

6.2 Suggestions for Future Research

This dissertation focuses on the continuity of tracking and the accuracy of ranging under strong scintillation conditions. Yet, to implement a navigation system for aviation, one must consider not only accuracy, but also continuity, availability, and integrity. The last three items have not been studied for the scenario of a receiver operating in a strong scintillation environment. Accuracy defines the difference between the measured position and the true position. Integrity and continuity address performance of the navigation system in the presence of failures. Integrity measures the ability of the system to protect the user from inaccurate position estimates in a timely fashion. Continuity measures the navigation system's ability to complete an operation without raising an alarm. Availability is computed as the fraction of time the system is providing position fixes to the specified level of accuracy, integrity, and continuity.

The work done in this dissertation provides a method for improving the accuracy of a GPS receiver in the presence of scintillation. The technique of Doppler aiding provides a way to assist the weakest loop of a GPS receiver. As a result, the Doppler aiding process facilitates the accuracy requirement of a navigation system. However, to better understand the performance of continuity, availability, and integrity in the presence of scintillation, a global model of ionospheric scintillation is a key element. A better understanding of when, where, how often, and how severe the scintillation happens is important to evaluate continuity, availability and integrity of a navigation system. In addition, models for faulty situations must be studied to assess the performance of continuity and integrity for a navigation system under scintillation conditions.

To obtain more gains through a tightly-coupled system, one must look into the clock technology. From this study, we know that the clock dynamics limit the reduction of noise bandwidth. Consequently, the robustness to wideband noise cannot be significantly improved. More specifically, the oscillator phase noise prevents remarkable headway in the technology of a tightly-coupled system. Therefore, to advance a high performance, low cost, and chip scale clock would be a decisive step for making the tightly-coupled system practical and effectively gain more sensitivity.

In addition to the application in aviation, the technique of the tightly-coupled system has a potential use in commercial GPS receivers. For application in this category, a traditional automotive grade IMU is impractical because of its comparatively large dimension and high cost. Instead, one pays more attention to MEMS inertial sensors and optical gyros. However, the time increasing errors in these low cost and chip scale inertial sensors are harmful to a tightly-coupled system. Therefore, research into MEMS inertial sensors is highly suggested future work.

Finally, terrestrial signals are also potential candidates in the technique of Doppler-aiding. This dissertation proves the benefits of applying Doppler-aiding to the carrier tracking loops in a GPS receiver. In addition to the two sources of Doppler measurements discussed in this dissertation, one may consider other means for providing aiding to GPS receivers. Any sensors complementary to GPS signals are all potential candidates. As long as the sensors can provide the positioning function when the GPS signal is weak or not available, the technique of Doppler-aiding can be considered by integrating GPS and the external sensors. Good candidates are those terrestrial signals which are suitable for ranging. For example, Loran, TV signals, cell phone signals, and WiFi signals.

Appendix A

BER and WER for WAAS

A.1 BER for WAAS

In the previous literature, the BER of a WAAS message with FLL tracking has not been studied. We applied theorems based on Binary Symmetric Channels (BSC) and obtained the union-Bhattacharyya error bound for calculating the BER of a WAAS message with FLL tracking. Before looking at the results of the FLL, we will start the analysis for the PLL.

When using a PLL, BPSK for the WAAS signal is used except that there is a convolutional encoding with a rate of 1/2 and a constraint length of 7 imposed on WAAS messages. Therefore, 500 symbols/sec are used to represent the 250 bits/sec WAAS data bits. Applying the convolutional encoding can somehow compensate for the loss in bit energy due to its faster data rate. The BER of WAAS messages via the PLL tracking can be upper-bounded by [40, p.199]

$$P_{b,WASS}(\phi) \leq \frac{1}{2}\left[36D^{10} + 211D^{12} + 1404D^{14} + 11633D^{16}\right] \tag{A.1}$$

where for the coherent BPSK signal with the soft decision for the Viterbi decoding [40, p.196], $D = exp\left(-T_{WASS,PLL}\frac{C}{N_0}cos^2(\phi)\right)$, and $T_{WASS,PLL}$ is the symbol period of the WAAS message, 0.002 sec.

The final BER with PLL tracking in the presence of scintillation is then

$$BER_{PLL,scint} = \int_0^{\infty}\int_{-\pi/2}^{\pi/2} P_b(\phi,\rho_0)p_\phi(\phi)f_{\rho_0}(\rho_0)d\phi d\rho_0 \tag{A.2}$$

where

$f_{\rho_0}(\rho_0) = \frac{m^m \rho_0^{m-1}}{\Gamma(m)\left(\frac{C}{N_0}\right)^m} \exp\left(-\frac{m\rho_0}{\frac{C}{N_0}}\right)$ and ρ_0 represents the instantaneous carrier-to-noise density ratio of the received signal;

$P_\phi(\phi)$ is the PDF defined in Eq.(2.51) and Eq.(2.52) on page 44;

For GPS ($T_{WASS,PLL} = 0.02sec$): $P_b(\phi,\rho_0) = \frac{1}{2}erfc\left(\sqrt{T_{GPS,PLL}\rho_0}cos(\phi)\right)$; and,

For WAAS ($T_{WASS,PLL}$ = 0.002 sec): $P_b(\phi,\rho_0)$= the right hand side of Eq.(A.1) with $D = exp\left(-T_{WASS,PLL}\rho_0 cos^2(\phi)\right)$.

As for using an FLL, the BER of a WAAS message with FLL tracking also follows the upper bound given in Eq.(A.1) on the preceding page except that the coefficient, D, is not as presented. A soft decision is not applicable in this case since the DPSK demodulation only resolves the sign changes between the successive data bits. Accordingly, a hard decision is applied which results in the Binary Symmetric Channel (BSC) [40, p.196]. For a BSC, the coefficient D was found by applying the maximum-likelihood metric. The result of this D is referred to as the union-Bhattacharyya error bound and expressed as [40, p.198] and [43, p.107]

$$D = \sqrt{4P_{b,FLL}(1 - P_{b,FLL})} \tag{A.3}$$

Note that T_{FLL}=0.001 sec for a WAAS signal with FLL tracking. The BER of a WAAS message with FLL tracking is evaluated by substituting Eqs. (A.3) and (2.61) into Eq.(A.1).

Therefore, the BER is

$$BER_{FLL,scint} = \int_0^\infty P_{b,FLL}(\rho_0) f_{\rho_0}(\rho_0) d\rho_0 \tag{A.4}$$

where

$f_{\rho_0}(\rho_0) = \frac{m^m \rho_0^{m-1}}{\Gamma(m)\left(\frac{C}{N_0}\right)^m} exp\left(-\frac{m\rho_0}{\frac{C}{N_0}}\right)$ and ρ_0 represents the instantaneous carrier-to-noise density ratio of the received signal;

For GPS (T_{FLL}= 0.01 sec): $P_{b,FLL}(\rho_0) = \frac{1}{2}e^{-T_{FLL}\rho_0}$; and,

For WAAS (T_{FLL}= 0.001 sec): $P_{b,FLL}(\rho_0)$ =the right hand side of Eq.(A.1) on the facing page with

$D = \sqrt{4 \cdot \frac{1}{2}e^{-T_{FLL}\rho_0}(1 - \frac{1}{2}e^{-T_{FLL}\rho_0})}$.

A.2 WER for WAAS

The WER of WAAS messages will likely to occur in bursts as a result of utilizing the Viterbi decoding of the convolutional code. Eq.(2.63) would provide a conservative result even in the case of fast scintillation. The burst property of the Viterbi decoding has been studied in [44, 45, 46, 47]. Specifically, in [44, 45], an algorithm was proposed to estimate the WER given the BER at the output of the Viterbi decoder. In the following section, we present a quick summary of the algorithm without details.

Before listing the steps of the algorithm, it is important to define an error burst. CCITT [48] defines an error burst as *"a group of bits in which two successive erroneous bits are always separated by less than a given number (L) of correct bits."* The number L is also called "Burst Length Criterion" (BLC) [44]. Here are the steps of the algorithm specified in [44].

1. Calculate the BER at the output of the Viterbi decoder, i.e., those BERs for WAAS messages in the previous paragraphs.

2. Let BLC = K-1, where K is the constraint length of the convolutional encoding. For WAAS messages, K=7.

3. Define an important measure of a code's burst error performance, called "Average Burst Length," $\overline{B}$.

$$\overline{B} = \frac{\text{Total length of all bursts}}{\text{Total number of bursts}} \tag{A.5}$$

From simulation results for BLC=6 and the asymptotic limit, $\overline{B}$ is approximated by

$$\overline{B} = 5 + \frac{17.1}{\begin{bmatrix} \sqrt{-log_{10}(2BER)} + 0.0475log_{10}(2BER) \\ +0.3161(log_{10}(2BER))^2 \end{bmatrix}} \tag{A.6}$$

4. Burst Length Distribution: Based on computer simulations with comparatively low E_b/N_0, the PDF of error burst lengths is

$$p(l) = \frac{1}{\overline{B}}\left(1 - \frac{1}{\overline{B}}\right)^{i-1} \tag{A.7}$$

5. Density of Errors in a Burst: The average density of errors in a burst of length l is

given as

$$\overline{\vartheta}(l) = \begin{cases} 1 & , \ l = 1 \\ \frac{l+2}{2l} & , \ l > 1 \end{cases} \tag{A.8}$$

6. Average Density for all Bursts: The average density of errors in all bursts can be defined as

$$\overline{\vartheta} = \frac{\text{Total number of errors}}{\text{Total length of all bursts}} \tag{A.9}$$

This is further expressed as

$$\overline{\vartheta} = \frac{\sum_{l} (l \cdot p(l) \cdot \vartheta(l))}{\sum_{l} (l \cdot p(l))} \tag{A.10}$$

7. The final WER (burst error probability) is then defined as

$$WEB = \frac{BER}{\overline{B\vartheta}} \tag{A.11}$$

Bibliography

[1] Knight, M.F., Ionospheric Scintillation Effects on Global Positioning System Receivers, Ph.D. Thesis, The University of Adelaide, Adelaide, South Australia, December, 2000.

[2] Spilker, J.J. and et al., Global Positioning System: Theory and Applications, Vol. 1, AIAA, Washington, DC, 1996.

[3] Conker, R.S., El-Arini, M.B., and et al, “Modeling the Effects of Ionospheric Scintillations on GPS/SBAS Availability,” Proc. ION AM 2000, pp. 563-576.

[4] Knight, M.F. and Finn, A., “The Effects of Ionospheric Scintillations on GPS,” Proc. ION GNSS 1998, pp. 673-685.

[5] Humphreys, T.E., Psiaki, M. L., and et al, “GPS Carrier Tracking Loop Performance in the presence of Ionospheric Scintillations,” Proc. ION NTM 2005, pp. 156-167.

[6] Pullen, S., Opshauh, G., and et al, “A Preliminary Study of the Effect of Ionospheric Scintillation on WAAS User Availability in Equatorial Regions,” Proc. ION GNSS 1998, pp. 687-699.

[7] Yu, W., Lachapelle, G., and Skone, S., “ PLL Performance for Signals in the Presence of Thermal noise, Phase noise, and Ionospheric Scintillation,” Proc. ION GNSS 2006

[8] Morrissey, T.N., Shallberg, K.W., and et al, “GPS Receiver Performance Characterization Under Simulated Ionospheric Scintillation Environments,” Proc. ION AM 2000, pp. 577-587.

[9] Morrissey, T.N., Shallberg, K.W., and et al, “GPS Receiver Performance Characterization Under Simulated Ionospheric Scintillation Environments II,” Proc. ION NTM 2002, pp. 682-693.

[10] Van Dierendonck, A.J., “Measuring Ionospheric Scintillation in the Equatorial Region Over Africa, Including Measurements From SBAS Geostationary Satellite Signals,” Proc. ION NTM 2004, pp. 316-324.

[11] So, H., Kee, C., and Kim, T., “Analysis of GPS Receiver Tracking Loss under Ionospheric Scintillation,” Seoul National University - Stanford University Student Joint Workshop, June, 2006.

[12] Hegarty, C.J., “Analytical Derivation of Maximum Tolerable In-Band Interference Levels for Aviation Applications of GNSS,” Journal of The Institute of Navigation, Vol. 44, No. 1, pp. 25-34, Spring 1997.

[13] Gebre-Egziabher, D., Razavi, A., and et al, “Sensitivity and Performance Analysis of Doppler-Aided GPS Carrier - Tracking Loops,” Journal of The Institute of Navigation, Vol. 52, No. 2, pp. 49-60, Summer 2005.

[14] Alban, S., Akos, D.M., and et al, “Performance Analysis and Architectures for INS-Aided GPS Tracking Loops,”Proc. ION NTM 2003, pp. 611-622.

[15] Alban, S., Design and Performance of a Robust GPS/INS Attitude System for Automobile Applications, Ph.D. Thesis, Stanford University, Stanford, California, U.S.A., June, 2004.

[16] Razavi, A., Sensitivity and Performance Analysis of Doppler-Aided GPS Carrier Tracking Loops, M.S. Thesis, University of Minnesota, Twin Cities, Minneapolis, Minnesota, October, 2005.

[17] Chiou, T.Y., “GPS Receiver Performance Using Inertial-Aided Carrier Tracking Loop,” Proc. ION GNSS 2005, pp. 2895-2910.

[18] Irsigler, M. and Eissfeller, B., “PLL Tracking Performance in the Presence of Oscillator Phase Noise,” GPS Solutions, Volume 5, Number 4, Spring 2002, Wiley Periodicals Inc., 2002

[19] Cahn, C.R., “Improving Frequency Acquisition of a Costas Loop,” IEEE Transactions Communications, Vol. COM-25, No. 12, pp. 1453-1459, December 1977.

[20] Natali, F.D., “AFC Tracking Algorithms,” IEEE Transactions Communications, Vol. COM-32, No. 8, pp. 935-947, August 1984.

[21] Natali, F.D., “Noise Performance of a Cross-Product AFC with Decision Feedback for DPSK Signals,” IEEE Transactions Communications, Vol. COM-34, No. 3, pp. 303-307, March 1986.

[22] Ward, P.W., “Performance Comparisons Between FLL, PLL and a Novel FLL-Assisted-PLL Carrier Tracking Loop Under RF Interference Conditions,” Proc. ION GNSS 1998, pp. 783-795.

[23] Van Dierendonck, A.J., “Technical Note on Assessment of CNAV Satellite Navigation using the C-Band,” A.J. Systems, Aug. 9, 2001.

[24] Razavi, A., Gebre-Egziabher, D., and Akos, D.M., “Tracking Weak GPS Signals: A methodology for Analysis and Experimental Validation,” IEEE Transactions on Aerospace and Electronic Systems, Vol. 43, No. 4, 2007.

[25] RTCA, Minimum Operational Performance Standards for Sensors Using GPS/WAAS, RTCA Document No. RTCA/DO-229, January 1996.

[26] Misra, P., and Enge, P., Global Positioning System: Signals, Measurements, and Performance, Second Edition, Ganga-Jamuna Press, 2006

[27] Van Dierendonck, A.J., “GPS Receivers,” in Global Positioning System: Theory and Applications, Vol. 1, AIAA, Washington, DC, 1996, pp. 330-433.

[28] Ward, P.W., “Satellite Signal Acquisition, Tracking, and Data Demodulation,” in Understanding GPS Principles and Applications, Second Edition, Artech House, Washington, DC, 2006, pp. 153-241.

[29] Rino, C.L., “A Power Law Phase Screen Model for Ionospheric Scintillation: 1. Weak Scatter,” Radio Science, Vol. 14, No. 6, pp. 1135-1145, 1979a.

[30] Fremouw, E.J., and et al, “On the Statistics of Scintillating Signals,” Journal of Atmospheric and Terrestrial Physics, Vol. 42, pp. 717-731, 1980.

[31] Conker, R.S., El-Arini, M.B., and et al, "Modeling the Effects of Ionospheric Scintillations on GPS/WAAS Availability," MITRE Working Note Number WN00W22, 2000.

[32] Spilker, J., Digital Communication by Satellite, Prentice-Hall, Cambridge, Massachusetts, pp. 336-397, 1977

[33] Gardner, F.M., Phaselock Techniques, Third Edition, John Wiley & Sons, pp. 143-182, 2005.

[34] Grebenkemper, C.J., "Local Oscillator Phase Noise and its Effect on Receiver Performance," Watkins-Johnson Company Tech-notes, vol. 8, No. 6, Nov/Dec, 1981.

[35] US Department of Defense, Global Positioning System Standard Positioning Service Signal Specification, Appendix A, Second Edition, June, 1995.

[36] Hamkins, J., "A Joint Receiver-Decoder for Convolutionally Coded BPSK," The Telecommunications and Mission Operations Progress Report, Vol. 42-139, November 15, 1999.

[37] RTCA, Environmental Conditions and Test Procedures for Airborne Equipment, Section 8, Vibration, RTCA Document No. RTCA/DO-160D, December 14, 2000.

[38] Viterbi, A.J., Principles of Coherent Communication, McGraw-Hill Inc., 1966

[39] Holmes, J.K., Coherent Spread Spectrum Systems, John Wiley & Sons, Inc., 1982.

[40] Simon, M.K., Omura, J.K., and et al, Spread Spectrum Communications, Volume I, Computer Science Press, 1985.

[41] Ho., K.P., "The Effect of Interference Phase Error on Direct-Detection DPSK and DQPSK Signals," IEEE Photonics Technology Letters, Vol. 16, No. 1, January, 2004

[42] Proakis, J.G., Digital Communications, 4th Edition, McGraw Hill, 2000.

[43] Viterbi, A.J. and Omura, J.K., Principles of Digital Communication and Coding, McGraw-Hill Inc., 1979

[44] Franchi, A. and Harris, R.A., "On the Error Burst Properties of Viterbi Decoding," Proc. IEEE International Conference on Communications, pp. 1086-1091, Geneva, Switzerland, 23-26 May 1993.

[45] Franchi, A. and Harris, R.A., "On the Error Burst Properties of the "Standard" K=7, Rate-1/2 Convolutional Code with Soft-Decision Viterbi Decoding," Telecommunication Systems, Vol. 6, No. 3, pp. 337-351, May-June 1995.

[46] Porat, Y. and Reichman, A., "Burst Error Characteristics of Viterbi Decoding of Convolutional Codes," Proc. 17th Convention of Electrical and Electronics Engineers in Israel, pp. 230-233, Tel Aviv, Israel, 5-7 March 1991.

[47] Morris, J.M., "Burst Error Statistics of Simulated Viterbi Decoded BPSK on Fading and Scintillating Channels," IEEE Transactions on Communications, Vol. 40, No. 1, p.34-41, January 1992

[48] CCITT "Blue Book," Vol. 1, Fascicle I.3, "Terms and Definitions," Rec.M.60, n.34, Rec.Q.9 n.0222.

[49] Nakazawa, M. and Suzuki, K., "Cesium Optical Atomic Clock: an optical pulse that tells the time," Optics Letters, Vol. 26, No. 9, 1 May, 2001.

[50] Vig, J.R., "QUARTZ CRYSTAL RESONATORS AND OSCILLATORS, For Frequency Control and Timing Applications A Tutorial," U.S. Army Communications-Electronics Command, Attn: AMSEL-RD-C2-PT, Fort Monmouth, NJ 07703, USA, June 2003.

[51] Johnson, G., Lage, M. and et al, "The JPALS performance Model," Proceeding of the ION-GPS 2003, Portland, OR, September 2003.

[52] Peterson, B. R., Johnson, G. and et al, "Feasible Architectures for Joint Precision Approach and Landing System (JPALS) for Land and Sea," Proceeding of the ION-GPS 2004, Long Beach, CA, September 2004.

[53] Bastide, F., Akos, D. and et al, "Automatic Gain Control Control (AGC) as an Interference Assessment Tool," Proceeding of the ION-GPS 2003, Portland, OR, September 2003.

[54] Philips, R., and Schmidt, G. T., GPS/INS Integration, AGARD Lecture Series on System Implications and Innovative Application of Satellite Navigation, Paris, France, July 1996.

[55] Gebre-Egziabher, D., Razavi, A., and et al, "Inertial-aided Tracking Loops for SRPS Integrity Monitoring," Proceeding of the ION-GPS 2003, Portland, OR, September 2003.

[56] Misra, P. and Enge, P., Global Positioning System: Signals, Measurements and Performance, Ganga-Jamuna Press, Lincoln, Massachusetts, USA, 2001. pp. 356.

[57] Best, R. E., Phase-Locked Loops:Design, Simulations, and Applications, McGRAW-Hill, Third Edition, 1997. pp1-89.

[58] Gebre-Egziabher, D., and Razavi, A., personal communication entitled "Evaluation of GPS PLL and FLL Architectures in RFI Environments," 2005.

[59] Travis, C., "Automatic Frequency Control," Proc. The Institute of Radio Engineers, Vol. 23, No. 10, Oct., 1935.

[60] Natali, F.D., "AFC Tracking Algorithms," IEEE Transactions Communications, Vol. COM-32, No. 8, pp. 935-947, August 1984.

[61] Chiou, T.Y., Gebre-Egziabher, D. and et al, "Model Analysis on the Performance for an Inertial Aided FLL-Assisted-PLL Carrier-Tracking Loop in the Presence of Ionospheric Scintillation," Proc. ION NTM 2007.

[62] Haykin, S., Communication Systems, 4th Edition, John Wiley & Sons, Inc., 2001.

[63] Gerald, C.F., and Wheatley, P.O., Applied Numerical Analysis, 5th edition, Addison-Wesley, pp. 628-650, 1994.

[64] Tikhonov, V.I., "The Operation of Phase and Automatic Frequency Control in the Presence of Noise,"Automation and Remote Control, Vol. 21, No.3, AIAA, pp. 209-214, 1960.

[65] Holmes, J.K., Spread Spectrum Systems for GNSS and Wireless Communications, Artech House, 2007.

[66] Brown, R.G. and Hwang, P.Y.C., Introduction to Random Signals and Applied Kalman Filtering with Matlab Exercises and Solutions, 3rd Edition, Wiley, 1996.

[67] Gebre-Egziabher, D., Design and Performance Analysis of a Low-Cost Aided Dead Reckoning Navigator, Ph.D. Thesis, Stanford University, Stanford, California, U.S.A., December, 2001.

[68] Secan, J.A., Bussey, R.M., Fremouw, E.J., Basu, S., "An Improved Model of Equatorial Scintillation," Radio Science, vol. 30, No. 3, pp. 607-617, 1995.

[69] Hegarty, C.J., et al, "Scintillation Modeling for GPS/WAAS Receivers," Radio Science, vol. 36, No. 5, pp. 1221-1231, 2001.

[70] Beach, T.L., Kintner, P.M., "Simultaneous Global Positioning System Observations of Equatorial Scintillations and Total electron Content Fluctuations," Journal of Geophysical Research, vol. 104, No. A10, pp. 22,553-22,565, October, 1999.

[71] Basu, S., et.al., "250 MHz/GHz Scintillation Parameters in the Equatorial, Polar, and Auroral Environments," IEEE J. Selected Areas in Communications, vol. SAC-5, No. 2, pp. 102-115, February, 1987.

[72] Van Dierendonck, A.J., Reddan, P., and Nicholson M., "GPS Receiver Performance Characterization under Simulated Ionospheric Scintillation Environments," Proceeding of the ION-NTM 1999, San Diego, CA, January, 1999.

[73] Van Dierendonck, A.J., Klobuchar, J., and Hua, Q., "Ionospheric Scintillation Monitoring Using Commercial Single Frequency C/A Code Receivers," Proceeding of the ION-GPS 1993, Salt Lake City, UT, September, 1993.

[74] Borre, K., Akos, D., and et al, A Software-Defined GPS and Galileo Receiver: A Single-Frequency Approach, Birkhauser, 2006.

[75] Goodman, J.M. and Aarons, J., "Ionospheric Effects on Modern Electronic Systems," Proceedings of the IEEE, Vol. 78, No. 3, pp. 512-528, March 1990.

[76] Beniguel, Y., Adam, J.P., and et al, "Analysis of Scintillations Recorded in The Equatorial Regions," Beacon Satellite Symposium, Boston, 2007.